Interferometric Unruh Detectors

Steffen Biermann

School of Mathematical Sciences

Thesis submitted for the degree of Doctor of Philosophy
at the University of Nottingham

November, 2022

Interferometric Unruh Detectors

Steffen Biermann

University of Nottingham
UK | CHINA | MALAYSIA

School of Mathematical Sciences

Thesis submitted for the degree of Doctor of Philosophy
at the University of Nottingham

External Examiner: Prof. Christopher Fewster
Internal Examiner: Dr. Tommaso Tufarelli

November, 2022

Abstract

The Unruh effect strikes with its simple yet surprising statement that a uniformly linearly accelerated observer experiences the Minkowski vacuum as a thermal state with a temperature that is proportional to the observer's acceleration. This raises fundamental questions about the concepts of particles and vacua and to date, due to the smallness of the effect, there has been no experimental evidence thereof. Analogue gravity systems approach this issue by providing an effective relativistic vacuum state. They refer to a broad range of experimentally accessible systems in which the dynamical equations for small excitations are mathematically equivalent to the dynamics of relativistic quantum fields.

In this thesis, we introduce the mathematical framework for localised detectors in accelerated motion to probe the effective relativistic vacuum of an analogue gravity system. First, we show that Unruh detectors can be implemented by broad-band or continuous field detectors and derive the Unruh temperature for a circular trajectory in $3+1$ and $2+1$ dimensions. Then, we argue that localised laser beams can be used as continuous field Unruh detectors and support our argument with the modelling of two low-temperature analogue systems, namely Bose-Einstein condensates and superfluid Helium-4 thin films, interacting with a localised laser beam on a circular trajectory.

An analysis of experimentally feasible parameters for these analogue systems indicates that the Unruh effect is within the realm of current experimental possibilities. Finally, we complement these findings with signal extraction methods developed in the context of quantum optics and a first experimental realisation of localised measurement probes relevant for the proposed analogue Unruh detectors.

Acknowledgements

First and foremost, I would like to thank my supervisors Silke Weinfurtner and Jorma Louko for providing me with the opportunity to write this thesis under their supervision, for their constant support and guidance during this time and for introducing me to the fascinating world of Unruh detectors and analogue gravity.

During my PhD, I was fortunate to collaborate with incredibly great minds, whose ideas have been tremendously inspiring – thank you for all our projects together.

I would also like to thank everyone in the extended Gravity Laboratory group for making this thesis possible and for all the help along the way.

Contents

I

Introduction

The same equations have the same solutions.
—The Feynman Lectures on Physics

Probably no other theories in the history of physics have been tested as thoroughly as general relativity and quantum mechanics. Experiments in both theories continue to provide fascinating results, in their very own regime of relevant energy and length scales, one of which was recently honoured with the Nobel Prize in Physics "for experiments with entangled photons, establishing the violation of Bell inequalities and pioneering quantum information science". Naturally, the question arises whether it is possible to combine the two theories – a quantum theory of gravity [1, 2]. There have been theoretical advances trying to overcome this apparent conceptual incompleteness of our present understanding, but it turns out that the combination of gravity, a macroscopic theory, and quantum mechanics, a microscopic theory, is rather difficult. It seems that we need to understand the interplay of both theories much better – both theoretically, and with support from experiments! Instead of the desired, but not yet achievable, goal of a quantised theory of gravity, one can work with quantum field theory in curved spacetime (QFTCS), in which we consider quantum fields propagating in a classical, curved spacetime [3, 4]. QFTCS is expected to account for gravitational contributions in quantum phenomena unless curvatures reach Planckian scales.

Experimental confirmation is essential for a physical theory, even if sometimes it is a long time in the making. The discovery of the Higgs boson is one such example that was detected experimentally only 60 years after its theoretical prediction [5, 6]. Other milestones include the detection of gravitational waves in 2016 [7] and the first ever picture taken of the black hole in the centre of galaxy M87 in 2019 [8]. This image was celebrated as a huge success in black hole research after the prediction of black holes in Einstein's theory of general relativity in 1915 [9, 10]. Black holes are interesting objects on many levels – one of the reasons is the

interplay between gravity and quantum mechanics in and around black holes leading to peculiar effects. Hawking radiation is such a phenomenon on the boundary between gravity and quantum mechanics which states that an observer far away from a black hole would see thermal radiation coming from the black hole, even though the quantum field was in a state that evolved from a no-particle state before the black hole formation [11].

Hawking's theoretical discovery of radiating black holes was driven by the endeavour at that time to define the concept of particles, pioneered by Parker's work on cosmological particle creation [12, 13, 14, 15]. Parker's considerations led Fulling to define particles in flat spacetime in terms of accelerated Rindler coordinates instead of the usual Minkowski coordinates [16]. At the same time, Unruh thought about particles as excitations of an accelerated particle detector – typically modelled as a two-level system that is locally coupled to a field. Their calculations showed another rather peculiar effect – an accelerated observer perceives the Minkowski vacuum as a thermally occupied state [17, 18, 19, 20]. The temperature T of this state is found to be proportional to the acceleration a of the observer

$$k_{\mathrm{B}}T \;=\; \frac{\hbar a}{2\pi c}\,.$$

Despite its elegant derivation and simplicity compared to the Hawking effect, which needs a black hole to occur, the Unruh effect exhibits a serious complication. An Unruh temperature of 1 Kelvin requires an acceleration of about 10^{20} m/s^2. One of the reasons why there is still a lack of experimental evidence.

The original descriptions of this acceleration radiation use a linearly accelerated trajectory, however, Bell and Leinaas showed that similar effects can be achieved using a circular trajectory [21, 22]. Their results demonstrate that the spectrum of a circularly accelerated detector is approximately thermal with a temperature that is dependent on the energy gap between the ground and excited state of the detector, which is a striking difference to the case of a linear acceleration. The circular acceleration spectrum, however, is sufficiently similar to the linear acceleration. So if one could experiment with such a circularly accelerated detector, it would give a strong hint to whether there exists such a thermal state with this characteristic temperature.

QFTCS leads to interesting physical phenomena, however, at the same time these phenomena, such as the Unruh effect, are incredibly difficult to probe experimentally. But what if we could find a system that exhibits the same characteristics, theoretically and experimentally – an analogue so to speak? Such an analogue could help test these challenging phenomena in well-controlled, earthbound, laboratories. Analogies in general have always played a significant role in physics and mathematics. They allow us to take a question from a target system and transfer it to a source system. As the name of a chapter in Feynman's lectures on physics "The same equations have the same solutions" suggests, the answer to this question in the source system is like a map that could be a representation of multiple territories [23]. This has the tremendous advantage of not being constrained by restrictions from the target system, but allows to use the full knowledge of the source system. These transfers have been made frequently in the past, even if it was only to visualise certain aspects in Gedankenexperiments, as they were frequently used by Einstein to think about concepts of relativity.

In the 1980s, William Unruh drew a connection between gravitation and fluids during a lecture in fluid mechanics – an idea very much motivated by the characteristics of black holes.

A black hole is a region in spacetime where the gravitation pull is so strong that neither matter nor light can escape. This phenomenon also appears in fluids, such as a river ending in a waterfall. In Unruh's analogy, fish in the river communicate via sound waves and as long as they stay far from the waterfall, they can move and communicate freely. However, once a fish starts to get dragged over the edge by the downstream flow, there exists a point at which the speed of the falling water exceeds the speed of sound waves travelling in water. Just as the event horizon of a gravitational black hole, this waterfall has a sonic horizon past which neither fish nor sound can escape – an idea that led to the birth of analogue gravity [24, 25]. This analogy seems like a simple visualisation of black hole processes, but Unruh showed that this is indeed a mathematically consistent analogue. Sound waves propagating in ideal fluids obey the same equations as massless scalar fields that live on an effective curved spacetime, laying the cornerstone for many acoustic analogues and everything that followed [26, 27, 28, 29].

In the beginning, analogue gravity was purely a theoretical field of research, however, in the last decade experimental groups all over the world have started researching analogue systems [30, 31]. Analogues are by far not restricted solely to fluids [32] but have been found as well for electromagnetic waves in dielectric media [33, 34] and interfaces waves [35]. With technological advances, cold atom analogues, such as Bose-Einstein condensates (BECs) [36, 37, 38, 39] and superfluid Helium [40, 41], have become increasingly popular, however, an important milestone was the measurement of stimulated Hawking emission in a classical fluid analogue [42]. The experimental triumph of analogues in classical fluids continued, with measurements of the first superradiant scattering in a bathtub vortex [43], black hole ringdown [44] and back action with background fluid flows [45].

But can we use analogue systems to learn more about what Feynman listed as "Accel. Temp." in the "to learn" section on his blackboard? If so, it could help improve our understanding of quantum fields and particles not only on a theoretical level. Compared to other effects, there are only a limited amount of proposals to detect the Unruh effect in analogue systems [46, 47]. Motivated by pioneering work on BEC analogues [48, 49, 50, 51, 52, 53] and the circular acceleration description of the Unruh effect, this thesis positions itself in the sparsely populated space of experimental analogue Unruh effect proposals by presenting a novel approach for a detection scheme in cold-atom systems to shed light on the vacuum in quantum field theories.

The second chapter II is an introduction to the Unruh effect in its original description arising from a linearly accelerated observer, followed by its extension to circular accelerations. We calculate the response function of a detector in a $(3+1)$ and $(2+1)$-dimensional, relativistic quantum field theory and translate those findings to analogue systems. The results have been published in [54]. Furthermore, we introduce a continuous field detector model and show its equivalence to the standard Unruh-DeWitt detector. The analogue models that are introduced in the following chapters are a mapping to this detector model.

In chapter III, we create two explicit systems and show that they provide a suitable setup to detect the analogue Unruh effect. We show that a laser beam can act as a continuous detector, as opposed to the traditional two-level Unruh-DeWitt detector, and derive a regime in which its interaction with matter results in the coupling, as required for a mapping to the detector model. We introduce two analogue systems, a Bose-Einstein condensate and superfluid Helium-4. The mathematical description of those system is found to be an analogue of the relativistic detector model. We provide a conceptual schematic setup, as well as experimental feasibility estimates. Using a laser beam as a continuous detector to probe quantum systems in order to look for the

Unruh effect is a novel approach and has been published in [55], while the superfluid Helium-4 results are yet to be published [56].

Chapter IV is about the operator description of the two analogue systems. We use Glauber's theory of photodetection and the photon counting formula to find the signal at the photodiodes and how it connects to the information present in the system. While the preceding chapter was more about conceptual feasibility statements, this chapter is about the details of how to extract the signal related to the Unruh effect. It establishes the bridge from classical detection to quantum processes. This chapter contains unpublished work.

Chapter V paves the way towards an experimental implementation of the Unruh effect detection concept in superfluid Helium-4. We present an experiment as proposed in [57, 58] that utilises confocal microscopy to measure thermal surfaces waves on classical fluids. We give a brief introduction to the underlying theory and provide an outlook on how this method can be used for superfluids and measurements of the Unruh effect.

We conclude with an outlook on future research in chapter VI, how the findings of this thesis can be used in ongoing projects and what the limitations of those approaches are. Analogue gravity experiments can not entirely replace experiments on real gravitational systems, however, analogue gravity models help understand detector schemes, which can be used as a stepping stone towards the measurement of the real Unruh effect. Whilst doing so, analogue detectors push the boundaries of current technologies and help progress towards a clearer picture of the quantum vacuum state.

Notations and Conventions. Throughout this thesis, we will use the following notations and conventions unless explicitly mentioned otherwise.

Coordinates. d-dimensional spacetime coordinates are usually written as $x = (t, \boldsymbol{x})$ while the $d-1$ space coordinates are written in boldface $\boldsymbol{x}$. Functions that depend on spacetime coordinates are either written as $\phi(x)$ or as $\phi(t, \boldsymbol{x})$, whenever a clarifying distinction between t and $\boldsymbol{x}$ seems appropriate.

Einstein Sum Convention. We will use the convention that whenever two indices appear at the same time as sub- and superscript, an implicit summation over these indices is assumed

$$a_i a^i \;=\; \sum_i a_i a^i \,. \tag{1.1}$$

Derivatives. Most of the time we will use the following short notation for derivatives

$$\partial_i \;=\; \frac{\partial}{\partial x_i} \,. \tag{1.2}$$

Minkowski Metric. We define the Minkowski metric with the following sign convention

$$g_{\mu\nu} \;=\; \begin{pmatrix} -1 & & & \\ & 1 & & \\ & & \ddots & \\ & & & 1 \end{pmatrix} , \tag{1.3}$$

We use the short notation for the derivative

$$\partial_\mu \;=\; \frac{\partial}{\partial x^\mu} \;=\; \left(\frac{1}{c}\frac{\partial}{\partial t}, \boldsymbol{\nabla}\right) , \tag{1.4}$$

and in contravariant form

$$\partial^\mu \;=\; g^{\mu\nu}\partial_\nu \;=\; \left(-\frac{1}{c}\frac{\partial}{\partial t}, \boldsymbol{\nabla}\right) . \tag{1.5}$$

Fourier Transform. We adopt the following notation throughout this thesis

$$f_\omega \;=\; \int \mathrm{d}t\; \mathrm{e}^{\mathrm{i}\omega t} f(t) , \tag{1.6}$$

such that all Fourier components are labelled with a subscript.

Densities. Throughout the text, mass densities will generally be denoted by ρ whereas number densities will be denoted either by n or by ρ_N whenever we need to avoid confusion with refractive indices.

II

Unruh Effect and Detectors

A particle is what a particle detector detects.
—William Unruh

Fulling in 1973 [16], Davies in 1975 [20] and Unruh in 1976 [17] described the phenomenon arising in relativistic quantum field theory that an uniformly accelerated observer sees the Minkowski vacuum as a thermal state with a characteristic temperature proportional to its acceleration a. Most famously, the temperature of this state, which is now known as the Unruh temperature, is given by

$$k_{\mathrm{B}}T \;=\; \frac{\hbar a}{2\pi c}\,. \tag{2.1}$$

This counter-intuitive phenomenon has led Unruh to think further about this acceleration radiation and particle detectors. The most prominent example of such a detector to detect quantum particles is known as the Unruh-DeWitt detector, a simple two-level system [18]. This chapter follows this historical development by first introducing the Unruh effect of a linearly accelerated observer, before discussing Unruh-DeWitt detectors. We will then show that this effect is not limited to linear acceleration only and calculate how a particle detector reacts to a circular acceleration in $3+1$ and $2+1$ dimensions and extend the traditional understanding of two-level Unruh-DeWitt detectors to continuous detectors [18].

We conclude this chapter with an outlook to the actual implementation in analogue systems.

2.1 Linear Unruh Effect

As the starting point of this discussion, we want to introduce the general setting in which the Unruh effect occurs. The key idea of it is the concept of acceleration. To simplify the notation, we assume that the acceleration takes place in just one direction of our coordinate system, say in x-direction. Now, imagine two frames in $(1+1)$-dimensional Minkowski space, one inertial frame with coordinates (t, x) and one accelerated frame with coordinates (τ, ξ), which is uniformly accelerated with acceleration a. The time of a inertial frame t is related to the to the time of the accelerated frame τ via the gamma factor

$$\gamma \;=\; \frac{1}{\sqrt{1-\frac{v^2}{c^2}}}\,. \tag{2.2}$$

such that $\mathrm{d}t = \gamma(v)\mathrm{d}\tau$. The coordinates of the inertial frame and the coordinates of the accelerated frame are related via the coordinate transformation [59]

$$t \;=\; a^{-1}\mathrm{e}^{a\xi}\sinh a\tau \tag{2.3a}$$
$$x \;=\; a^{-1}\mathrm{e}^{a\xi}\cosh a\tau\,, \tag{2.3b}$$

yielding the relation $x^2 - t^2 = a^{-2}\mathrm{e}^{2a\xi}$. For constant ξ, this expression describes a hyperbolic trajectory, as shown in figure 2.1.

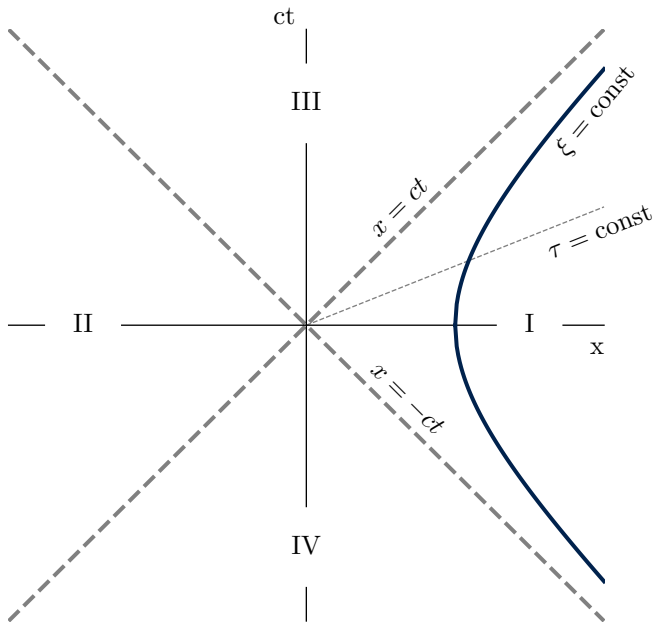

Figure 2.1 (Accelerated Motion) Hyperbolic motion of uniform acceleration in spacetime diagram. The world line with $ct = x$ forms a horizon for the accelerated motion. The hyperbolae represent curves with $\xi = \text{const}$ and the straight lines $\tau = \text{const}$. Without loss of generality we focus on the right Rindler wedge I with $x > |ct|$.

This figure shows, furthermore, that lightlike world lines passing through the origin are asymptotic to the accelerated motion. Those asymptotics divide the spacetime diagram into four

distinct regions, which are labelled from I to IV. The line element is given by $\mathrm{d}s^2 = -\mathrm{d}t^2 + \sum_i \mathrm{d}x_i^2$ in Minkowski coordinates, and in Rindler coordinates it becomes $\mathrm{d}s^2 = -\mathrm{e}^{2a\xi}\left(\mathrm{d}\tau^2 - \mathrm{d}\xi^2\right) + \sum_{i'} \mathrm{d}x_{i'}^2$. We want to consider a massive, free scalar field in a d dimensional spacetime with arbitrary geometry with metric $g^{\mu\nu}$ and derive how this field behaves under uniform acceleration. The Lagrangian density of this minimally coupled field ϕ with mass m is

$$\mathcal{L} \;=\; \frac{1}{2}(-g)^{-1/2}\left\{g^{\mu\nu}\partial_\mu\phi^*\partial_\nu\phi + m^2\phi^*\phi\right\}\;, \tag{2.4}$$

with spacetime indices $\mu = 0, \ldots, d$. The zero component of these indices will be associated with a time component t and the remaining $d-1$ indices with space components x^i, in the following labelled with Latin indices. Applying the variation principle to the associated action

$$S \;=\; \int \mathrm{d}^d x\, \mathcal{L}\;, \tag{2.5}$$

leads to the equation of motion for ϕ

$$\left(-(-g)^{-1/2}\partial_\mu g^{\mu\nu}(-g)^{1/2}\partial_\nu - m^2\right)\phi \;=\; 0\;. \tag{2.6}$$

In the special case of a Minkowskian spacetime with metric

$$g^{\mu\nu} \;=\; \begin{pmatrix} -1 & & & \\ & 1 & & \\ & & \ddots & \\ & & & 1 \end{pmatrix}\;, \tag{2.7}$$

we find $\sqrt{-g} = 1$ and the Lagrangian simplifies to

$$\mathcal{L} \;=\; \frac{1}{2}\left(\partial_\mu\phi^*\partial^\mu\phi + m^2\phi^*\phi\right)\;. \tag{2.8}$$

The equation describing the dynamics of this field is the Klein-Gordon equation, given by

$$\left(\partial^2 + m^2\right)\phi(t,\boldsymbol{x}) \;=\; 0\;, \tag{2.9}$$

where we used the short notation $\partial^2 = \partial_\mu\partial^\mu = -\partial_0^2 + \sum_i \partial_i^2$. Upon quantisation, the scalar field becomes an operator and as such, its dynamics are described by the equation above. It has the mode expansion

$$\hat{\phi}(t,\boldsymbol{x}) \;=\; \int \mathrm{d}^d k\left(\hat{a}_k U_k(t,\boldsymbol{x}) + \hat{a}_k^\dagger U_k^*(t,\boldsymbol{x})\right)\;, \tag{2.10}$$

with positive-frequency modes U_k and negative-frequency modes U_k^*, which are given by

$$U_k(t,\boldsymbol{x}) \;=\; \left[2\omega_k(2\pi)^{d-1}\right]^{-1/2}\exp\left\{-\mathrm{i}\left(k^0 t - \boldsymbol{k}\cdot\boldsymbol{x}\right)\right\}\;, \tag{2.11}$$

with $(k^0)^2 = \omega_k^2 = \boldsymbol{k}^2 + m^2$.

The operators $\hat{a}_k$ and $\hat{a}_k^\dagger$ are annihilation and creation operators for modes U_k and obey the commutation relations

$$\left[\hat{a}_k, \hat{a}_{k'}^\dagger\right] = \delta(k-k') \,, \tag{2.12a}$$

$$\left[\hat{a}_k^\dagger, \hat{a}_{k'}^\dagger\right] = \left[\hat{a}_k, \hat{a}_{k'}\right] = 0 \,. \tag{2.12b}$$

These operators act on the states of this field, one of which is the vacuum state. The Minkowski vacuum $|0_\mathrm{M}\rangle$ is defined as the state that is annihilated by $\hat{a}_k$, such that $\hat{a}_k |0_\mathrm{M}\rangle = 0$[1] and the Fock space of states is created by repeatedly applying $\hat{a}_k^\dagger$ to this vacuum state [60]. The annihilation and creation operators can be extracted from the mode expansion using the Klein-Gordon inner product

$$\hat{a}_k = \left(U_k, \hat{\phi}\right)_\mathrm{KG} := \mathrm{i}\int \mathrm{d}\boldsymbol{x} \left(U_k(t,\boldsymbol{x})^* \partial_t \hat{\phi}(t,\boldsymbol{x}) - \partial_t U_k(t,\boldsymbol{x})^* \hat{\phi}(t,\boldsymbol{x})\right) . \tag{2.13}$$

Furthermore, we can use this inner product to normalise the modes

$$(U_k, U_{k'})_\mathrm{KG} = \delta(k-k') \,, \tag{2.14a}$$

$$(U_k, U_{k'}^*)_\mathrm{KG} = 0 \,, \tag{2.14b}$$

$$(U_k^*, U_{k'}^*)_\mathrm{KG} = -\delta(k-k') \,. \tag{2.14c}$$

Similarly, we can describe the equation of motion for $\hat{\phi}$ in terms of Rindler coordinates τ and ξ of Rindler wedge I (2.3) with $x > |ct|$

$$\left(\partial_\tau^2 - \partial_\xi^2\right) \hat{\phi}_I(\tau, \boldsymbol{\xi}) = 0 \,, \tag{2.15}$$

where $\boldsymbol{\xi}$ is a shorter notation for the transformed coordinate ξ and the remaining coordinates $x_{i'}$. This has the same form as in Minkowski coordinates and, therefore, has the solutions

$$\hat{\phi}_I(\tau, \boldsymbol{\xi}) = \sum_k \left(\hat{b}_k \widetilde{U}_k(\tau, \boldsymbol{\xi}) + \hat{b}_k^\dagger \widetilde{U}_k{}^*(\tau, \boldsymbol{\xi})\right) , \tag{2.16}$$

with the modes $\widetilde{U}_k(\tau, \boldsymbol{\xi})$ being identical in form to the Minkowski modes $U_k(\tau, \boldsymbol{\xi})$. The important difference here is that the operators $\hat{b}_k$ are not the same as the operators $\hat{a}_k$. For this set of new operators $\hat{b}_k$ we can define the Rindler vacuum as the state that satisfies $\hat{b}_k |0_\mathrm{R}\rangle = 0$. As both Minkowski and Rindler modes form a complete set of orthonormal modes they are related via a Bogoliubov transformation

$$\widetilde{U}_k = \sum_l \left(u_{lk} U_l + v_{lk} U_l^*\right) . \tag{2.17}$$

Equating both the Minkowski and Rindler expansion for ϕ and using (2.17) shows that the creation and annihilation operators in both expansions are related via the transformation

$$\hat{b}_k = \sum_l \left(u_{kl}^* \hat{a}_l - v_{kl}^* \hat{a}_l^\dagger\right) . \tag{2.18}$$

The coefficients can be extracted using the inner product (2.13) between the Rindler mode (2.17)

[1] If not specified otherwise, the vacuum state $|0\rangle$ refers to the Minkowski vacuum.

and the Minkowski mode, and solving the integrals [61]. The particle number operators $\hat{a}_k^\dagger \hat{a}_k$ and $\hat{b}_k^\dagger \hat{b}_k$ determine the number of particles of a given state, with $\langle 0_M | \, \hat{a}_k^\dagger \hat{a}_k \, | 0_M \rangle = \langle 0_R | \, \hat{b}_k^\dagger \hat{b}_k \, | 0_R \rangle = 0$.

At this point, we have constructed the operator description of scalar fields, both in Minkowski and Rindler coordinates, and have presented a transformation that relates the annihilation and creation operators in each coordinate system. In addition, we have provided a definition of the vacuum state. The previous considerations suggest that the vacuum state is not unique [16, 62]. It depends on the observer, one can use the Bogoliubov transformation to calculate the expectation value (for details see [61])

$$\langle 0_M | \hat{b}_k^\dagger \hat{b}_k | 0_M \rangle \;\; = \;\; \frac{1}{\mathrm{e}^{\frac{\hbar a}{2\pi c}} - 1} \, . \tag{2.19}$$

This is a well known distribution, most commonly referred to as the Bose-Einstein statistics and is the particle distribution of a thermal state with a finite temperature. Interestingly, this shows that an accelerated observer sees the Minkowski vacuum as a thermally occupied state with temperature $k_\mathrm{B} T_\mathrm{U} = \frac{\hbar a}{2\pi c}$, which linearly depends on the acceleration. This is the Unruh temperature.

2.2 Unruh-DeWitt Detectors

After having derived the linear acceleration Unruh effect, we want to extract information about the Rindler vacuum, or the thermal state that an accelerated observer sees. For this purpose, we use the conceptually simplest detector model proposed by DeWitt [63] consisting of a point-like object with two distinct energy levels. This detector couples with its monopole moment operator $\hat{m}$ to a scalar field $\hat{\phi}$. Extensions to higher moments, such as dipoles, are described in [61]. We provide more detail in this chapter and follow the standard derivation of Birrell and Davies [4], as this will become important later when we talk about continuous detectors. The interaction is described by the Lagrangian with coupling $c(\tau)$

$$\mathcal{L}_{\text{int}} \;=\; c(\tau)\hat{m}(\tau)\hat{\phi}\left(x^{\mu}(\tau)\right) \;, \tag{2.20}$$

with τ being the proper time of the detector moving along the world line $x^{\mu}(\tau)$. Note, that the coupling may be time dependent and may be interpreted as a (time) constant times a switching function $c\chi(\tau)$. The switching function turns the interaction between the detector and the field on and off. At this point, however, we will not go into the technical details of this switching function (for details, cf. [64]) and will assume a constant interaction for all times $c(\tau) \equiv c$ for which the trajectory is defined. Throughout this section, we will work in natural units $\hbar = c_0 = 1$. The two level system has a ground state with energy E_0 and an excited state with energy $E > E_0$, both separated by the energy gap $\Delta E = E - E_0 > 0$. This level system can be understood as an atom that has a ground and excited state.

Assume that the scalar field is initially in the Minkowski vacuum state $|0_M\rangle$ and the detector is in a state with energy E_0. Prior to the interaction the whole system is in the state $|0_M E_0\rangle$. The question is whether this interaction will cause a transition into another state $|\psi E\rangle$. The first step towards answering this question is to calculate the transition amplitude (simplifying x^{μ} to x) in first order perturbation theory

$$\mathcal{M} \;=\; \mathrm{i}c\,\langle E\psi| \int_{-\infty}^{\infty} \mathrm{d}\tau\; \hat{m}(\tau)\hat{\phi}\left(x(\tau)\right)|0_M E_0\rangle \;. \tag{2.21}$$

Working in the interaction picture in which the time dependence of operators is defined by the free Hamiltonian $\hat{H}_d$ of the detector, the monopole moment operator can be written as

$$\hat{m}(\tau) \;=\; \mathrm{e}^{\mathrm{i}\hat{H}_d\tau}\hat{m}(0)\mathrm{e}^{-\mathrm{i}\hat{H}_d\tau} \;, \tag{2.22}$$

with $\hat{H}_0\,|E\rangle = E\,|E\rangle$. Using this expression, the transition amplitude can be written as

$$\mathcal{M} \;=\; \mathrm{i}c\,\langle E|\hat{m}(0)|E_0\rangle \int_{-\infty}^{\infty} \mathrm{d}\tau\; \mathrm{e}^{\mathrm{i}(E-E_0)\tau}\,\langle\psi|\hat{\phi}\left(x(\tau)\right)|0_M\rangle \;. \tag{2.23}$$

Using the mode expansion in equation (2.10) for $3+1$ dimensions, we see that the only states in our basis contributing to the transition amplitude are the one-particle states $|1_{\boldsymbol{k}}\rangle$ with momenta $\boldsymbol{k}$

$$\langle 1_{\boldsymbol{k}}|\hat{\phi}(x(\tau))|0_M\rangle \;=\; (2\pi)^{-\frac{3}{2}}\,\frac{\mathrm{e}^{-\mathrm{i}k\cdot x(\tau)}}{\sqrt{2\omega_k}} \;, \tag{2.24}$$

where we have used that $\langle 1_{\boldsymbol{k}}|\,a^{\dagger}(k')\,|0_M\rangle = \delta^3(\boldsymbol{k}-\boldsymbol{k}')$ and $\omega_k^2 = |\boldsymbol{k}|^2 + m^2 > 0$.

If the detector is moving along an inertial trajectory parametrised by $\boldsymbol{x}(\tau) = \boldsymbol{x}_0 + \gamma\boldsymbol{v}\tau$ with

$\gamma = (1-v^2)^{-1/2}$, $v<1$, then the integral in the transition amplitude reads

$$\mathcal{M} \;=\; \mathrm{i}c\,\langle E|\hat{m}(0)|E_0\rangle\,(2\pi)^{-3/2}\,\frac{1}{\sqrt{2\omega}}\mathrm{e}^{\mathrm{i}\boldsymbol{k}\cdot\boldsymbol{x}_0}\int_{-\infty}^{\infty}\mathrm{d}\tau\;\mathrm{e}^{\mathrm{i}(E-E_0+\gamma(\omega-\boldsymbol{k}\cdot\boldsymbol{v}))\tau}\;. \tag{2.25}$$

The integral is a representation of the delta distribution $2\pi\delta(E-E_0+\gamma(\omega-\boldsymbol{k}\cdot\boldsymbol{v}))$, which means that a transition can only occur when the argument of this delta distribution equals zero. However, on the one hand we know that $E>E_0$ and on the other hand we have $\omega\geq|\boldsymbol{k}|>|\boldsymbol{k}||\boldsymbol{v}|\geq\boldsymbol{k}\cdot\boldsymbol{v}$ and $\gamma>0$ such that the sum in the delta distribution is strictly greater than zero causing the transition amplitude to vanish for inertial trajectories. In summary, there would be no transition from the ground state to excited states if the detector were moved on an inertial trajectory.

However, keeping the expression more general for some arbitrary trajectory $x(\tau)$ we can calculate the transition probability for excitations from the ground state to any allowed state

$$|\mathcal{M}|^2 \;=\; c^2\sum_{E,\psi}|\,\langle E|\hat{m}(0)|E_0\rangle\,|^2\int\mathrm{d}\tau'\mathrm{d}\tau\;\mathrm{e}^{-\mathrm{i}(E-E_0)(\tau-\tau')}\,\langle\psi|\hat{\phi}\,(x(\tau))\,|0_M\rangle\,\langle 0_M|\hat{\phi}\,(x(\tau'))\,|\psi\rangle\;. \tag{2.26}$$

Using the completeness relation for final states, we can express the transition probability as

$$|\mathcal{M}|^2 \;=\; c^2\sum_{E}|\,\langle E|\hat{m}(0)|E_0\rangle\,|^2\mathcal{F}(E-E_0)\;, \tag{2.27}$$

where the response function $\mathcal{F}(E)$, which encodes the trajectory dependence of the transition probability, is defined as

$$\mathcal{F}(E) \;=\; \int\mathrm{d}\tau'\mathrm{d}\tau\;\mathrm{e}^{-\mathrm{i}E(\tau-\tau')}\mathcal{W}(\tau-\tau')\;, \tag{2.28}$$

in terms of the Wightman function

$$\mathcal{W}(\tau-\tau') \;=\; \langle 0_M|\hat{\phi}(x(\tau))\hat{\phi}(x(\tau'))|0_M\rangle\;. \tag{2.29}$$

For stationary processes, the Wightman function only depends on the time difference $\Delta\tau=\tau-\tau'$.

More generally, for stationary processes we can express the transition amplitude as

$$|\mathcal{M}|^2 \;=\; c^2\sum_{E}|\,\langle E|\hat{m}(0)|E_0\rangle\,|^2\int\mathrm{d}(\Delta\tau)\;\mathrm{e}^{-\mathrm{i}(E-E_0)\Delta\tau}\mathcal{W}(\Delta\tau)\;. \tag{2.30}$$

Note that the integral of the response function includes a formally infinite integral over τ which can be avoided by looking at the transition probability per unit time. Equation (2.30) shows that the response function is an integral part in determining the transition rate. For this reason, a major part of this chapter discusses the response function of scalar fields.

Most generally, the Wightman function of a scalar field in $3+1$ dimensions is given by

$$\mathcal{W}(\Delta\tau) \;=\; -\frac{1}{4\pi^2}\frac{1}{(\Delta\tau-\mathrm{i}\epsilon)^2-|x(\tau)-x(\tau')|^2}\;. \tag{2.31}$$

This expression has been regularised with $\Delta\tau\to\Delta\tau-\mathrm{i}\epsilon$ and is to be understood in the limit $\epsilon\to 0+$. A linearly accelerated trajectory is given by $x=(t^2+\alpha^2)^{1/2}$ with α constant and

$t = \alpha \sinh(\tau/\alpha)$, τ being the detector's proper time. This corresponds to the coordinate transformation in equation (2.3) with constant ξ. For this trajectory, the Wightman function in equation (2.31) is

$$\mathcal{W}(s) \;=\; -\frac{1}{16\pi^2}\frac{1}{\alpha^2 \sinh^2\left(\frac{s}{2\alpha} - \frac{\mathrm{i}\epsilon}{2\alpha}\right)} \,, \tag{2.32}$$

with $s = \Delta\tau$ and making use of a few trigonometric identities, one finds $(t-t')^2 - (x(t)-x(t'))^2 = 4\alpha^2 \sinh^2\left(\frac{\tau-\tau'}{2\alpha}\right)$ which can be substituted in equation (2.31). Note that equation (2.31) and (2.32) are indeed equal in the limit $\epsilon \to 0+$. In order to calculate the response function for this trajectory we may rewrite the sinh as a series to find [2]

$$\mathcal{W}(s) \;=\; -\frac{1}{4\pi^2}\sum_{k=-\infty}^{\infty} (s - \mathrm{i}\epsilon - 2\pi\mathrm{i}\alpha k)^{-2} \,. \tag{2.33}$$

Consequently, the response function as in equation (2.28) yields

$$\mathcal{F}(E) \;=\; -\frac{1}{4\pi^2}\sum_{k=-\infty}^{\infty}\int_{-\infty}^{\infty} \mathrm{d}s\, \mathrm{e}^{-\mathrm{i}Es}\,(s - 2\mathrm{i}\epsilon - 2\pi\mathrm{i}\alpha k)^{-2} \,. \tag{2.34}$$

As in most of the cases that will be discussed in this chapter, the response function can be calculated using the residue theorem (see appendix A.3). In the simplest case, this involves using the analytical continuation of the integrand and choosing an integration contour from $-R$ to R along the real axis and along a semi circle with radius R either in the upper or lower complex plane. The semi circle is chosen in such a way that its contribution vanishes in the limit $R \to \infty$, resulting in an integral along the real axis only. Using this approach shows that the response function for an inertial trajectory vanishes and, subsequently, no transition will take place, as expected.

Applying the above procedure to the response function of an accelerated trajectory, we can choose the integration contour along the real axis and a semi circle in the lower half plane for $E > 0$, enclosing the poles at $s = 2\mathrm{i}\epsilon + 2\pi\mathrm{i}\alpha k$, with $k < 0$. The contribution of the auxiliary semi circle vanishes taking the limit of its radius to infinity. Poles with $k > 0$ do not contribute to this integral. The residues at those poles in the limit $\epsilon \to 0$ can be calculated to be $-\mathrm{i}E \exp\{2\pi\alpha E k\}$. For $E < 0$, we choose the upper semi circle enclosing only the poles for non-negative k. In summary, the response function is given by

$$\mathcal{F}(E) \;=\; \frac{|E|}{2\pi}\Theta(-E) + \frac{|E|}{2\pi}\sum_{k=1}^{\infty} \mathrm{e}^{-2\pi\alpha|E|k} \,. \tag{2.35}$$

By adding and subtracting a 1 to the summation for $E > 0$, the sum is a geometric series such that both results for $E > 0$ and $E < 0$ can be summarised to

$$\mathcal{F}(E) \;=\; \frac{E}{2\pi}\frac{1}{\mathrm{e}^{2\pi\alpha E} - 1} \,. \tag{2.36}$$

[2] Using $\frac{1}{\sinh^2 \pi x} = \mathrm{cosec}^2 \pi x = \pi^{-2}\sum_{k=-\infty}^{\infty}(x - \mathrm{i}k)^{-2}$.

Now, we can substitute this into the expression for the excitation rate

$$|\mathcal{M}|^2 \;=\; \frac{c^2}{2\pi}\sum_E \frac{(E-E_0)|\,\langle E|\hat{m}(0)|E_0\rangle\,|^2}{\mathrm{e}^{2\pi\alpha(E-E_0)}-1}\,, \tag{2.37}$$

to see that the Bose factor indicates a distribution at temperature

$$T \;=\; \frac{1}{2\pi}a\,, \tag{2.38}$$

with acceleration $a=\alpha^{-1}$. The temperature of this accelerated trajectory can be expressed entirely in terms of the response function of the detector using Einstein's detailed balance condition [65]

$$\frac{1}{T} \;=\; \frac{1}{E}\ln\left(\frac{\mathcal{F}(-E)}{\mathcal{F}(E)}\right)\,. \tag{2.39}$$

The detailed balance condition in equation (2.39) is of central importance for the discussion in the following chapters. This condition utilises the excitation and de-excitation rates to define a temperature via their ratio. Even when the right-hand side of equation (2.39) depends on the energy gap E, we can still use this condition to define an effective temperature. Furthermore, we see that multiplying the response function by a factor that is either energy independent or even in energy leads to the same temperature. Any response function that is entirely even in E does not give rise to an Unruh temperature.

In a similar way to the approach in this chapter, we will extend the discussion of the Unruh temperature to circularly accelerated trajectories in both 3+1 and 2+1 dimensions. In particular, we will calculate response functions and Unruh temperatures utilising the residue approach as outlined in this section.

2.3 Circular Unruh Effect

In the previous section we saw how a linear acceleration gives rise to a thermal state with a characteristic temperature proportional to the acceleration. In this chapter we show that this effect occurs as well on circular trajectories. Although the speed v of this trajectory is constant, it is the circular acceleration that causes this effect. Instead of parametrising the trajectory as linear motion, we can specify the trajectory to be circular motion with radius R using the parametrisation with respect to proper time τ

$$X(\tau) \;=\; (\gamma\tau, R\cos(\gamma\Omega\tau), R\sin(\gamma\Omega\tau), \cdots)\;, \tag{2.40}$$

with angular velocity $\Omega = v/R$. Note that v is constant on a circular orbit, therefore the gamma factor $\gamma = 1/\sqrt{1-v^2}$ is constant as well. Proper and Minkowski time are therefore related by this constant gamma factor $t = \gamma\tau$, which will become helpful later when we talk about analogues. The dots in the d-dimensional parametrisation of $X(t)$ stand for $d-3$ zeroes. The magnitude of the proper acceleration is given by $a = \sqrt{\ddot{X}(\tau)^2} = \gamma^2 v^2/R$. If the expression for the linear Unruh temperature (2.1) effect held for the circular motion as well, we would find

$$k_{\mathrm{B}}T_{\mathrm{lin}} \;=\; \frac{\hbar}{2\pi c}\frac{v^2\gamma^2}{R}\;, \tag{2.41}$$

by simply substituting the expression for the circular acceleration into the equation for the linear Unruh temperature. We will calculate the exact Unruh temperature for a circular acceleration in this chapter, however, we will frequently refer to this linear motion prediction to determine to what extent the exact result differs from this simplified view. That this accelerated motion gives rise to the Unruh effect was shown in [21, 22]. In the following, we want to calculate the response of a detector on a circular trajectory in various dimensions as the distinction between two and three spatial dimensions will become important once we talk about the analogue Unruh effect. For that reason, we calculate the Wightman function for a massless scalar field in d dimensions [66] [3]

$$\mathcal{W}(s) \;=\; \frac{\Gamma\left(\frac{d}{2}-1\right)}{4\pi^{\frac{d}{2}}\left(\Delta x(s)^2\right)^{\frac{d-2}{2}}}\;, \tag{2.42}$$

where we have defined [4]

$$\left(\Delta x(s)\right)^2 \;:=\; \left(X(s)-X(0)\right)^2 \;=\; -\gamma^2 s^2 + 4R^2\sin^2\left(\frac{\gamma v}{2R}s\right)\;, \tag{2.43}$$

noting that $\Delta x(s) = \Delta x(-s)$. With $z = \frac{\gamma v}{2R}s$, this expression can be more conveniently rewritten as

$$\left(\Delta x(z)\right)^2 \;=\; -4R^2\left(\frac{z^2}{v^2}-\sin^2 z\right) \;=\; -4R^2\left(\frac{z}{v}-\sin z\right)\left(\frac{z}{v}+\sin z\right)\;. \tag{2.44}$$

[3] The gamma function is defined as $\Gamma(z) = \int_0^\infty \mathrm{d}t\; t^{z-1}\mathrm{e}^{-t}$ with $\Gamma(1) = 1$.
[4] Using $2\sin^2\frac{x}{2} = 1-\cos x$.

The response function in d dimensions is then given by

$$\mathcal{F}(E) \;=\; \int_{-\infty}^{\infty} \mathrm{d}s\; \mathrm{e}^{-\mathrm{i}Es} \frac{\Gamma\left(\frac{d}{2}-1\right)}{4\pi^{\frac{d}{2}}\left(\Delta x(s)^2\right)^{\frac{d-2}{2}}}\,. \tag{2.45}$$

In the following, we present how to calculate the response functions explicitly in various limiting regimes for a circular trajectory. From equation (2.45) we see that the behaviour of the response function is entirely specified by the pole structure of the Wightman function, which in turn is determined by the zeroes of (2.44) [67]. Note that, strictly speaking, this response function is the response function per unit time as it will be used for transition probabilities. The poles of the Wightman function are given by the solutions to

$$\frac{z}{v} \;=\; \pm \sin z\,. \tag{2.46}$$

The only real solution to that equation is at $z = 0$ which means that $(\Delta x(z))^2$ has a zero of order two at $z = 0$. In fact, this pole is quite crucial because it requires proper regularisation of the Wightman function. As it turns out, regularisation with $z \to z + \mathrm{i}\epsilon$ does not work in the case of an accelerated trajectory as it will give rise to time dependent transition rates [68]. Instead, we regularise the integral with $\Delta x(z) \to \Delta x(z) - \mathrm{i}\epsilon\Delta\dot{x}(z)$ understood in the limit $\epsilon \to 0+$ [69, 70]. This regularisation is a result of a smeared, finite size detector. The response function can then be written as

$$\mathcal{F}(E) \;=\; \frac{4R}{\gamma v}\mathrm{Re}\int_0^{\infty} \mathrm{d}z\; \mathrm{e}^{-\mathrm{i}\frac{2RE}{\gamma v}z} \frac{\Gamma\left(\frac{d}{2}-1\right)}{4\pi^{\frac{d}{2}}\left(\left(\Delta x(z) - \mathrm{i}\epsilon\Delta\dot{x}(z)\right)^2\right)^{\frac{d-2}{2}}}\,. \tag{2.47}$$

This integral can be split into several parts which makes calculations and interpretations slightly easier. A common split is to isolate a distributional component at $s = 0$ [69, 70]. Alternatively, it can be split into a contribution of the inertial motion response function $\mathcal{F}^{\mathrm{in}}(E)$ and corrections due to the circular motion $\mathcal{F}^{\mathrm{corr}}(E)$. We will see that the integral of the correction due to the circular motion can be calculated using the residue theorem. As such, this contribution will be equivalent to the sum of contributions at poles z_n, which we call $\mathcal{F}_n(E)$, with n summing over the residues. The response function is the sum of all separate contributions

$$\mathcal{F}(E) \;=\; \mathcal{F}^{\mathrm{in}}(E) + \mathcal{F}^{\mathrm{corr}}(E) \;=\; \mathcal{F}^{\mathrm{in}}(E) + \sum_n \mathcal{F}_n(E)\,. \tag{2.48}$$

The explicit form of those parts will be calculated later as we talk about the response functions in various dimensions. However, a common theme will be the pole structure of the Wightman function which will be inherently present in all dimensions. For this reason, we will briefly discuss the general structure of those poles. In all what follows we assume $E \neq 0$.

The function $\Delta x(z)^2$ is symmetric in z which means it is sufficient to look for zeroes in the upper complex plane. If we write z as the sum of imaginary and real part $z = \mathrm{i}(\alpha_n + \mathrm{i}\beta_n)$, equation (2.46) can be written as two equations

$$\alpha_n \;=\; \pm\, v \sinh\alpha_n \cos\beta_n\,, \tag{2.49a}$$

$$\beta_n \;=\; \pm\, v \cosh\alpha_n \sin\beta_n\,, \tag{2.49b}$$

by separation into real and imaginary parts.[5] There is only one pole with real part $\beta_0 = 0$ and imaginary part $\alpha_0 > 0$ which allows a parametrisation of v in terms of α_0

$$v = \frac{\alpha_0}{\sinh \alpha_0} . \tag{2.50}$$

Note, that we can use this result to write

$$\gamma = \frac{\sinh \alpha_0}{\sqrt{\sinh^2 \alpha_0 - \alpha_0^2}} . \tag{2.51}$$

Solving equation (2.49a) for β_n gives

$$\beta_n = \arccos\left(\pm \frac{\sinh \alpha_0}{\alpha_0} \frac{\alpha_n}{\sinh \alpha_n}\right) + 2\pi n , \tag{2.52}$$

where the additional term $2\pi n$, $n \in \mathbb{Z}$ appears due to the periodicity of the cosine. Using $\arccos(-x) = -\arccos(x) + \pi$ and $0 \leq \arccos(x) \leq \pi$ we can rewrite the equation above more conveniently as

$$\beta_n = (-1)^n \arccos\left(\frac{\sinh \alpha_0}{\alpha_0} \frac{\alpha_n}{\sinh \alpha_n}\right) + \pi n , \tag{2.53}$$

where even n correspond to the zeroes associated with the plus sign in equation (2.49a) and odd n correspond to the zeroes associated with the minus sign. With the help of the expression above for β_n, we can rewrite equation (2.49b) to find that α_n are the solutions to the following equation

$$\sqrt{1 - \left(\frac{\sinh \alpha_0}{\alpha_0} \frac{\alpha_n}{\sinh \alpha_n}\right)^2} \frac{\alpha_0}{\sinh \alpha_0} \cosh \alpha_n = \arccos\left(\frac{\sinh \alpha_0}{\alpha_0} \frac{\alpha_n}{\sinh \alpha_n}\right) + (-1)^n n\pi . \tag{2.54}$$

To get a feeling for those solutions, figure 2.2 shows the pole structure of the Wightman function for a circular trajectory in the complex plane as numerical results to equations (2.53) and (2.54).

The residue theorem allows us to choose an integration contour in the upper half of the complex plane of the integral appearing in the response function with which we can rewrite the integral as the sum over the enclosed residues of the Wightman function

$$\mathcal{F}_n(E) = 2\pi \mathrm{i} \operatorname*{Res}_{z_n} \left\{ \mathrm{e}^{-\mathrm{i}Ez} \mathcal{W}(z) \right\} . \tag{2.55}$$

The particular path $\mathcal{C}_1$ is shown in figure 2.2 whereas the contributions of auxiliary semi circles to close the integration contour vanish in the limit $R \to \infty$. We now want to compare how the circular Unruh effect manifests itself in different spacetime dimensions by considering different limits and compare the calculated circular Unruh temperature to equation (2.41). The general approach of the following sections is to determine the dominant behaviour of the response function of a detector on a circular trajectory in a specific regime and use the detailed balance condition to calculate the circular Unruh temperature. We will then compare this result to the naïve approach of using a circular acceleration for the linear Unruh temperature expression.

[5] Using $\sin \mathrm{i}x = \mathrm{i} \sinh x$ and $\cos \mathrm{i}x = \cosh x$.

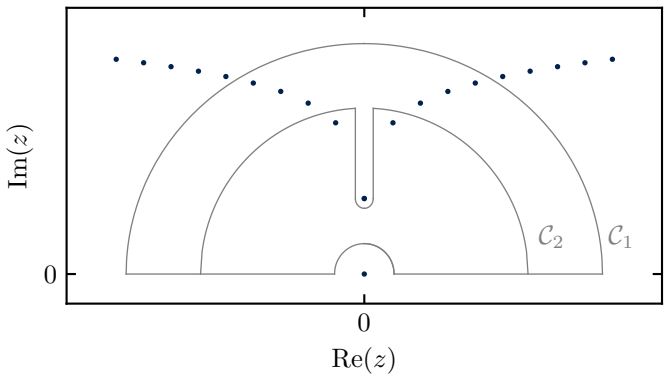

Figure 2.2 (Poles of Wightman Function) Poles for $z = v \sinh z$ with $z = \mathrm{i}(\alpha_n + \mathrm{i}\beta_n)$. Note, that the real pole at $(0, 0)$ has been regularised independently. The poles are symmetric with respect to the real axis. The graph only shows the poles with $\alpha_n > 0$ for $v = 0.4$. In addition, $\alpha_n < \alpha_{\pm(n+1)}$ and $|\beta_n| < |\beta_{\pm(n+1)}|$. The curves $\mathcal{C}_i$ are used as integration contours to calculate the response functions.

2.3.1 3 + 1 Dimensions

In $3 + 1$ dimensions, we have $\Gamma(1) = 1$ and equation (2.42) becomes

$$\mathcal{W}(s) \;=\; \frac{1}{4\pi^2}\frac{1}{(\Delta x(s))^2}\,, \tag{2.56}$$

which possesses poles at $(\Delta x(s))^2 = 0$. To calculate the response function explicitly, a few preparatory steps are necessary, which we will only briefly mention here (for details see [69]). First, using the regularisation approach of Schlicht [68], we note that the response function can be written as

$$\mathcal{F}(E) \;=\; \frac{1}{2\pi^2}\mathrm{Re}\int_0^\infty \mathrm{d}s \frac{\mathrm{e}^{-\mathrm{i}Es}}{(\Delta x(s) - \mathrm{i}\epsilon q)^2}\,, \tag{2.57}$$

with ϵ being the regularisation parameter in the limit $\epsilon \to 0$, $q = \dot{x}(\tau) + \dot{x}(\tau - s)$ and $\Delta x = x(\tau) - x(\tau - s)$. Then, separating the integral in parts that are even and odd in E, as well as taking the real part shows

$$\mathcal{F}^{\mathrm{even}}(E) \;=\; \frac{1}{2\pi^2}\int_0^\infty \mathrm{d}s\, \frac{\left((\Delta x)^2 - \epsilon^2 q^2\right)\cos(Es)}{\left(\epsilon^2 q^2 - (\Delta x)^2\right)^2 + 4\epsilon^2 (q\cdot\Delta x)^2}\,, \tag{2.58a}$$

$$\mathcal{F}^{\mathrm{odd}}(E) \;=\; \frac{1}{\pi^2}\int_0^\infty \mathrm{d}s\, \frac{\epsilon(q\cdot\Delta x)\sin(Es)}{\left(\epsilon^2 q^2 - (\Delta x)^2\right)^2 + 4\epsilon^2 (q\cdot\Delta x)^2}\,. \tag{2.58b}$$

Those integrals can be split into a part with $s \in [0, \sqrt{\epsilon}]$ and $s \in [\sqrt{\epsilon}, \infty]$. For small s, q and Δx as well as their product can be expanded in powers of s. Carefully keeping track of powers of ϵ, it can be shown that the integrals above are perfectly well defined in the limit $\epsilon \to 0$ for which

we eventually obtain [69]

$$\mathcal{F}(E) \;=\; -\frac{E}{4\pi} + \frac{1}{2\pi^2}\int_0^\infty \mathrm{d}s\, \left(\frac{\cos(Es)}{(\Delta x)^2} + \frac{1}{s^2}\right) . \tag{2.59}$$

Finally, adding and subtracting $\cos(Es)/s^2$ in the integral shows that [6]

$$\mathcal{F}(E) \;=\; -\frac{E}{2\pi}\Theta(-E) + \frac{1}{2\pi^2}\int_0^\infty \mathrm{d}s\, \cos(Es)\left(\frac{1}{(\Delta x)^2} + \frac{1}{s^2}\right) , \tag{2.60}$$

where we recognise the response function of an inertial trajectory as the first part (see appendix) and corrections due to the circular motion as the second part.

The correction term of the response function can best be evaluated using the residue theorem. Analytical continuation in the complex plane and choosing the integration contour $\mathcal{C}_1$ as outlined in figure 2.2 yields

$$\mathcal{F}(E) \;=\; -\frac{E}{2\pi}\Theta(-E) - \frac{1}{8\pi^2\gamma v R}\oint_{\mathcal{C}} \mathrm{d}z\, \frac{\exp\left\{\mathrm{i}\frac{2ER}{\gamma v}z\right\}}{\frac{z^2}{v^2} - \sin^2 z} . \tag{2.61}$$

Note that this expression uses the substitution $z = \frac{\gamma v}{2R}s$ and that the contour excludes the pole at $s = 0$. As we have set the scene, we can turn our attention to various limits of E and v.

Large Gap Limit. Consider the limit $|E| \to \infty$ with fixed v and R. As $\alpha_n < \alpha_{\pm(n+1)}$, we see that the integrand appearing in the response function scales with $\sim \exp\{-Ez\}$, which suppresses the effect of higher order residues in this limit. We can therefore evaluate the integral at residue $z_0 = -\mathrm{i}\alpha_0$ only

$$\mathcal{F}_0(E) \;=\; \frac{v}{8\pi\gamma R}\frac{\mathrm{e}^{-E\frac{2R}{\gamma v}\alpha_0}}{(\alpha_0 - v^2\sinh\alpha_0\cosh\alpha_0)} . \tag{2.62}$$

This explicit expression allows us to calculate the Unruh temperature of a circular orbit in the large gap limit as

$$\frac{1}{T_{\mathrm{circ}}} \;=\; \frac{1}{E}\ln\left(\frac{4\gamma R|E|}{v}\left(\alpha_0 - v^2\sinh\alpha_0\cosh\alpha_0\right)\mathrm{e}^{|E|\frac{2R}{\gamma v}\alpha_0} - 1\right) \;\to\; \frac{2R\alpha_0}{\gamma v} , \tag{2.63}$$

where the dominant contribution comes from the exponential in the logarithm, whose exponent therefore determines the Unruh temperature. By explicitly using the form of γ in equation (2.51), we write this more conveniently as

$$T_{\mathrm{circ}} \;=\; \frac{1}{2\sqrt{\sinh^2\alpha_0 - \alpha_0^2}\,R} . \tag{2.64}$$

The circular Unruh temperature in $3+1$ dimensions only depends on the radius R of the trajectory and on the orbital speed v, implicitly through α_0. Replacing v in the equation for

[6] Using the integral in appendix 2.1.2

the prediction of the linear motion Unruh temperature yields

$$T_{\text{lin}} \;=\; \frac{v^2\gamma^2}{2\pi R} \;=\; \frac{\alpha_0^2}{2\pi R\left(\sinh^2\alpha_0 - \alpha_0^2\right)} \,. \tag{2.65}$$

Hence, the ratio of the linear and circular temperature is given by

$$\frac{T_{\text{circ}}}{T_{\text{lin}}} \;=\; \frac{\pi\sqrt{\sinh^2\alpha_0 - \alpha_0^2}}{\alpha_0^2} \,. \tag{2.66}$$

Note that for a given velocity, or equivalently for a given acceleration and trajectory radius, we can solve equation (2.50) numerically for α_0 and calculate the ratio above explicitly.

Small Gap Limit. In the small gap limit we consider $E \to 0$ while keeping v and R fixed. As the integral in (2.60) is continuous in E we can apply a dominated convergence argument (see appendix A.4) with which we can take the limit $E \to 0$ under the integral. Only keeping the lowest order in E shows that

$$\mathcal{F}(E) \;=\; -\frac{E}{2\pi}\Theta(-E) + \frac{1}{2\pi^2}\int_0^\infty \mathrm{d}s\, \left(\frac{1}{(\Delta x)^2} + \frac{1}{s^2}\right) \,. \tag{2.67}$$

Again, using the detailed balance condition, we find

$$T_{\text{circ}} \;=\; E\ln\left(1 - \frac{2\pi ER}{\gamma v\int_0^\infty \mathrm{d}z\, \left(\frac{1}{z^2} - \frac{1-v^2}{z^2 - v^2\sin^2 z}\right)}\right)^{-1} \,, \tag{2.68}$$

which can be simplified using the Taylor expansion of the logarithm only keeping the lowest order in E [7]

$$T_{\text{circ}} \;=\; \frac{\gamma v}{2\pi R}\int_0^\infty \mathrm{d}z\, \left(\frac{1}{z^2} - \frac{1-v^2}{z^2 - v^2\sin^2 z}\right) \,. \tag{2.69}$$

The ratio of the circular to linear motion temperature can be calculated to

$$\frac{T_{\text{circ}}}{T_{\text{lin}}} \;=\; \frac{\sqrt{1-v^2}}{v}\int_0^\infty \mathrm{d}z\, \left(\frac{1}{z^2} - \frac{1-v^2}{z^2 - v^2\sin^2 z}\right) \,. \tag{2.70}$$

In the paragraphs above, we calculated the ratio of circular and linear prediction Unruh temperature as a function of v, or α_0 equivalently. Now, we want to look at the behaviour for specific asymptotics of v.

Ultra-Relativistic Limit. If the orbital speed of the detector approaches the speed of light, we see from the parametrisation of $v = \alpha_0/\sinh\alpha_0$ that $\alpha_0 \to 0$ for $v \to 1$ [71, 61]. All other α_n and β_n with $n \neq 0$ are non-zero. In this ultra-relativistic limit we can re-express relevant expressions in terms of α_0 by expanding the hyperbolic sine, only keeping lowest order terms in

[7] The Taylor expansion for the logarithm at $x = 0$ is $\ln(1+x) = \sum_n \frac{(-1)^{n-1}}{n}x^n$.

α_0, and use the parametrisation for v to find [8]

$$v = 1 + \frac{1}{6}\alpha_0^2 + \mathcal{O}\left(\alpha_0^4\right) , \tag{2.71a}$$

$$a = \frac{3}{\alpha_0^2 R}\left(1 + \mathcal{O}\left(\alpha_0^4\right)\right) , \tag{2.71b}$$

$$\frac{1}{\gamma v} = \frac{\alpha_0}{\sqrt{3}}\left(1 + \mathcal{O}\left(\alpha_0^2\right)\right) . \tag{2.71c}$$

Using the above expansions we find [9]

$$\mathcal{F}_0(E) = \frac{\sqrt{3}\exp\left(-\frac{2\alpha_0|E|R}{\gamma v}\right)}{8\pi R\alpha_0^2}\left(1 + O(\alpha_0^2)\right) , \tag{2.72}$$

while all other terms are [71] (see appendix (2.23))

$$\mathcal{F}_{n>0}(E) = O\left(\alpha_0 \exp\left(-\frac{2\alpha_1|E|R}{\gamma v}\right)\right) . \tag{2.73}$$

Keeping only the leading $v \to 1$ behaviour yields

$$\mathcal{F}(E) = -\frac{E}{2\pi}\Theta(-E) + \frac{\sqrt{3}\exp\left(-\frac{2\alpha_0|E|R}{\gamma v}\right)}{8\pi R\alpha_0^2} . \tag{2.74}$$

As before, the Unruh temperature can be calculated using the detailed balance condition

$$T_{\text{circ}} = \frac{|E|}{\ln\left(1 + \frac{4\sqrt{3}\,|E|}{a}\exp\left(\frac{2\sqrt{3}\,|E|}{a}\right)\right)} , \tag{2.75}$$

where equation (2.71b) has been used for a. This expression shows that T_{circ}/a is a function of $|E|/a$, where the dependence on v and R is implicitly present through a. Note that in natural units the ratio E/a is dimensionless

Conclusion. Figure 2.3 (a) shows the numerical result for the ratio of circular and linear Unruh temperature as given in equation (2.60) for $v \in (0,1)$ and $E/a \in (0,3)$, excluding the endpoints of either interval. We see that this ratio vanishes for small v and E/a and grows to a maximum for small v and large E/a. In the remaining range it mostly lies between 1 and 2. In addition we see that for large energy gaps in the ultra relativistic limit $v \to 1$ (figure 2.3 (b)), we have $\alpha_0 \to 0$, and we find that $T_{\text{circ}}/T_{\text{lin}} = \pi/\sqrt{3} \approx 1.8$. On the other hand in the ultra-relativistic limit, the ratio of circular and linear Unruh temperature approaches $T_{\text{circ}}/T_{\text{lin}} \approx \pi/(2\sqrt{3}) \approx 0.9$ for $|E|/a \ll 1$ and is strictly below $T_{\text{circ}}/T_{\text{lin}} \approx \pi/\sqrt{3} \approx 1.8$.

[8] The Taylor expansion for hyperbolic sine at $x = 0$ is $\sinh x = \sum_n \frac{x^{2n+1}}{(2n+1)!}$.

[9] Using the lowest order contributions of the Taylor expansions at $x = 0$ for $\sinh x = \sum_n \frac{x^{2n+1}}{(2n+1)!}$ and $\cosh x = \sum_n \frac{x^{2n}}{(2n)!}$

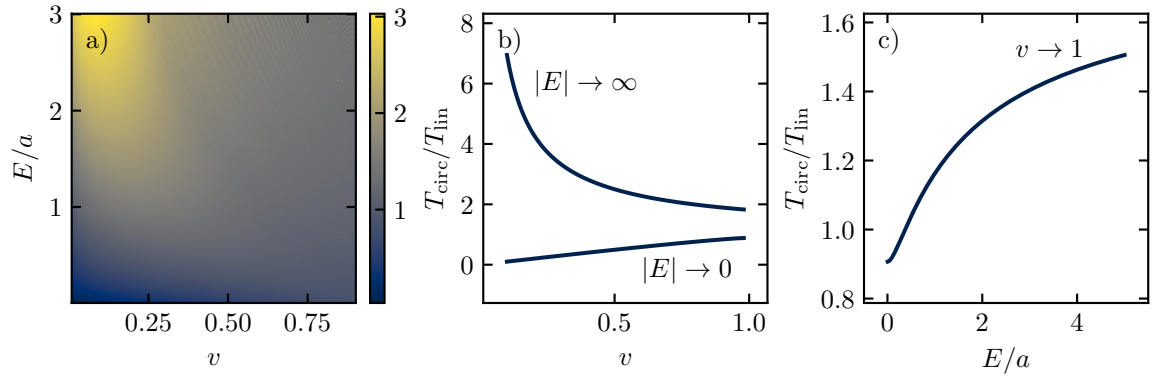

Figure 2.3 (Circular Unruh temperature in 3 + 1 dimensions) a) Full plot of $T_{\mathrm{circ}}/T_{\mathrm{lin}}$ in $3+1$ dimensions using detailed balance and equation (2.60), b) Large gap and small gap limit of $T_{\mathrm{circ}}/T_{\mathrm{lin}}$, c) $T_{\mathrm{circ}}/T_{\mathrm{lin}}$ over E/a in ultra-relativistic limit $v \to 1$.

2.3.2 2 + 1 Dimensions

In this section, we present the derivation of the circular Unruh temperature in $2+1$ dimensions and various asymptotic limits, which has not been presented to that extent in the literature so far. In $2+1$ dimensions, the Wightman function of equation (2.42) for $d = 3$ gives

$$\mathcal{W}(s) \;=\; \frac{1}{4\pi}\frac{1}{\sqrt{(\Delta \mathrm{x}(s))^2}} \;=\; \frac{1}{4\pi}\frac{1}{\sqrt{-4R^2\left(\frac{\gamma^2 s^2}{4R^2} - \sin^2(\gamma\Omega s)\right)}}\,. \tag{2.76}$$

The discussion of the response function in terms of higher residues turns out to be more cumbersome than in the four dimensional case and we will avoid it wherever possible. For the purpose of this discussion, we write this integral as [72]

$$\mathcal{F}(E) \;=\; \frac{1}{4} - \frac{1}{2\pi}\int_0^\infty \mathrm{d}s\, \frac{\sin(Es)}{\sqrt{-(\Delta x(s))^2}}\,, \tag{2.77}$$

where the square root in the denominator is now positive. In principle, the approach to derive this equation is equivalent to the case of the $(3+1)$-dimensional response function. First, separate the response function in even and odd contributions in E. Then, split the integration into two parts, with one ranging from 0 to $\sqrt{\epsilon}$, and the second one from $\sqrt{\epsilon}$ to ∞. Carefully keeping track of all relevant orders of ϵ and finally taking the limit $\epsilon \to 0$ shows the result above. Using the substitution $z = \frac{\gamma v}{ER}s$ we may write

$$\mathcal{F}(E) \;=\; \frac{1}{4} - \frac{1}{2\pi\gamma v}\int_0^\infty \mathrm{d}z\, \frac{\sin\left(\frac{2ER}{\gamma v}z\right)}{\sqrt{\frac{z^2}{v^2} - \sin^2 z}}\,. \tag{2.78}$$

Alternatively, adding and subtracting $\sin(Es)/s$ in the integral results in the split

$$\mathcal{F}(E) \;=\; \frac{1}{2}\Theta(-E) + \frac{1}{2\pi\gamma v}\int_0^\infty \mathrm{d}z\; \sin\left(\frac{2ER}{\gamma v}z\right)\left(\frac{\gamma v}{z} - \frac{1}{\sqrt{\frac{z^2}{v^2}-\sin^2 z}}\right)\,, \tag{2.79}$$

where the first contribution is the inertial motion response function in $2+1$ dimensions (see appendix 2.1.1) and the second part corrections come from the circular motion response. Again, note the beauty of this approach, as the integrals are free of singularities and regularisation parameters.

The contribution due to the circular motion is equivalent to the integral

$$\mathcal{F}^{\text{corr}}(E) \;=\; \frac{\mathrm{i}\,\mathrm{sgn}(E)}{4\pi\gamma v}\int_{\mathcal{C}_1}\mathrm{d}z\;\frac{\exp\left(\mathrm{i}\frac{2|E|R}{\gamma v}z\right)}{\sqrt{z^2/v^2-\sin^2 z}}\,, \tag{2.80}$$

where the contour $\mathcal{C}_1$ is chosen as shown in figure 2.2. As the notation at the beginning of this chapter indicates, this integral can be represented as the sum of contributions from residues by deforming the integration contour to the upper half-plane and along the real axis. As the explicit form for residues with $n \neq 0$ will not be needed, we see that the exponential function suppresses residues with large imaginary part. Therefore, we focus on the contribution from the residue at $z_0 = \mathrm{i}\alpha_0$

$$\mathcal{F}_0(E) \;=\; \frac{\mathrm{sgn}(E)}{2\pi\gamma v}\int_{\alpha_0}^\infty \mathrm{d}\alpha\;\frac{\exp\left(-\frac{2|E|R}{\gamma v}\alpha\right)}{\sqrt{\sinh^2\alpha-\alpha^2/v^2}}\,, \tag{2.81}$$

where square roots are taken to be with positive real parts. The expression above can be calculated evaluating the integral in equation (2.80) along the contour $\mathcal{C}_2$ in figure 2.2. The residue theorem tells us that this integral has to be equal to the sum of all residues with $n \neq 0$. We can therefore calculate the residue for $n = 0$ by subtracting this result from the result obtained with integration contour $\mathcal{C}_1$ such that in the limit for ϵ radii to zero and R radii to infinity

$$\mathrm{Res}_{z_0}(F^{\text{corr}}) \;=\; -2\mathrm{i}\int_{\alpha_0}^\infty \mathrm{d}\alpha\;\frac{\exp\left(-\frac{2|E|R}{\gamma v}\alpha\right)}{\sqrt{\sinh^2\alpha-\alpha^2/v^2}}\,. \tag{2.82}$$

This shows the result above for $\mathcal{F}_0(E)$. As in the previous section, we will now turn our attention to various limits of the response function by varying one parameter while keeping the other parameters fixed.

Large Gap Limit. Equivalent to the calculations in $3+1$ dimensions, the correction in the response function for $|E| \to \infty$ in $2+1$ dimensions is dominated by the contribution of the lowest order residue at $z_0 = \mathrm{i}\alpha_0$ of equation (2.81). Changing the integration variable from α to y with $\alpha_0(1+y^2)$ results in an exponent that is quadratic in y such that we approximate this integral using Laplace's method (see appendix A.1). The expansion at $y = 0$ shows that

$$\mathcal{F}_0(E) \;=\; (8\pi\gamma v R\alpha_0|E|)^{-1/2}\,\frac{\mathrm{sgn}(E)}{\sqrt{2\alpha_0\sinh\alpha_0\cosh\alpha_0 - 2\alpha_0^2/v^2}}\exp\left\{-\frac{2|E|R}{\gamma v}\alpha_0\right\}\,. \tag{2.83}$$

To arrive at this result we used trigonometric identities[10] and Taylor expansions to calculate the limit for $y \to 0$. Calculating the Unruh temperature by using the detailed balance condition yields

$$T_{\text{circ}} = \frac{\gamma v}{4R\alpha_0} . \tag{2.84}$$

This expression is the same as in $3+1$ dimensions.

Small Gap Limit. Now we take the small gap limit with $E \to 0$ and fixed v and R. The circular motion correction to the response function is given by the second part in equation (2.79) and can be rewritten by adding a $\sin\left(\frac{2ER}{\gamma v}z\right)/z$ and subtracting it again under the integral. Doing this, we find [11]

$$\mathcal{F}^{\text{corr}}(E) = \frac{\gamma-1}{4\gamma}\operatorname{sgn}(E) + \frac{ER}{\pi\gamma^2 v}\int_0^\infty \mathrm{d}z \frac{\sin\left(\frac{2ER}{\gamma v}z\right)}{\frac{2ER}{\gamma v}z}\left(1 - \frac{z}{\sqrt{z^2 - v^2\sin^2 z}}\right) . \tag{2.85}$$

As we are interested in the small gap limit, we have already rewritten the integrand in a way that allows us to take the limit $E \to 0$ under the integral, showing that the whole integral is $\mathcal{O}(E)$ and therefore

$$\mathcal{F}^{\text{corr}}(E) = \frac{\gamma-1}{4\gamma}\operatorname{sgn}(E) + O(E) . \tag{2.86}$$

Using detailed balance and the complete expression for $\mathcal{F}(E)$, we then have

$$T_{\text{circ}} = \frac{|E|}{\ln\left(\frac{\gamma+1}{\gamma-1}\right)}(1 + O(E)) . \tag{2.87}$$

An important consequence of this expression is that the Unruh temperature is dependent on the absolute value of the energy gap with $T_{\text{circ}} \to 0$ as $E \to 0$. As a result, the circular motion temperature in this limit is significantly lower than the corresponding result in $3+1$ dimensions.

Ultra-Relativistic Limit with Fixed E/a. In this section we look at the limit $v \to 1$ for fixed E/a. Starting from equation (2.81), this limit is equivalent to $\alpha_0 \to 0$ with fixed $2ER\alpha_0/(\gamma v)$ which is again dominated by the lowest residue of the correction to the response function. After the substitution $\alpha = \alpha_0 y$, we find

$$\mathcal{F}_0(E) = \frac{\operatorname{sgn}(E)}{2\pi\alpha_0\gamma v}\int_1^\infty \mathrm{d}y \frac{\exp\left\{-\frac{2|E|R\alpha_0}{\gamma v}y\right\}}{\sqrt{\alpha_0^{-4}\left(\sinh^2(\alpha_0 y) - y^2\sinh^2\alpha_0\right)}} . \tag{2.88}$$

The square root in the denominator converges to $\frac{1}{3}y^2(y^2-1)$ for $\alpha_0 \to 0$. Note that in the exponent of the exponential we can use $R = \gamma^2 v^2/a$ and the limit $1/(\gamma v) \to \alpha_0/\sqrt{3}$ as shown in

[10] Namely, $\sinh(x+y) = \sinh x\cosh y + \cosh x\sinh y$.
[11] Using $\int_0^\infty \mathrm{d}z \frac{\sin bz}{z} = \frac{\pi}{2}\operatorname{sgn} b$ as shown in appendix 2.1.1.

equations (2.71) to arrive at

$$\mathcal{F}_0(E) \;=\; \frac{\mathrm{sgn}(E)}{2\pi}\int_1^\infty \mathrm{d}y\;\frac{\exp\left\{-2\sqrt{3}\frac{|E|}{a}y\right\}}{y\sqrt{y^2-1}}\;. \tag{2.89}$$

We show in appendix 2.2.2 that this integral can be written as

$$\mathcal{F}_0(E) \;=\; \frac{1}{4}\,\mathrm{sgn}(E) - \frac{1}{2\pi}\int_0^\infty \mathrm{d}s\frac{\sin\left(2\sqrt{3}s\frac{E}{a}\right)}{s\sqrt{s^2+1}}\;. \tag{2.90}$$

In the case of a response function dominated by the z_0 residue behaviour, the detailed balance condition yields

$$T_{\mathrm{circ}} \;=\; |E|\,\ln\left(\frac{1+\frac{2}{\pi}\int_0^\infty \mathrm{d}s\frac{\sin\left(2\sqrt{3}s\frac{E}{a}\right)}{s\sqrt{s^2+1}}}{1-\frac{2}{\pi}\int_0^\infty \mathrm{d}s\frac{\sin\left(2\sqrt{3}s\frac{E}{a}\right)}{s\sqrt{s^2+1}}}\right)^{-1}\;. \tag{2.91}$$

Conclusion. Figure (2.4) (a) shows the ratio of the circular to linear Unruh temperature for $v \in (0,1)$ and $E/a \in (0,3)$. The large gap limit in $2+1$ dimensions is the same as in $3+1$ dimensions (see figure 2.4 (b)) with $T_{\mathrm{circ}}/T_{\mathrm{lin}} \approx 1.8$ for $|E| \to \infty$ and $v \to 1$. However, we see that the circular Unruh temperature in the small gap limit is proportional to the energy gap, thus, vanishing in the limit $|E| \to 0$. In the ultra-relativistic limit, the ratio approaches $T_{\mathrm{circ}}/T_{\mathrm{lin}} \approx 1.8$ for $E/a \to \infty$ and falls of with $1/(E/a)$ for $E/a \to 0$ where it finally reaches zero for $E/a = 0$.

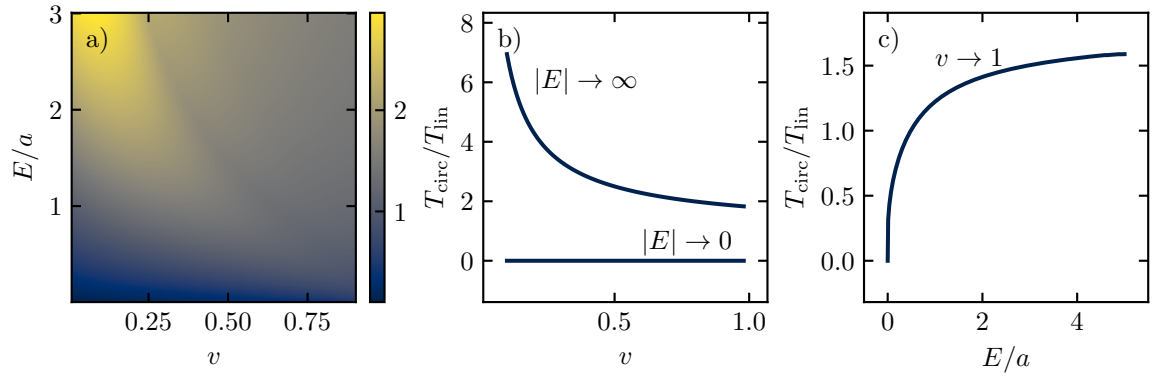

Figure 2.4 (Circular Unruh temperature in $(2+1)$d) a) Full plot of $T_{\mathrm{circ}}/T_{\mathrm{lin}}$ using detailed balance and equation (2.79) , b) Large gap and small gap limit of $T_{\mathrm{circ}}/T_{\mathrm{lin}}$ over v, c) $T_{\mathrm{circ}}/T_{\mathrm{lin}}$ over E/a in ultra-relativistic limit $v \to 1$.

2.4 Continuous Detectors

We saw in the previous chapter that a two-level system can act as a particle detector, whose excitation and de-excitation rates are sensitive to the trajectory on which it moves. In view of potential implementations in physical systems, we present an extended description of this traditional picture of Unruh detectors to continuous fields and show that the same signature can be obtained. In essence, the two-level system of an Unruh-DeWitt detector is replaced by a continuous scalar field. These scalar fields arise naturally in our analogue models, which is why we want to introduce them mathematically in this section. Consider a system of two real scalar fields ψ and ϕ with the Lagrangian

$$L = \frac{1}{2}\int \mathrm{d}z \left(\frac{1}{c^2}\left(\partial_t\psi(t,z)\right)^2 - \left(\partial_z\psi(t,z)\right)^2\right) + \frac{1}{2}\int \mathrm{d}\boldsymbol{x} \left(\frac{1}{c_s^2}\left(\phi(t,\boldsymbol{x})\right)^2 - \left(\nabla\phi(t,\boldsymbol{x})\right)^2\right) - \varepsilon \int \mathrm{d}\boldsymbol{x}\mathrm{d}z\, \partial_t\psi(t,z)\phi(t,\boldsymbol{x})\delta(\boldsymbol{x}-\boldsymbol{X}(t))\delta(z)\ . \quad (2.92)$$

This system consists of the free Lagrangians for two scalar fields one of which propagates with speed c in z direction, the second one with speed c_s in the (x, y) plane. The coupling between both fields is described by a coupling constant ϵ and a time derivative coupling between both fields. Variation of the action $S = \int \mathrm{d}t\ L$ gives rise to the equation of motion for $\psi(t, z)$

$$\frac{1}{c^2}\partial_t^2\psi(t,z) - \partial_z^2\psi(t,z) = \epsilon\delta(z)\partial_t\phi(t,\boldsymbol{X}(t))\ . \quad (2.93)$$

This equation shows that a non-zero interaction between both fields alters the free field equation of motion by an additive term that is proportional to the coupling constant ϵ. In the limit $\epsilon \to 0$ the free field equation of motion is recovered. Furthermore, we see that the equation of motion for ψ has a contribution from the ϕ field and so will the equation of motion for ϕ contain a contribution from ψ. ψ changes the dynamics of ϕ which in return changes the dynamics of ψ – a phenomenon known as back-action. The equation above considers only the free field dynamics of ϕ contributing to the dynamics of ψ and as such is therefore just an approximation, neglecting back-action. This equation can be solved by the means of the Greens function for the operator $\partial_t^2 - c^2\partial_z^2$, given by

$$G(t-t', z-z') = \frac{1}{2c}\Theta(t-t'-|z-z'|)\ , \quad (2.94)$$

with Θ being the Heaviside function, such that the solution to the equation of motion is given by

$$\psi(t,z) = \epsilon\int \mathrm{d}t'\mathrm{d}z'\ G(t-t', z-z')\delta(z')\partial_{t'}\phi(t', \boldsymbol{X}(t'))\ . \quad (2.95)$$

The z integration is facilitated by the delta distribution and after a partial integration on the t coordinate, noting that the derivative of the Heaviside function is a delta distribution, we find

$$\psi(t,z) = \psi_0(t,z) + \frac{\epsilon c}{2}\phi\left(t-|z|, \boldsymbol{X}(t-|z|)\right)\ , \quad (2.96)$$

where $\psi_0(t, z)$ is the solution of equation (2.93) with $\epsilon = 0$. As suggested already by the equation of motion, the explicit solution for ψ shows that it carries a contribution from ϕ pulled back to the point of interaction in the $z = 0$ plane.

In a similar fashion to the two-level detector model, we can calculate the excitation rate of the detector field ψ from a ground state $|0\rangle$ to an excited state $|E\rangle$ using the mode expansions for scalar fields

$$\hat{\psi}(t,z) = \int \frac{\mathrm{d}k}{\sqrt{2\omega_k}} \left(\hat{a}_k \mathrm{e}^{-\mathrm{i}(\omega_k t - kz)} + \hat{a}_k^\dagger \mathrm{e}^{\mathrm{i}(\omega_k t - kz)}\right) , \tag{2.97a}$$

$$\hat{\phi}(t,\boldsymbol{x}) = \frac{1}{\sqrt{2\pi}} \int \frac{\mathrm{d}^2 k}{\sqrt{2\omega_k}} \left(\hat{b}_{\boldsymbol{k}} \mathrm{e}^{-\mathrm{i}(\omega_k t - \boldsymbol{k}\cdot\boldsymbol{x})} + \hat{b}_{\boldsymbol{k}}^\dagger \mathrm{e}^{\mathrm{i}(\omega_k t - \boldsymbol{k}\cdot\boldsymbol{x})}\right) . \tag{2.97b}$$

Using first order perturbation theory we find for the transition amplitude

$$\mathcal{M} = -\frac{\epsilon\sqrt{\tilde{\omega}}}{\sqrt{2}} \int \mathrm{d}t\, \mathrm{e}^{\mathrm{i}\tilde{\omega}t} \langle \Omega | \phi(t, \boldsymbol{x}(t)) | 0 \rangle , \tag{2.98}$$

where $|0\rangle$ is short for the vacuum state of both fields and $|\Omega\rangle$ is short for the excited $|E\rangle$ of the ψ field and any state of the ϕ field. The ψ-mode frequency is denoted by $\tilde{\omega} = K > 0$ and the ϕ mode frequency is denoted by $\omega = c|\boldsymbol{k}|$. Following the process as outlined before, we take the squared modulus of (2.98) and sum over all possible final states for ϕ . Using the stationarity of the circular trajectory to factor out the total observation time, one obtains the transition probability per unit time

$$|\mathcal{M}|^2 = \frac{\epsilon^2 \tilde{\omega}}{2} \int \mathrm{d}s\, \mathrm{e}^{-\mathrm{i}\tilde{\omega}s} \mathcal{W}(s) , \tag{2.99}$$

where $\mathcal{W}(s)$ is the ϕ field Wightman function evaluated on the interaction trajectory

$$\mathcal{W}(s) = \langle 0 | \phi(s, \mathbf{X}(s)) \phi(0, \mathbf{X}(0)) | 0 \rangle . \tag{2.100}$$

We see that this transition amplitude has exactly the same form as the one derived in equation (2.30) for a discrete energy gap detector: it vanishes for inertial trajectories.

Interestingly, these calculations show that a continuous scalar field propagating in $1+1$ dimensions that couples to a $(2+1)$-dimensional scalar field with an interaction given by

$$\mathcal{L}_{\text{int}} = -\varepsilon \partial_t \psi(t,z) \phi(t, \boldsymbol{x}) \delta(\boldsymbol{x} - \boldsymbol{X}(t)) \delta(z) , \tag{2.101}$$

exhibit the same behaviour as a traditional Unruh-DeWitt detector. These continuous detectors allow for a completely new range of physical systems to probe for the Unruh effect, in particular in view of its implementation in analogue systems.

That continuous fields can act as a particle detector is a new perspective on this matter and hasn't been pointed out to that extent in the literature so far. The presence of this interaction term in the Lagrangian leads to additional excitations in the probing field which can be calculated using perturbation theory. The transition probability per unit time of this process has the same dependence on the interaction trajectory as that of a pointlike two-state system coupled to ϕ along the trajectory [4]: the ψ field acts as a detector for fluctuations of the ϕ field along the interaction trajectory. Furthermore, this transition amplitude vanishes for any inertial trajectory $X(\tau)$, as we would expect from an Unruh detector.

2.5 Towards Analogue Systems

In the previous chapters we have seen how the traditional understanding of an Unruh-DeWitt detector can be extended to continuous detectors. Those detectors open up a wide range of potential physical systems in which they can be implemented to detect the Unruh effect. As we will see in chapter III, due to the quantum nature of physical systems at low temperatures, condensed matter systems prove to be particularly suitable to probe characteristics of the quantum vacuum. In particular, we will have a look at Bose-Einstein condensates [36, 37, 38, 39] and superfluid Helium [40, 41, 73]. As we will see, the analogy to the continuous detector model arises naturally in a certain regime of the parameter space as an effective field theory in $(2+1)$ dimensions [55]. The beauty of analogue systems, in particular regarding the Unruh effect, is that the speed of light is replaced with the speed of sound in those systems. The drastic difference between the order of magnitude justifies the hope to be able to detect the Unruh effect in those laboratory systems. We now want to take the results derived in the previous chapters and apply them to analogue systems. We are interested in how the expressions for the circular Unruh temperature change in analogue systems. The energy of the moving detector is now defined with respect to the laboratory time.

A notable difference of the continuous detector presented in this chapter is the time derivative coupling compared to the coupling of a standard Unruh-DeWitt detector. However, this time derivative contributes with a factor E^2 to the response function and as we are interested in the temperature using the detailed balance condition (2.39) this factor cancels out in the ratio of excitation and de-excitation rates. We now want to consider an Unruh-DeWitt detector that is coupled linearly to a field with excitations given by a phonon-like dispersion relation.

In addition, we will use this framework to describe experimental setups in a laboratory. Thus, we need a non-relativistic description of these processes. In order to do so, we write

$$\widetilde{E} = \frac{E}{\gamma} \quad , \quad \widetilde{T} = \frac{T}{\gamma} \quad , \quad \widetilde{a} = \frac{a}{\gamma^2} \, , \tag{2.102}$$

to go from relativistic quantities to quantities with respect to the laboratory frame which is indicated with a tilde. We will refer to the quantities that are measured with respect to the laboratory time as analogue quantities. The prediction for the linear acceleration, analogue Unruh temperature is

$$\widetilde{T}_{\text{lin}} \;=\; \frac{T_{\text{lin}}}{\gamma} \;=\; \frac{\hbar\gamma\widetilde{a}}{2\pi c} \, , \tag{2.103}$$

where in the last step we assume a circular acceleration $\widetilde{a} = v^2/R$, with velocity v and radius R. The detailed balance condition then becomes

$$\frac{1}{\widetilde{T}} \;=\; \frac{1}{\widetilde{E}} \ln\left(\frac{\mathcal{F}(-\gamma\widetilde{E})}{\mathcal{F}(\gamma\widetilde{E})}\right) \, . \tag{2.104}$$

The response function $\mathcal{F}$ is the same as in the relativistic setup which has been calculated in this chapter. Again, we now compare the exact solution for the analogue, circular Unruh temperature to the analogue linear prediction in various dimensions. We will focus on the numerical solution and only look at the asymptotic behaviour relevant for future analogue setups.

3 + 1 Dimensions. In $3+1$ spacetime dimensions we use the result of equation (2.60) with $E/a = \widetilde{E}/(\gamma\widetilde{a})$

$$\mathcal{F}(\gamma\widetilde{E}) \;=\; -\frac{\gamma\widetilde{E}}{2\pi}\Theta(-\widetilde{E}) + \frac{\widetilde{a}}{4\pi^2\gamma v^3}\int_0^\infty \mathrm{d}z\, \cos\left(2\frac{\widetilde{E}}{\widetilde{a}}vz\right)\left(\frac{\gamma^2v^2}{z^2} - \frac{1}{\frac{z^2}{v^2}-\sin^2 z}\right) . \tag{2.105}$$

The results for the analogue, circular Unruh temperature in relation to the linear acceleration Unruh temperature can be found in figure 2.5. As in the relativistic case, the ratio of circular to linear Unruh temperature converges to the value $\pi/(2\sqrt{3})$ for $v \to 1$ with $\widetilde{T}_{\mathrm{circ}} \sim \gamma\widetilde{a}$ as can be seen from the limit of equation (2.105). Note that taking this limit does not cause any issues as equation (2.105) is uniform in E/a.

2 + 1 Dimensions. In $2+1$ dimensions we evaluate equation (2.79) at $\gamma\widetilde{E}$

$$\mathcal{F}(\gamma\widetilde{E}) \;=\; \frac{1}{2}\Theta(-\widetilde{E}) + \frac{1}{2\pi\gamma v}\int_0^\infty \mathrm{d}z\, \sin\left(2\frac{\widetilde{E}}{\widetilde{a}}vz\right)\left(\frac{\gamma v}{z} - \frac{1}{\sqrt{\frac{z^2}{v^2}-\sin^2 z}}\right) . \tag{2.106}$$

In particular, we are interested in the $(2+1)$, ultra-relativistic case with $v \to 1$. For this reason, it is useful to look at the split in even and odd parts of the response function (2.78). For large v one can construct a dominated convergence argument to show that [54]

$$\mathcal{F}(\gamma\widetilde{E}) \;\to\; \frac{1}{4} - \frac{\sqrt{3}}{\pi}\frac{\ln\gamma}{\gamma}\frac{\widetilde{E}}{\widetilde{a}} , \tag{2.107}$$

where only the leading contribution of γ is kept and using $R = v^2/a \to 1/a$ for $\gamma \to \infty$.

Using detailed balance, the circular temperature in this limit is

$$\widetilde{T}_{\mathrm{circ}}^{(2+1)} \;\approx\; \frac{\pi}{8\sqrt{3}}\frac{\gamma}{\ln\gamma}\widetilde{a} , \tag{2.108}$$

where we have used $\ln\gamma/\gamma \to 0$ for $\gamma \to \infty$ to use the lowest order Taylor expansion for the logarithm.

We see from figure 2.5 that the behaviour of the ratio of circular to linear Unruh temperature is similar to the one in the relativistic case. In $3+1$ dimensions we see that the ratio converges to a constant value for $v \to 1$ which means that the circular Unruh temperature grows proportional to γ as does the linear Unruh temperature. In $2+1$ dimensions, however, we see that in ratio drops to zero in the ultra-relativistic limit. Equation (2.108) shows that the circular Unruh temperature grows in that limit as well, but is suppressed by the factor $1/\ln\gamma$. It therefore grows slower than the linear Unruh temperature.

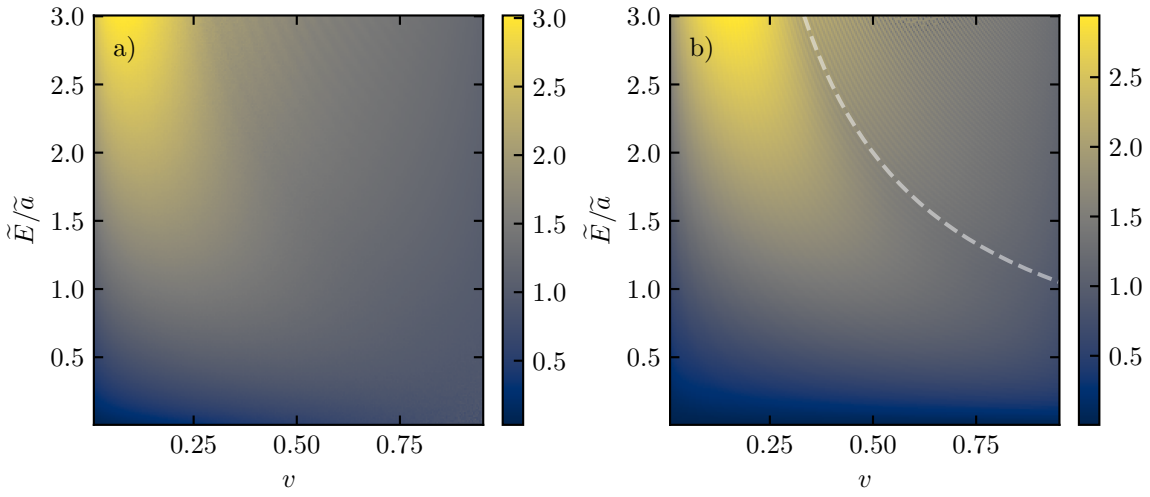

Figure 2.5 (Analogue Unruh Temperature) Ratio of analogue temperature to linear temperature in a) $3+1$ dimensions as given by the response function in equation (2.105) and b) in $2+1$ dimensions as given by the response function in equation (2.106). White, dashed line indicates local minimum at $\widetilde{E}/\widetilde{a} = 1/v$.

Figure 2.5 shows as well that there is a local minimum in $2+1$ dimensions where $\widetilde{E}/\widetilde{a} = 1/v$, indicated by the white dashed line. This is a peculiar phenomenon as it suggests that for a given v there exists an energy range in which the Unruh temperature decreases, reaches a minimum and then increases again. This effect seems to be genuine and not an artefact of the numerical methods in this chapter, however, the exact reason for its appearance is not yet fully understood and requires further research.

2.6 Summary

In the first part of this chapter, we introduced the Unruh effect of a linearly accelerated observer as originally described by Fulling, Davies and Unruh while defining some fundamental concepts of quantum field theory that will be used later on. The main part of this chapter described how the Unruh effect can be obtained from a circular accelerated trajectory. We have shown a detailed calculation of the response functions for a massless scalar quantum field in its Minkowski vacuum state on a circular trajectory in 3+1 and 2+1 dimensions and compared the results to the expression obtained from the linear acceleration formula. The full range of this ratio has been outlined numerically, however certain limits can be obtained analytically. As expected, the Unruh temperature was highest in the ultra-relativistic limit for $v \to 1$, both in $2+1$ and $3+1$ dimensions.

In a novel approach to the discussion of particle and Unruh-DeWitt detectors we have extended the meaning of a detector from a two-level system to a continuous field detector. Conceptually, the continuous detector has the same trajectory dependence as an Unruh-DeWitt detector.

Finally, we used the results for the circular accelerated trajectory to calculate the corresponding response functions in analogue systems. The most important difference between those systems is that we had to scale relevant quantities such as the energy, temperature and acceleration by the time dilation gamma-factor. However, we found a logarithmic suppression factor in the limit $v \to c_s$ of the circular Unruh temperature in $2+1$ dimensions, which could help stay longer in the regime of linear perturbation theory.

As motivated by previous proposals to observe the circular motion Unruh effect in condensed matter analogue spacetime systems [46, 55], we will use these results in later chapters. All the results have been obtained for a sufficiently small coupling constant, which allows for a first-order perturbation theory treatment, and we used the simplifying assumptions in the derivation of the Unruh effect for a spatially infinite system whose initial state as well as the initial detector state are prepared in the vacuum state. These are rather idealised conditions and calculations will get more complicated once we restrict the system to a finite size [74, 75, 76]. Physically, we assumed that the dimensions of the analogue system are large compared to the detector orbit, effectively neglecting those finite size effects. In addition to finite size effects, we find that accelerating a detector which has a finite initial temperature will pick up a signal due to a Doppler shift and due to the Unruh temperature. In this case, more study is needed to isolate the Unruh effect part of the signal [77, 78]. In addition, all the calculations presented in this chapter neglect back-action of the detector on the field [79, 80, 81] and finite interaction time effects due to switching the coupling on and off [82].

A Note on Symmetry. The detailed balance condition in equation (2.39) connects the Unruh temperature to the ratio of excitation and de-excitation rates, or the ratio of the response function of negative and positive energies. Any response function that is entirely symmetric in E does not give rise to a temperature as the logarithm of this ratio equals zero. For a general split in even and odd parts we have

$$\frac{\mathcal{F}(-E)}{\mathcal{F}(E)} = \frac{\mathcal{F}^{\text{even}}(E) - \mathcal{F}^{\text{odd}}(E)}{\mathcal{F}^{\text{even}}(E) + \mathcal{F}^{\text{odd}}(E)} \,. \tag{2.109}$$

Note that any response function, which is entirely even in E will not give rise to a temperature via the detailed balance condition. Interestingly, this chapter showed that the information contained in the even and odd part depends on the dimensions considered. Equation (2.59) tells us that in three dimensions the even part is the one that contains all the information about the trajectory. On the other hand, it is the odd part in two dimensions that depends on the parameters of the trajectory.

III

Analogue Unruh Effect

And it blows my mind
Yeah, it blows my mind
—Corey Taylor

Analogues have always played a big role in physics by developing and studying a mathematical model in a particular physical system (source) and applying the newly gained knowledge thereof to a different system (target), which is described by the same model. In Unruh's words: the mathematical model acts just like a map which can be applied to two different territories [23]. These analogues help use intuition and existing solutions in this source system to develop possible solutions and ideas in the target system. A particularly useful, and perhaps surprising at first, analogy is the analogy between gravitational effects and fluid mechanics [25, 83, 84, 85]. In general, analogues have the tremendous advantage to study phenomena in relativistic quantum field theory in well controlled setups [30, 73]. This led to experimental observations of fundamental effects of quantum field theories in curved spacetime, such as superradiant scattering of rotating black holes [43] and the Hawking effect in classical [86, 87, 88] and quantum systems [89, 90].

In all cases of those analogues, perturbations in the system ϕ can be described by a minimally coupled Klein-Gordon field in effective geometries, whose dynamics is described by

$$\frac{1}{\sqrt{-g}}\partial_\mu\left(\sqrt{-g}g^{\mu\nu}\partial_\nu\phi(t,\boldsymbol{x})\right) \;=\; 0\,. \tag{3.1}$$

This Klein-Gordon equation with metric g usually emerges when the system in its generality is simplified. For example, in the context of wave propagations in fluids, this metric is often found

to be

$$g_{\mu\nu} \sim \begin{pmatrix} -(c_s^2 - v^2) & -v^T \\ -v & \mathbb{I}_{n\times n} \end{pmatrix}, \tag{3.2}$$

where c_s is the propagation speed of waves in the medium and v the n-dimensional background fluid flow velocity. The simplest case with $v = 0$ and constant c_s shows that this metric has the form of a Minkowski metric, however, the speed of light is replaced by the speed of sound in this particular system.

The Unruh effect strikes with its simplicity in derivation, but remains one of the most counter-intuitive phenomena in QFT. Even more difficult is its observation: a temperature of 1 Kelvin requires an acceleration of $\sim 2.5 \times 10^{20}$ m/s^2. A huge acceleration with a tiny effect only is having us waiting for an experimental verification of its existence. However, using the idea of analogues in which the speed of light is replaced by the speed of sound in this medium, thus reducing the required acceleration, the measurement of this effect seems to be in reach. Studying this effect will lead to new insights in the ever so confusing world of quantum mechanics and will foster a better understanding of the Unruh effect. But first, we need to find appropriate systems which exhibit this mapping to the relativistic detector model (2.92).

As we have seen in the previous chapter, a continuous field can be used as an Unruh detector, which arise naturally in many physical systems. In this chapter we provide the modelling of the field theory described by equation (2.92) in a physical context. It turns out, that low temperature systems interacting with a laser beam are particularly well suited as a model.

First, we derive the fundamental form of light-matter interactions and then show the equivalence of a Bose-Einstein Condensate (BEC) and superfluid Helium-4 interacting with a laser to the relativistic theory. In addition, we noticed that the continuous detector model consists of a $(1 + 1)$ and a $(2 + 1)$-dimensional massless scalar field. In all generality, physical systems are $(3 + 1)$-dimensional theories, however, we can choose the set of parameters in such a way that we can effectively describe the probing field as a $(1 + 1)$-dimensional scalar field and the field being probed as $(2 + 1)$-dimensional.

3.1 Electromagnetic Fields

A central element of the systems described in this chapter is the interaction of matter with an external electromagnetic field. We will see how (quantum) phase fluctuations of the electromagnetic field on a classical background can be used as a continuous detector field. In the following, we will outline the approximations that are necessary to linearise the electromagnetic field in terms of those phase fluctuations.

3.1.1 Dynamic Equations

We start off with the Lagrangian for the electromagnetic field [91] [1]

$$\mathcal{L}_{\mathrm{em}} \;=\; -\frac{1}{4\mu_0} F_{\mu\nu}F^{\mu\nu}\,, \tag{3.3}$$

with $F^{\mu\nu} = \partial^\mu A^\nu - \partial^\nu A^\mu$, A^μ being the electromagnetic 4-potential. This Lagrangian has some degrees of freedom that can be fixed by working in Coulomb gauge, with $A_0 = 0$ and $\nabla \cdot \boldsymbol{A} = 0$. This gauge reduces the Lagrangian of the electromagnetic field to the sum of the Lagrangian for two scalar fields, each representing one polarisation of the electromagnetic field. Working with only one of those polarisations propagating in z direction reduces this Lagrangian to

$$\mathcal{L}_{\mathrm{em}} \;=\; -\frac{1}{2\mu_0}\left(\frac{1}{c_0^2}\left(\partial_t A(t,z)\right)^2 - \left(\partial_z A(t,z)\right)^2\right)\,. \tag{3.4}$$

In a slight abuse of notation, A does not refer to the whole electromagnetic potential any more but only to this chosen polarisation. The equation of motion for $A(t,z)$ is derived by variation of the corresponding action, leading to

$$\frac{1}{c_0^2}\partial_t^2 A(t,z) - \partial_z^2 A(t,z) \;=\; 0\,, \tag{3.5}$$

which is essentially the equation of motion for a real scalar field, propagating with the speed of light in vacuum c_0.[2] Upon quantisation we promote the electromagnetic potential to an operator and introduce commutation relations. We can write the quantised, $(1+1)$-dimensional electromagnetic potential as a mode expansion given as in (2.10), with the electromagnetic field given by $\hat{E}(t,z) = \partial_t \hat{A}(t,z)$. Calculating the derivative of the mode expansion for $\hat{A}(t,z)$ explicitly, we see that the mode representation of $\hat{E}(t,z)$ is

$$\hat{E}(t,z) \;=\; \int \mathrm{d}\omega\; E_\omega \mathrm{i}\left(\hat{a}_\omega \mathrm{e}^{-\mathrm{i}(\omega t - kz)} - \hat{a}_\omega^\dagger \mathrm{e}^{\mathrm{i}(\omega t - kz)}\right)\,, \tag{3.6}$$

with

$$E_\omega \;=\; \sqrt{\frac{\hbar\omega}{4\pi\epsilon_0 c_0 A_\perp}}\,. \tag{3.7}$$

$A_\perp$ is the area through which the photon flux, as given by the operator $\hat{a}_\omega^\dagger \hat{a}_\omega$, propagates.

[1] μ_0 is the vacuum permeability with $\mu_0 = 1.25663706212(19) \times 10^{-6}$ kg m s^{-2} A^{-2}.
[2] The speed of light is given by $c_0 = 299792458$ m/s

For a macroscopically occupied single-frequency field with mode frequency ω_L the corresponding operator becomes a c-number $\hat{a}_{\omega_L} = \alpha \in \mathbb{C}$ The electromagnetic potential can then be conveniently written as

$$A(t,z) \;=\; A_0 \cos\left(\omega_L t - kz\right) \;. \tag{3.8}$$

Later, we will use this ansatz for a laser beam, thus, already introducing the subscript L for the carrier frequency of the laser.

The electromagnetic field, however, never contains just a single frequency, but always has a certain bandwidth. Even with a macroscopically occupied mode at a certain frequency there exist fluctuations around that frequency. The electromagnetic potential with phase fluctuations about this background can be written as

$$A(t,z) \;=\; A_0 \cos\left(\omega_L t - kz + \psi(t,z)\right) \;, \tag{3.9}$$

with $\psi(t,z)$ being phase fluctuations that could either be classical or quantum. As we will see later, we are interested in a measurement that is sensitive to the phase of the electromagnetic field only. We will therefore focus on phase fluctuations only and omit amplitude fluctuations. In addition, these phase fluctuations are assumed to be small such that the lowest order in ψ are the predominant contributions. We use this ansatz in equation (3.4) to obtain an effective Lagrangian for $\psi(t,z)$. Omitting the constant background term, the result is

$$\mathcal{L}_{\text{em}} \;=\; \frac{1}{2\mu_0}\left(\frac{1}{c_0^2}\left(\partial_t\psi(t,z)\right)^2 - \left(\partial_z\psi(t,z)\right)^2\right) \;, \tag{3.10}$$

where we rescaled the original field ψ by the constant factor $A_0/\sqrt{2}$ to obtain the standard form of the massless scalar field Lagrangian. In anticipation of implementing this formalism in specific systems, we assume at this point that the laser frequency is much higher than any frequency at which those systems will be probed. Effectively, we can time average over a period $2\pi/\omega_L$ such that any sine and cosine vanishes and squared sine and cosine results in a factor of $1/2$.[3]

This shows that phase fluctuations about a constant background of an electromagnetic field can be effectively treated as a $(1+1)$-dimensional, massless Klein-Gordon field. This is the first stepping stone towards the analogue models discussed in this chapter. The phase fluctuations in this field will take the role of a continuous detector. For an analogy to the model described in section 2.4, this detector has to couple to a scalar field in a particular way. More specifically, it has to couple with a time derivative to another massless Klein-Gordon field. Looking into continuous detectors was motivated by the goal to model these physical detectors. But all the mathematical curiosity aside, it is not sufficient to simply construct such a model by hand, but it has to be derived based on physical processes. Originally, the motivation behind the development of a continuous detector model was the desire to model exactly the systems in this chapter. In the following section, we will see how an interaction between light and polarisable matter gives rise to the desired coupling.

3.1.2 Interaction with Matter

When we talk about a dielectric medium interacting with light we refer to the property of this medium to react to the electromagnetic field by developing dipoles. The amplitude of the

[3] Using $\left(\partial_t A\right)^2 = \frac{1}{2}A_0^2\left(\omega + \partial_t\psi\right)^2$ and $\left(\partial_z A\right)^2 = \frac{1}{2}A_0^2\left(-k + \partial_z\psi\right)^2$.

induced dipole moment $\boldsymbol{d}$ for an external electromagnetic field $\boldsymbol{E}$ is given by [92]

$$\langle \boldsymbol{d} \rangle \;=\; \alpha(\omega)\,\langle \boldsymbol{E} \rangle \;. \tag{3.11}$$

In this section, $\langle \ldots \rangle$ is a time-average. This kind of interaction is called electrostriction and is quantified by the medium specific polarisability α. The polarisability of an isotropic medium is a complex number and depends on the frequency of the external field. The interaction potential of the induced dipole and the external field is given by [92]

$$V \;=\; -\frac{1}{2}\boldsymbol{d}\cdot\boldsymbol{E}\;. \tag{3.12}$$

Note that the time averaged intensity per area is given by

$$I \;=\; \frac{1}{2}\epsilon_0 c|E_0|^2\;. \tag{3.13}$$

However, if we wanted to compute the absorbed power $P_{\mathrm{ab}} = \langle \dot{\boldsymbol{d}}\cdot\boldsymbol{E}\rangle$, we would see that the imaginary part of the polarisability is responsible for the absorption of the medium which we can easily calculate to be $P_{\mathrm{ab}} = 2\omega \mathrm{Im}\left(\alpha(\omega)\right)|E_0|^2$. Thinking of scattering as the process of absorption and subsequent re-emission of photons, we can define the scattering rate Γ_{sc} as

$$\Gamma_{\mathrm{sc}} \;=\; \frac{P_{\mathrm{ab}}}{\hbar\omega} \;=\; \frac{2}{\hbar}\mathrm{Im}\left(\alpha(\omega)\right)|E_0|^2 \;=\; \frac{4}{\hbar\epsilon_0 c_0}\mathrm{Im}\left(\alpha(\omega)\right) I\;. \tag{3.14}$$

We have now specified how the medium reacts to an external electromagnetic field, however, we still need to compute the polarisability. Here, we want to use a classical approach by approximating the atom as an oscillator which is driven by an external field. The result for α can be found in standard literature [91], such that

$$\alpha \;=\; 6\pi\epsilon_0 c^3 \frac{\Gamma/\omega_r^2}{\omega_r^2-\omega^2-\mathrm{i}\frac{\omega^3}{\omega_r^2}\Gamma}\;, \tag{3.15}$$

where Γ is the classical on-resonance damping rate of the oscillator given by

$$\Gamma \;=\; \frac{e^2\omega_r^2}{6\pi\epsilon_0 m_e c^3}\;. \tag{3.16}$$

Here, ω_r is the resonant frequency of the oscillator, ω the frequency of the external field, e the electron charge and m_e the electron mass. Alternatively, α can be calculated using a quantum mechanical model of an atom with two distinct energy levels and a classical external field, however, at far detuned frequencies and low scattering rates $\Gamma_{\mathrm{sc}} \ll \Gamma$, the corresponding solution is well approximated by the one of the entirely classical ansatz in equation (3.15) [92, 93]. In this case, equation (3.15) simplifies to

$$\alpha \;=\; \frac{3\pi\epsilon_0 c^3}{\omega_r^3}\left(\frac{\Gamma}{\omega_r-\omega}+\frac{\Gamma}{\omega_r+\omega}\right)+\mathrm{i}\frac{3}{2}\frac{\pi\epsilon_0 c^3}{\omega_r^3}\left(\frac{\Gamma^2}{(\omega_r-\omega)^2}-\frac{\Gamma^2}{(\omega_r+\omega)^2}\right)\;. \tag{3.17}$$

This expression has the usual resonant term at $\omega=\omega_r$ as well as a counter-rotating term which is resonant at $\omega=-\omega_r$. If we assume that $|\omega-\omega_r| \ll \omega_r$, then the counter-rotating term can

be neglected, which is called the rotating wave approximation [94]. In this case, we find

$$\alpha \;=\; \frac{6\pi\epsilon_0 c^3}{\omega_r^3}\left(\frac{1}{\delta_0}+\mathrm{i}\frac{1}{\delta_0^2}\right)\,, \tag{3.18}$$

defining the detuning per half-line width $\delta_0 = (\omega-\omega_r)/(\Gamma/2)$. For $\delta_0 < 0$ we talk about red detuning and for $\delta_0 > 0$ about blue detuning.

For large detunings, the real part of α in equation (3.18) is dominating. In this case, it is convenient to express the laser frequency as a detuning from the resonant frequency by a modulation frequency $\pm\omega_m$ such that $\omega = \omega_r \pm \omega_m$. Then, the polarisability for detunings in both directions from the resonant frequency is given by

$$\alpha(\omega_r \pm \omega_m) \;=\; \mp\frac{3\pi\epsilon_0 c^3}{\omega_r^3}\frac{\Gamma}{\omega_m}\,, \tag{3.19}$$

from which we see that $\alpha(\omega_r+\omega_m) = -\alpha(\omega_r-\omega_m)$.

Now, we have an explicit form for the atomic polarisability derived from the induced dipole interactions, but what happens in the context of field theories interacting with an external field? Every atom in this approximation develops a dipole and consequently the external field applies a force $\boldsymbol{f}$ on the medium. This force can be calculated to [91, 95]

$$f_i \;=\; \frac{1}{2}\partial_i\left(\boldsymbol{E}^2\rho\frac{\partial\epsilon}{\partial\rho}\right)\,, \tag{3.20}$$

assuming that the permittivity depends on space coordinates only implicitly through its density $\epsilon(\boldsymbol{x},\rho) = \epsilon(\rho)$. How exactly the permittivity depends on the number density ρ is given by the Clausius-Mossotti relation [96][4]

$$\epsilon(\boldsymbol{x})-\epsilon_0 \;=\; \frac{\rho(\boldsymbol{x})\alpha}{1-\frac{\rho(\boldsymbol{x})\alpha}{3\epsilon_0}}\,. \tag{3.21}$$

Most of the time we find that $\rho\alpha \ll 3\epsilon_0$, justifying the approximation

$$\epsilon(\boldsymbol{x}) \;\approx\; \epsilon_0+\rho(\boldsymbol{x})\alpha\,. \tag{3.22}$$

The force in equation (3.20) can be expressed as the gradient of a potential $\boldsymbol{f} = -\nabla\phi$ using equation (3.22) and $\boldsymbol{E} = \partial_t\boldsymbol{A}$

$$\phi \;=\; -\frac{\rho\alpha}{2}\left(\partial_t\boldsymbol{A}\right)^2\,. \tag{3.23}$$

It is exactly the potential in equation (3.23) that describes the interaction between an electromagnetic field and matter, represented by the density ρ. Working on the level of Lagrangians we have

$$\mathcal{L}_{\text{int}} \;=\; -\frac{\rho\alpha}{2}\left(\partial_t\boldsymbol{A}\right)^2\,. \tag{3.24}$$

The electromagnetic field couples to the matter specific density which, we will see later, will be the second dynamic scalar field in our analogue model. The polarisability takes the role of a coupling constant. For now, we want to see how this interaction affects the dynamics of the electromagnetic field. The whole electromagnetic Lagrangian, including the interaction with

[4]The vacuum permittivity is given by $\epsilon_0 = 8.8541878128(13)\times10^{-12}\ \mathrm{Fm}^{-1}$.

matter, can be rearranged to

$$\mathcal{L} \;=\; -\frac{1}{2\mu_0}\left(\frac{1}{c_0^2}\left(1+\rho\alpha\mu_0 c_0^2\right)\left(\partial_t A(t,z)\right)^2-\left(\partial_z A(t,z)\right)^2\right)\,. \tag{3.25}$$

Note that strictly speaking the interaction is confined to the medium, so unless the medium does not extend infinitely, there has to be some sort of switching function which we will omit for brevity and only reintroduce it where necessary. The expression above shows that within the medium the effective speed of light is given by

$$\frac{1}{c^2} \;=\; \frac{1}{c_0^2}\left(1+\rho\alpha\mu_0 c_0^2\right)\,, \tag{3.26}$$

which allows us to define the index of refraction for this medium [5]

$$n^2 \;=\; \frac{c_0^2}{c^2} \;=\; 1+\frac{\rho\alpha}{\epsilon_0}\,. \tag{3.27}$$

This result is what we would naively expect - the denser the medium, and the stronger the coupling, the higher the effect on the electromagnetic field.

In the same fashion as before, we can use the electromagnetic field ansatz for quantum fluctuations on a classical background in equation (3.9), as well as the simplifying calculations, such as the averaging over fast oscillating frequencies, to arrive at the interaction Lagrangian

$$\mathcal{L}_{\text{int}} \;=\; -\frac{\alpha\rho}{2}\left(\frac{A_0\omega}{\sqrt{2}}+\partial_t\psi(t,z)\right)^2\,, \tag{3.28}$$

applying the same rescaling as before. The construction of a physical interaction between matter and light has led us to this interaction which couples the density ρ and the linearised phase fluctuations ψ of the electromagnetic field. In this sense, we have found the first two parts of the analogue, the $(1+1)$-dimensional probing field ψ and its interaction with some yet to determined matter field. In the next section, we will see what this field is and how it completes the analogue.

[5] Using the identity $\epsilon_0 = \left(\mu_0 c_0^2\right)^{-1}$

3.2 Analogue Unruh Effect in Bose-Einstein Condensates

In 2001 the Nobel Prize in physics was awarded to Eric A. Cornell, Wolfgang Ketterle and Carl E. Wieman "for the achievement of Bose-Einstein condensation in dilute gases of alkali atoms, and for early fundamental studies of the properties of the condensates". It was a recognition of an almost centuries-long endeavour after Satyendra Nath Bose and Albert Einstein postulated a new possible state of particles already in 1924 [97]. However, it was not before the 1990s that the first Bose-Einstein Condensate (BEC) was created in a laboratory. Breakthroughs in technology and cooling techniques made it possible to reach nano Kelvin temperatures, which was the starting point of the ever since growing field of experimental BEC research [98]. In theory, creating BECs is fairly simple: take a low density gas of bosonic atoms and cool it down below a critical temperature. Once the spatial extent of each atom's wave function becomes larger than the interatomic separation of atoms, those wave functions start to overlap and the gas starts to enter a state of indistinguishable particles. As the temperature approaches zero, the result is a macroscopical entity of a single, quantum mechanical state of bosons occupying the lowest energy state. As E. Cornell so aptly described it "Quantum mechanics rules over the physics in two regimes: the very cold, and the very small. Insights derived from one regime can apply in the other". This new ultra-cold state thus allows us to probe quantum phenomena at a macroscopic scale.

Of course the lack of trapping and cooling techniques didn't keep theorists from investigating this intriguing phenomenon. Most important for this thesis was the work of Eugene P. Gross and Lev Petrovich Pitaevskii who derived an equation that describes the evolution of the macroscopic wave function. Their starting point was a gas of bosonic atoms for which the inter-particle distance is much larger than the scattering length. In a similar way that a field with a high occupation number of photons in the same state can be described by classical Maxwell equations, the field for this macroscopic wave function $\Phi(t, \boldsymbol{x})$ of the BEC in an external potential $U(\boldsymbol{x})$ can be shown to have the action

$$S = \int \mathrm{d}t\mathrm{d}\boldsymbol{x}\ \Phi^*(t,\boldsymbol{x}) \left[\mathrm{i}\hbar\frac{\partial}{\partial t} + \frac{\hbar^2}{2m}\nabla^2 - U(\boldsymbol{x}) - \frac{1}{2}g|\Phi(t,\boldsymbol{x})|^2 \right] \Phi(t,\boldsymbol{x}) \ , \tag{3.29}$$

with m being the BEC atom mass, and g the coupling constant. Variation of this action leads to what is now known as the Gross-Pitaevskii equation (GPE)

$$\mathrm{i}\hbar\frac{\partial}{\partial t}\Phi(t,\boldsymbol{x}) = \left[-\frac{\hbar^2}{2m}\nabla^2 + U(\boldsymbol{x}) + g|\Phi(t,\boldsymbol{x})|^2 \right] \Phi(t,\boldsymbol{x}) \ , \tag{3.30}$$

with

$$g = \frac{4\pi\hbar^2 a_s}{m} \ , \tag{3.31}$$

being the interaction coupling constant related to the s-wave scattering length a_s.

Having a macroscopical system with quantum mechanical properties provides a fascinating framework for analogue experiments. In this chapter, we will see how BECs can be used in a setup to probe the Unruh effect. We will first establish the regime in which the analogy to the relativistic quantum field theory holds and show how the interaction with lasers completes the model.

3.2.1 Bogoliubov Theory

In an attempt to describe the excitation spectrum of BECs, N. Bogoliubov published a paper in 1946 on what later will be know as the Bogoliubov theory for BECs [99]. Bogoliubov simplified this many-body problem with a two-body potential V that enters the Hamiltonian as $\hat{\psi}^\dagger(r)\hat{\psi}^\dagger(r')V(r-r')\hat{\psi}(r')\hat{\psi}(r)$. As v has a divergent short range behaviour, the first step in this simplification was to apropriately smoothen this potential and replace it with an effective potential that accurately desribes the macroscopic behaviour of the BEC and to which perturbation theory can be safely applied. Quantisation of $\hat{\psi}$ with annihilation operators $\hat{a}_{\boldsymbol{p}}$ creates a Hamiltonian to various orders in $\hat{a}_{\boldsymbol{p}}$ [100]. Namely, the potential term is proportional to $\hat{a}^\dagger_{\boldsymbol{p}_1}\hat{a}^\dagger_{\boldsymbol{p}_2}\hat{a}_{\boldsymbol{p}_3}\hat{a}_{\boldsymbol{p}_4}$. Then, Bogoliubov theory only replaces the annihilation operator corresponding to the momentum $\boldsymbol{p}=0$ with a c-number, $\hat{a}_0 \to a_0 \in \mathbb{C}$. In order for this theory to give rise to an excitation spectrum, only lowest order combinations in the remaining operators with $\boldsymbol{p} \neq 0$ are considered. The resulting Hamiltonian can be diagonalised with a linear transformation on operators, which is known as Bogoliubov transformation that expresses a set of new operators $\hat{b}_{\boldsymbol{p}}$ as a linear combination of $\hat{a}_{\boldsymbol{p}}$ and $\hat{a}^\dagger_{\boldsymbol{p}}$. After this transformation, the Hamiltonian is diagonal in terms of the new operators $\hat{b}_{\boldsymbol{p}}$, such that

$$\hat{H} \;=\; \sum_{\boldsymbol{p}} \epsilon(\boldsymbol{p})\hat{b}^\dagger_{\boldsymbol{p}}\hat{b}_{\boldsymbol{p}}\,, \tag{3.32}$$

omitting the constant ground state energy. The Bogoliubov theory dispersion relation for elementary excitations

$$\epsilon(\boldsymbol{p}) \;=\; \left(\frac{gn}{m}p^2 + \left(\frac{p^2}{2m}\right)^2\right)^{1/2}\,, \tag{3.33}$$

is shown in figure (3.1), where n is the number density of the BEC. This spectrum describes the energy of excitations associated with the operators $\hat{b}_{\boldsymbol{p}}$ which are quasi-particle excitations. For small momenta with $p \ll mc$ the dispersion relation takes a phonon-like form, which is linear in momenta p

$$\epsilon(\boldsymbol{p}) \;=\; cp\,, \tag{3.34}$$

where $c = \sqrt{gn/m}$ is the speed of sound in the BEC. The transition from the phononic to the free particle regime occurs at momenta with $p^2/2m \sim gn$ corresponding to a characteristic length $\xi = \hbar/p$ called the healing length

$$\xi \;=\; \sqrt{\frac{\hbar}{2mgn}}\,. \tag{3.35}$$

The average occupation number of particles with momentum $\boldsymbol{p}$ can be calculated with the help of the Bogoliubov transformation

$$N_{\boldsymbol{p}} \;=\; \langle \hat{b}^\dagger_{\boldsymbol{p}}\hat{b}_{\boldsymbol{p}}\rangle \;=\; \frac{1}{\mathrm{e}^{\beta\epsilon(\boldsymbol{p})}-1}\,. \tag{3.36}$$

This is the famous Bose-Einstein distribution that describes the distribution of particles with a given energy of a state at temperature $k_{\mathrm{B}}T = 1/\beta$. Having established the basic framework for BECs, we now want to apply a few assumptions for our system in order to prepare for the desired analogy.

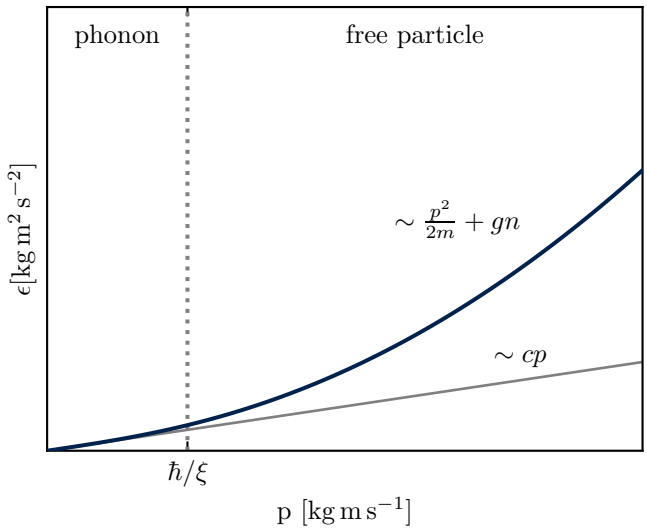

Figure 3.1 (Bogoliubov spectrum) Energy spectrum for full dispersion relation (blue) and phononic regime for $p \ll \sqrt{2mgn}$ (grey). Transition from phononic to free particle regime takes place at $p \sim \frac{\hbar}{\xi}$.

3.2.2 Density Fluctuations of Two-Dimensional BECs

Earlier we introduced the GPE for a three-dimensional BEC, however, a harmonic trapping potential in one direction, say z-direction, can be applied to create an effective (2+1)-dimensional BEC. The trapping potential $U(\boldsymbol{x}) = W(x,y) + \frac{1}{2}m\omega_z^2 z^2$ can be used to effectively freeze the dynamics in that direction by tuning ω_z appropriately. The result is an oblate shaped BEC. We can separate the wave function as follows [101]

$$\Phi(t,\boldsymbol{x}) \;=\; \phi(t,x,y) f(t,z;\eta(t,x,y)) \;, \tag{3.37}$$

with

$$f(t,z;\eta(t,x,y)) \;=\; \frac{\mathrm{e}^{-z^2/2\eta(t,x,y)^2}}{\pi^{1/4}\eta(t,x,y)^{1/2}} \;. \tag{3.38}$$

$\eta(t,x,y)$ describes the width of the condensate in the z-direction. In addition, we assume that f is slowly varying in (x,y), such that $\nabla_\perp^2 f \approx 0$. Substituting this in the three-dimensional action leads to the following equations of motion for ϕ and η

$$\mathrm{i}\hbar\partial_t\phi(t,x,y) \;=\; \left[-\frac{\hbar^2}{2m}\nabla_\perp^2 + W + g\frac{\eta^{-1}}{(2\pi)^{1/2}}|\phi(t,x,y)|^2 + \left(\frac{\hbar^2}{2m}\eta^{-2} + \frac{m\omega_z^2}{2}\eta^2\right)\right]\phi(t,x,y) \tag{3.39a}$$

$$0 \;=\; \frac{\hbar^2}{2m}\eta^{-3} - \frac{1}{2}m\omega_z^2\eta + g\frac{\eta^{-2}}{2(2\pi)^{1/2}}|\phi|^2 \;. \tag{3.39b}$$

In the weakly interacting case $a_s|f|^2 \ll 1$ we have $\eta = a_z = \sqrt{\frac{\hbar}{m\omega_z}}$, such that the equation of motion is

$$\mathrm{i}\hbar\partial_t\phi(t,x,y) \;=\; \left[-\frac{\hbar^2}{2m}\nabla_\perp^2 + W(x,y) + \frac{g}{(2\pi)^{1/2}a_z}|\phi(t,x,y)|^2\right]\phi(t,x,y)\;. \tag{3.40}$$

Comparing this equation to the three-dimensional GPE in equation (3.30), this equation has the very same form with an effective two-dimensional coupling $g_{2d} = \frac{g}{(2\pi)^{1/2}a_z}$. Having seen that the effectively two-dimensional BEC obeys the GPE as well, we continue by linearising this equation in terms of small density and phase fluctuations.

Linearisation. The Gross-Pitaevskii field can be parametrised in terms of a density and phase function which is called Madelung representation $\phi(t,\boldsymbol{x}) = \sqrt{\rho(t,\boldsymbol{x})}\mathrm{e}^{\mathrm{i}S(t,\boldsymbol{x})}$. The number density of the BEC is then associated with the square modulus of this field $\rho(t,\boldsymbol{x}) = |\phi(t,\boldsymbol{x})|^2$. Now, consider fluctuations of the density about some constant background ρ_0 such that $\rho(t,\boldsymbol{x}) = \rho_0 + \delta\rho(t,\boldsymbol{x})$ and fluctuations of the phase $S(t,\boldsymbol{x}) = S_0 + \delta S(t,\boldsymbol{x})$. The constant solution $\Phi_0 = \sqrt{\rho_0}\mathrm{e}^{\mathrm{i}S_0}$ obeys the GPE as well which means that

$$W(x,y) + g_{2d}\rho_0 \;=\; 0\;. \tag{3.41}$$

For brevity, we will omit any reference to 2d in the notation that follows. The set of linearised equations emerging from separating the GPE into real and imaginary part is

$$\partial_t\delta\rho(t,\boldsymbol{x}) \;=\; -\frac{\hbar}{m}\rho_0\nabla^2\delta S(t,\boldsymbol{x})\;, \tag{3.42a}$$

$$\hbar\partial_t\delta S(t,\boldsymbol{x}) \;=\; \frac{\hbar^2}{4m\rho_0}\nabla^2\delta\rho(t,\boldsymbol{x}) - g\delta\rho(t,\boldsymbol{x})\;, \tag{3.42b}$$

where we have used that $\delta\rho \ll \rho_0$ and where we have only kept terms up to linear order in any perturbation. These two equations can be combined into an equation of motion for $\delta\rho(t,\boldsymbol{x})$ by taking the time derivative of equation (3.42a) and substitute in the expression for $\partial_t S(t,\boldsymbol{x})$ of equation (3.42b)

$$\partial_t^2\delta\rho(t,\boldsymbol{x}) \;=\; -\frac{\hbar^2}{4m^2}\nabla^4\delta\rho(t,\boldsymbol{x}) + \frac{\rho_0 g}{m}\nabla^2\delta\rho(t,\boldsymbol{x})\;. \tag{3.43}$$

From this equation, the dispersion relation for $\delta\rho(t,\boldsymbol{x})$ is given by

$$\epsilon^2(k) \;=\; (\hbar\omega_k)^2 \;=\; \frac{\hbar^2k^2}{2m}\left(\frac{\hbar^2k^2}{2m} + 2\mu\right)\;, \tag{3.44}$$

with $\mu = \rho_0 g$ being the chemical potential. This is the same expression as the Bogoliubov excitation spectrum introduced earlier. If $\frac{\hbar^2k^2}{2m} \ll 2\mu$, then the energy is given by

$$\epsilon(k) \;=\; \sqrt{\frac{\mu\hbar^2}{m}}k\;, \tag{3.45}$$

indicating the linear part of the dispersion relation. In this regime the density fluctuations obey the wave equation

$$\partial_t^2 \delta\rho(t,\boldsymbol{x}) \;=\; \frac{\rho_0 g}{2m}\nabla^2\delta\rho(t,\boldsymbol{x})\;, \tag{3.46}$$

which propagates with the speed of sound in BECs

$$c_s^2 \;=\; \frac{\rho_0 g}{2m}\;. \tag{3.47}$$

As the density fluctuations describe a massless Klein-Gordon field, we can write it as a mode expansion

$$\delta\rho(t,\boldsymbol{x}) \;=\; \int\frac{\mathrm{d}^2k}{2\pi}A_k\left(\hat{d}_k\mathrm{e}^{-\mathrm{i}(\omega_k t-\boldsymbol{k}\cdot\boldsymbol{x})}+\hat{d}_k^\dagger\mathrm{e}^{\mathrm{i}(\omega_k t-\boldsymbol{k}\cdot\boldsymbol{x})}\right)\;, \tag{3.48}$$

with

$$A_k \;=\; \left(\frac{\hbar\rho_0 k}{c_s m}\right)^{1/2}\;. \tag{3.49}$$

At this point, let us recap the results of this section as they form the second part of the analogue. The density fluctuations of the BEC behave in the phononic regime as a massless Klein-Gordon field that effectively lives in $(2+1)$ dimensions. Those fluctuations propagate with the speed of sound in the BEC given by equation (3.47). The density fluctuations therefore take the role of the field ϕ from the relativistic field theory in equation (2.92). We have already seen that the laser phase fluctuation is the continuous probing field in this analogy. In the next chapter we discuss the interaction in more detail.

3.2.3 BEC - Laser Interactions

At this point we want to collect all the information we have gathered about BECs and interactions of electromagnetic fields with matter. We construct a system of an effectively two-dimensional BEC interacting with a laser beam, which is described by the electromagnetic field as introduced in this chapter. The BEC is assumed to be confined to the $z=0$ plane and therefore assumed to be effectively two-dimensional, whereas the laser beam (or more generally electromagnetic field) propagates purely in the z-direction.

Using equation (3.9) for the electromagnetic field and the same averaging argument, we can write for the electromagnetic interaction

$$\mathcal{L}_{\mathrm{int}} \;=\; -\frac{\alpha\rho}{2}\left(\frac{A_0\omega_L}{\sqrt{2}}+\partial_t\psi\right)^2\;. \tag{3.50}$$

As in the previous section, we now want to write the density field as some constant background plus fluctuations $\rho=\rho_0+\delta\rho$. The interaction Lagrangian then becomes

$$\mathcal{L}_{\mathrm{int}} \;=\; -\frac{1}{4}\alpha A_0^2\omega_L^2\delta\rho-\frac{1}{\sqrt{2}}\alpha A_0\omega_L\delta\rho\partial_t\psi-\frac{1}{2}\alpha\rho_0\left(\partial_t\psi\right)^2\;, \tag{3.51}$$

only keeping the parts that contribute to the dynamics of the fields. Earlier, we have dropped the first term arguing that it contributes with a constant energy to the density field. Working towards the actual feasibility of this system, this term becomes quite important so let us have

a quick look at this term

$$\mathcal{L}_{\text{int}}^{(0)} = -\frac{1}{4}\alpha A_0^2\omega_L^2\delta\rho\,, \tag{3.52}$$

where the superscript of $\mathcal{L}_{\text{int}}$ indicates the power of ψ. If we calculate the intensity of an electromagnetic field $I = \frac{1}{2}c\epsilon_0 n|E|^2$ and use the ansatz for E in equation (3.8), the intensity of an electromagnetic field can be written as

$$I = \frac{1}{4}c_0\epsilon_0 n A_0^2\omega_L^2\,. \tag{3.53}$$

We see that the zeroth-order term is proportional to the intensity of the laser beam with

$$\mathcal{L}_{\text{int}}^{(0)} = -I\frac{\alpha\rho_0}{\epsilon_0 c_0 n}\frac{\delta\rho}{\rho_0}\,. \tag{3.54}$$

using equation (3.27). The zero order effect contributes to the equation of motion for $\delta\rho$ and, thus, to the energy of the density fluctuations. This is called radiation pressure, which causes the BEC atoms to be attracted or repulsed from the point of interaction. This effect is crucial as it will induce additional noise, which scales with the intensity of the laser. In order to cancel out this effect one can use a second laser, which is oppositely detuned from the resonant frequency. The reason this works is because of the characteristics of the polarisability. Each of those detuned lasers have their own interaction with the BEC characterised by the frequency dependent polarisability. The frequency dependent part of this interaction scales with $\sim \alpha(\omega)\omega^2$. If we have a red and blue detuning by some frequency ω_m from the resonant frequency we find for $\omega_m \ll \omega_r$, using (3.19)

$$\alpha(\omega_r+\omega_m)\cdot(\omega_r+\omega_m)^2 \approx -\alpha(\omega_r-\omega_m)\cdot(\omega_r-\omega_m)^2\,, \tag{3.55}$$

which offsets the zero-order contribution. As we will be talking about BECs with alkali atoms which have multiple resonant frequencies within a reasonable range, the polarisability is simply the weighted average of single resonant frequency polarisabilities. For a multi-level system, such as Caesium 133 with D1 and D2 resonance lines, this average can be calculated to [92]

$$\alpha = \frac{2}{3}\alpha_{D2} + \frac{1}{3}\alpha_{D1}\,. \tag{3.56}$$

The quadratic term of equation (3.50) is

$$\mathcal{L}_{\text{int}}^{(2)} = -\frac{1}{2}\alpha\rho_0\left(\partial_t\psi\right)^2\,, \tag{3.57}$$

which contributes to the propagation speed of ψ. This can be seen by combining this term with the time-derivative of the free Lagrangian

$$\mathcal{L}_{\text{em}} = -\frac{1}{2\mu_0}\frac{1}{c_0^2}\left(1+\alpha\rho_0 c_0^2\mu_0\right)\left(\partial_t\psi(t,z)\right)^2\,, \tag{3.58}$$

with the effective speed of light in the medium given by[6]

$$\frac{1}{c_{\text{eff}}^2} = \frac{1}{c_0^2}\left(1 + \frac{\alpha\rho_0}{\epsilon_0}\right) . \tag{3.59}$$

The linear order term in ψ is the most important part of this interaction, as it shows how the density field couples to the laser phase perturbations

$$\mathcal{L}_{\text{int}}^{(1)} = -\frac{1}{\sqrt{2}}\alpha A_0 \omega_L \delta\rho\partial_t\psi . \tag{3.60}$$

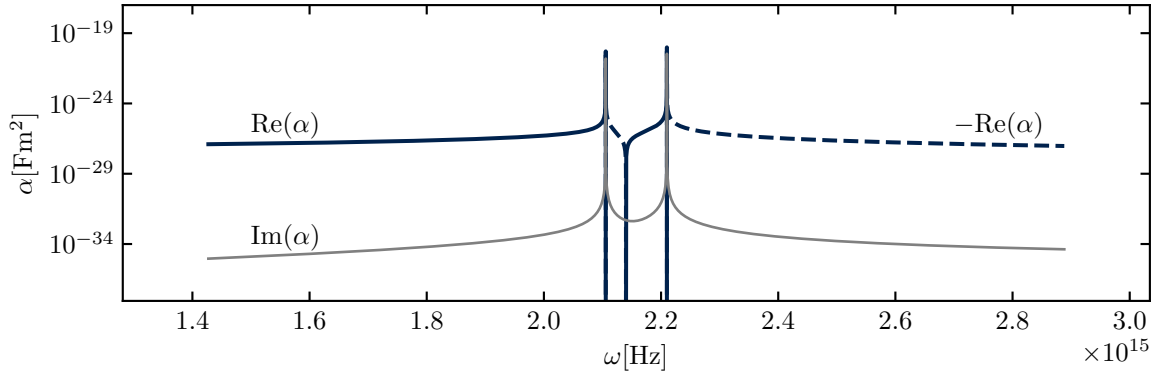

Figure 3.2 (Polarisability of ^{133}Cs) Real and imaginary part of polarisability (3.56). D1 line at 2.11×10^{15}Hz, D2 line at 2.21×10^{15}Hz.

A Note on Dimensionality. The density field in this section is $(2 + 1)$-dimensional, but how does this interaction arise from the Lagrangian of a $(3 + 1)$-dimensional density field? Using the separation ansatz in equation (3.37), the three-dimensional density can be written as $\rho_{3\text{d}} = \rho_{2\text{d}} \cdot |f(t, z; \eta)|^2$. The action of this system contains an integral over z and since f is assumed to be Gaussian, we find $\int \text{d}z\, |f|^2 = 1$. The interaction term therefore has exactly the same form in two and three dimensions and we can replace the three-dimensional density with $\rho_{2\text{d}}\delta(z)$.

The Analogue. In the previous sections, we have seen that the system consisting of a localised laser beam interacting with an effectively two-dimensional BEC can be written as the sum of

[6] Using the identity $\mu_0\epsilon_0 c_0^2 = 1$.

the following Lagrangians

$$\mathcal{L}_{\text{BEC}} = \frac{1}{2}\left(\frac{1}{c_s^2}\left(\partial_t\delta\rho(t,\boldsymbol{x})\right)^2 - \left(\nabla\delta\rho(t,\boldsymbol{x})\right)^2\right)\delta(z)\,, \tag{3.61a}$$

$$\mathcal{L}_{\text{em}} = \frac{1}{2\mu_0}\left(\frac{1}{c_0^2}\left(\partial_t\psi(t,z)\right)^2 - \left(\partial_z\psi(t,z)\right)^2\right)\delta(\boldsymbol{x}-\boldsymbol{X}(t))\,, \tag{3.61b}$$

$$\mathcal{L}_{\text{int}} = -\alpha\frac{A_0\omega_L}{\sqrt{2}}\delta\rho(t,\boldsymbol{x})\partial_t\psi(t,z)\delta(z)\delta(\boldsymbol{x}-\boldsymbol{X}(t))\,, \tag{3.61c}$$

where we have introduced the trajectory $\boldsymbol{X}(t)$ which describes the point of interaction between the laser and the BEC. We see that this system is equivalent to the relativistic field theory in (2.92), in the sense that it is described by the same Lagrangian, thus, providing us with the opportunity to probe the Unruh effect in an analogue system. The phase fluctuations ψ and density fluctuations $\delta\rho$ take the role of the fields ψ and ϕ.

The interaction between the laser and the BEC takes place at a single point in the (x,y) plane whose trajectory is described by $\boldsymbol{X}(t)$ indicated by the delta distributions in the Lagrangian. Now, that we have established the analogue by mapping the Lagrangian of the physical system to one of the continuous detector model (2.92), we can use the results from our discussion of continuous detectors, in particular the solution to the equation of motion for the phase fluctuations (2.96). This solution tells us that the laser phase carries contributions from the density fluctuations in the BEC

$$\psi(t,z) = \psi_0(t,z) + \frac{1}{2}\frac{\alpha}{\epsilon_0}\frac{\omega_L}{c_0}\delta\rho\left(t-\left|\frac{z}{c}\right|, \boldsymbol{X}\left(t-\left|\frac{z}{c}\right|\right)\right)\,, \tag{3.62}$$

where $\psi_0(t,z)$ is the phase of the laser without interaction. The coupling constant corresponding to the coupling ϵ in the relativistic model is given by

$$\epsilon = \frac{\alpha\rho_0}{\epsilon_0}\frac{\omega_L}{c_0}\,, \tag{3.63}$$

which can be seen from equation (3.62), by rewriting the density fluctuations as the dimensionless field $\delta\rho/\rho_0$. Note, that ρ_0 is a two-dimensional number density, such that ϵ is indeed dimensionless. The field ψ in equation (3.62) are the dimensionless phase fluctuations from the original ansatz for the electromagnetic field. The factor $A_0/\sqrt{2}$ cancels out in order to reverse the previously applied rescaling. If we were to calculate excitation rates of this continuous detector, we would notice the same acceleration dependence as in the idealized theory. Thus, this analogue system provides us with means to probe the Unruh effect. Moving the laser beam on a circular trajectory as given by equation (2.40), the circular Unruh temperature (2.103) is

$$k_{\text{B}}T_{\text{U}} = \frac{\gamma_s}{2\pi}\hbar\Omega_R\left(\frac{v}{c_s}\right)^2\,, \tag{3.64}$$

using $\Omega_R = c_s/R$ and the expression for the circular acceleration $\widetilde{a} = v^2/R$. In this analogue system, the phase fluctuations of the laser beam is the detector that effectively probes this temperature.

The gamma-factor is now defined in terms of the speed of sound in the BEC, which is

indicated by the subscript 's'

$$\gamma_s \;=\; \frac{1}{\sqrt{1-\frac{v^2}{c_s^2}}}\,. \tag{3.65}$$

The Unruh temperature is therefore a function of the speed of the angular motion in relation to the speed of sound in the system $\frac{v}{c_s}$, the speed of sound c_s and the radius of the orbit R. On further inspection, we recognise that the Unruh temperature increases for increasing ratios v/c_s, for decreasing radii R and increasing speed of sound c_s.

The formula for the analogue Unruh temperature uses the simplified prediction for the linear acceleration motion. We have seen in the previous chapter that the $(2+1)$-dimensional Unruh temperature actually contains an energy dependent factor (see section 2.5). As the next chapter is all about a conceptual feasibility estimate we will further use this justified simplification.

Conceptual Detection Scheme. The previous discussion showed that we can construct a physical system which shows the characteristic acceleration dependence for the Unruh effect. But how would such an experiment look like? This section discusses a conceptual experimental setup as shown in figure 3.3, and we will later give a detailed operator description that justifies this approach. For now, consider the following system: A laser beam of frequency ω_L passes a modulator that creates two frequency side bands with frequencies $\omega_L \pm \omega_m$, where ω_m is the modulation frequency. Subsequently, the beam passes through a filter which filters out the central frequency ω_L. As we have seen while creating the analogue it is necessary to have two oppositely detuned frequency bands in order to minimise the zero order effect of the laser on the BEC. The two modulated sidebands achieve exactly that.

The beam is then rotated with a deflector on a circular trajectory such that the laser beam, with the help of appropriate lenses, perpendicularly passes the effectively two-dimensional BEC. The laser beam is subsequently detected at a photo diode. There are various considerations that complicate the calculations, however, for the sake of this discussion we use the following simplified view. We assume the BEC initially is prepared in a state of zero temperature. The analogue model showed that a laser beam interaction with this BEC on a circular trajectory will probe this vacuum state and density fluctuations in the BEC will transduce into the phase fluctuations of the laser. As such, the thermal state that we would expect to see on this accelerated trajectory is therefore entirely attributed to the Unruh effect. The temperature of this state is given by the Unruh temperature in equation (2.103). Bearing this in mind, we can calculate and measure correlations in the laser phase, as we will see in the next section.

The Signal. We will show the exact measurement process later in chapter IV. For now, we will use the simplified view that the detected signal is the power spectral density (PSD) of the phase fluctuations

$$S_\psi(\omega) \;=\; \int \mathrm{d}t\; \mathrm{e}^{-\mathrm{i}\omega t}\,\langle\psi(t)\psi(0)\rangle\;, \tag{3.66}$$

which is the Fourier transform of the unequal-time two-point correlator of the phase fluctuation field, assuming stationarity. The solution to the equation of motion for ψ in equation (3.62) can be used to express the PSD of the laser phase fluctuations in terms of the PSD of density fluctuations

$$S_\psi(\omega) \;=\; \left(\frac{1}{2}\frac{\alpha\rho_0}{\epsilon_0}\frac{\omega_L}{c_0}\right)^2 S_{\delta\rho}(\omega)\;, \tag{3.67}$$

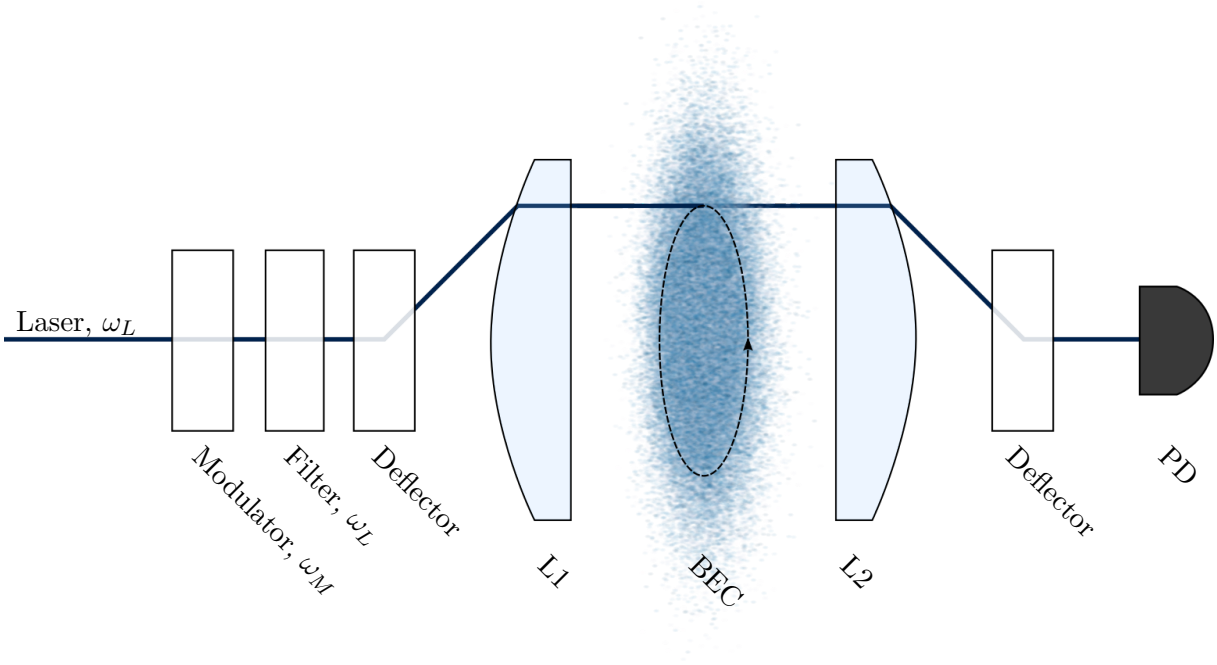

Figure 3.3 (Conceptual Detection Scheme) Detection scheme for the Unruh effect in BECs. A laser with frequency ω_L passes through a modulator with modulation frequency ω_m and a filter which filters out the central frequency ω_L. Subsequently, a deflector rotates the laser beam on a circular trajectory, and both sidebands with frequencies $\omega_L \pm \omega_m$ enter the BEC on a circular trajectory before being detected with a photo diode (PD). The two lenses (L1) and (L2) are required for the laser beam to pass the BEC perpendicularly.

where $S_{\delta\rho}(\omega)$ is the PSD of relative density fluctuations $\delta\rho/\rho_0$. We can calculate the PSD of density fluctuations explicitly using the mode expansion in (3.48). In the following, we work with the normalised density fluctuations $\delta\rho/\rho_0$ which have the same mode expansion as $\delta\rho$, in this case however, we find $A_k = \sqrt{\hbar k/(\rho_0 c_s m)}$. Until now the laser was just a one-dimensional field propagating in the z-direction. However, more realistically, the laser has a finite size which we will assume to be Gaussian with a variance corresponding to the beam diameter r_0 of the laser. Due to this finite size, all we see in the signal is an average of density fluctuations over that cross-section. We obtain the averaged density fluctuations

$$\overline{\delta\rho} \;=\; \int \mathrm{d}\boldsymbol{x}^2 \delta\rho(t,\boldsymbol{x}) \frac{1}{2\pi r_0^2} \mathrm{e}^{-\frac{x^2+y^2}{2r_0^2}} \;, \tag{3.68}$$

and can use the explicit mode representation of $\delta\rho$ to perform the integration. Completing the square results in a Gaussian integral and we find

$$\overline{\delta\rho}(t) \;=\; \int \frac{\mathrm{d}^2k}{2\pi}\, A_k \mathrm{e}^{-\frac{1}{2}r_0^2k^2} \left(\hat{d}_k \mathrm{e}^{-\mathrm{i}\omega_k t} + \hat{d}_k^\dagger \mathrm{e}^{\mathrm{i}\omega_k t}\right) . \tag{3.69}$$

Note that averaging the signal over the laser cross-section results in a factor $\exp\{-\frac{1}{2}r_0^2k^2\}$ suppressing modes with sufficiently high k. This should not pose any problem as we probe the low momentum regime of the phononic regime of the dispersion relation. The expectation value of the PSD can be calculated using

$$\left\langle \left(d_k \mathrm{e}^{-\mathrm{i}\epsilon_k t/\hbar} + d_k^\dagger \mathrm{e}^{\mathrm{i}\epsilon_k t/\hbar}\right)\left(d_{k'} + d_{k'}^\dagger\right)\right\rangle_\beta \;=\; \frac{\delta(k-k')}{\mathrm{e}^{\beta\epsilon_k}-1}\left(\mathrm{e}^{\beta\epsilon_k}\mathrm{e}^{-\mathrm{i}\epsilon_k t/\hbar} + \mathrm{e}^{\mathrm{i}\epsilon_k t/\hbar}\right) . \tag{3.70}$$

The expectation value in the equation above is assuming a thermal state at $k_\mathrm{B}T = \beta^{-1}$, where the thermal expectation value of the number operator is given by the Bose-statistics. Here, we assume that all thermality comes from the Unruh effect. Note, that a more thorough calculation is needed to assess the thermality of this state, but the assumption here will suffice for the purpose of this chapter (for a more detailed discussion, see [77]). The expression for the PSD then becomes

$$S_{\overline{\delta\rho}}(\omega) \;=\; \frac{1}{2}\int \mathrm{d}t \int_0^\infty \mathrm{d}k\; \mathrm{e}^{-\mathrm{i}\omega t} k \frac{\hbar k}{\rho_0 c_s m} \mathrm{e}^{-r_0^2k^2} \frac{\left(\mathrm{e}^{\beta\epsilon_k}\mathrm{e}^{-\mathrm{i}\epsilon_k t/\hbar} + \mathrm{e}^{\mathrm{i}\epsilon_k t/\hbar}\right)}{\mathrm{e}^{\beta\epsilon_k}-1} . \tag{3.71}$$

Note the subtle switch of integration variables from Cartesian to spherical coordinates, while already performing the integration over the angle resulting in a factor of 2π. Given the phonon-like dispersion relation we can rewrite the integration over k as an integration over ϵ_k

$$k \;=\; \frac{\epsilon_k}{\hbar c_s} \quad\Longrightarrow\quad \mathrm{d}k \;=\; \frac{\mathrm{d}\epsilon_k}{\hbar c_s} , \tag{3.72}$$

to arrive at the PSD

$$S_{\overline{\delta\rho}}(\omega) \;=\; \frac{1}{2}\frac{1}{\hbar^2 c_s^4 m\rho_0}\int \mathrm{d}t \int \mathrm{d}\epsilon_k\; \mathrm{e}^{-\mathrm{i}\omega t}\epsilon_k^2 \mathrm{e}^{-\frac{r_0^2}{c_s^2\hbar^2}\epsilon_k^2} \frac{\left(\mathrm{e}^{\beta\epsilon_k}\mathrm{e}^{-\mathrm{i}\epsilon_k t/\hbar} + \mathrm{e}^{\mathrm{i}\epsilon_k t/\hbar}\right)}{\mathrm{e}^{\beta\epsilon_k}-1} . \tag{3.73}$$

The only time dependence is in the last part of the expression above and performing the t-integration turns out to be a delta distribution

$$S_{\overline{\delta\rho}}(\omega) \;=\; \frac{\pi}{\hbar c_s^4 m\rho_0}\int \mathrm{d}\epsilon_k\; \epsilon_k^2 \mathrm{e}^{-\frac{r_0^2}{c_s^2\hbar^2}\epsilon_k^2} \frac{\left(\mathrm{e}^{\beta\epsilon_k}\delta(\hbar\omega+\epsilon_k) + \delta(\hbar\omega-\epsilon_k)\right)}{\mathrm{e}^{\beta\epsilon_k}-1} , \tag{3.74}$$

having factored out $1/\hbar$. Note that this expression is, as expected, symmetric in ω. If we focus on positive frequencies ω only with $\epsilon_k = \hbar\omega$, we find

$$S_{\overline{\delta\rho}}(\omega) \;=\; \frac{\pi}{\hbar c_s^4 m\rho_0}(\hbar\omega)^2 \mathrm{e}^{-\frac{r_0^2}{c_s^2\hbar^2}(\hbar\omega)^2} \frac{1}{\mathrm{e}^{\beta\hbar\omega}-1} . \tag{3.75}$$

Now, we can use this result to calculate the PSD of phase fluctuations in the laser phase

(3.67)

$$S_\psi(\omega) \;=\; \left(\frac{1}{2}\frac{\alpha\rho_0}{\epsilon_0}\frac{\omega_L}{c_0}\right)^2 \frac{\pi(\hbar\omega)^2}{\hbar c_s^4 m\rho_0} \mathrm{e}^{-\frac{r_0^2}{c_s^2\hbar^2}(\hbar\omega)^2} \frac{1}{\mathrm{e}^{\beta\hbar\omega}-1}\,. \tag{3.76}$$

This equation can be expressed in terms of mode energy per chemical potential $\widetilde{E} = \hbar\omega/\mu$ and the healing length $\xi = \hbar/\sqrt{2\mu m}$

$$S_\psi(\omega) \;=\; \left(\frac{1}{2}\frac{\alpha\rho_0}{\epsilon_0}\frac{\omega_L}{c_0}\right)^2 \frac{\pi m}{\hbar\rho_0} \widetilde{E}^2 \mathrm{e}^{-\frac{1}{2}\left(\frac{r_0}{\xi}\right)^2\widetilde{E}^2} \frac{1}{\mathrm{e}^{\mu\beta\widetilde{E}}-1}\,. \tag{3.77}$$

As mentioned before, the expectation value in the PSD is evaluated at a finite temperature T. Assuming that initially the BEC was at zero temperature, we have shown that a circular orbit gives rise to the Unruh temperature in the laser phase fluctuations. Consequently, the temperature of this thermal state is entirely given by the Unruh temperature (3.64)

$$\beta^{-1} \;=\; k_\mathrm{B} T_\mathrm{U}\,. \tag{3.78}$$

The key idea is to measure this spectrum and infer the temperature dependence due to the Unruh effect. If we wanted to extract the temperature via the detailed balance condition, note that (3.77) is valid for positive ω only. One would have to use (3.74) to calculate the PSD for negative ω in addition to (3.77). For now, we want to keep this idealised idea of a zero temperature initial state, however, this is a strong assumption to impose on any experiment. Realistically, the initial state has some non-zero initial temperature and we will later comment on that why only a sufficiently low initial temperature is necessary and why this zero temperature is a good approximation in the first place. In addition, we will comment on further experimental considerations later in this chapter.

Signal Optimisation and Signal-To-Noise Ratio. Realistically, the electromagnetic field picks up noise coming from various sources in and around the experiment, such as electronic noise. In the following, we only want to consider the shot noise induced phase noise in the laser phase, which is the result of the uncertainty in photon counting, or, more generally, associated with discrete counting processes. The shot-noise limited signal is

$$\widetilde{\psi}(t) \;=\; \psi(t) + \psi_\mathrm{sn}(t)\,, \tag{3.79}$$

where $\psi_\mathrm{sn}(t)$ is the shot noise induced phase noise. The PSD with this additional term becomes

$$\mathcal{S}(\omega) \;=\; S(\omega) + S_\mathrm{sn}(\omega)\,, \tag{3.80}$$

assuming the shot noise is uncorrelated with the signal over relevant time scales. Assuming a sufficiently high photon count, we can approximate the Poissonian shot noise by a Gaussian distribution with zero mean and variance

$$\langle\psi_\mathrm{sn}(t)\psi_\mathrm{sn}(t')\rangle \;=\; \sigma_\mathrm{sn}^2\delta(t-t') \;=\; \frac{\hbar\omega}{P}\delta(t-t')\,, \tag{3.81}$$

where ω and P are the frequency and the power of the laser, respectively. The signal-to-noise ratio (SNR) is defined as

$$\mathrm{SNR}(S) \;=\; \frac{S(\omega)}{\sqrt{\mathrm{Var}(S)}}\,, \tag{3.82}$$

which is the ratio of the signal, the PSD, and the noise defined by the standard deviation of the signal. The signal obtained from this setup can be further enhanced and optimised using a statistical approach. We perform the measurement N times, each measurement $\mathcal{S}^{(n)}(\omega), n \in \{1,\dots,N\}$ occurring over a time period T, and average the signal over the analysis resolution bandwidth B

$$\overline{\mathcal{S}}(\omega) \;=\; \frac{1}{N}\sum_n \mathcal{S}^{(n)}(\omega) \;=\; \frac{1}{N}\sum_n S^{(n)}(\omega) + \sigma_{\mathrm{sn}}^2 \;=\; \overline{S}(\omega) + \sigma_{\mathrm{sn}}^2\,, \tag{3.83}$$

where each measurement of the PSD $\mathcal{S}^{(n)}(\omega) = S^{(n)}(\omega) + \sigma_{\mathrm{sn}}^2$ is labelled with n. For any signal/noise with constant variance, averaging leads to the following variance [7]

$$\mathrm{Var}\left(\bar{\mathcal{S}}(\omega)\right) \;=\; \frac{1}{N^2}\sum_n \mathrm{Var}\left(\mathcal{S}^{(n)}(\omega)\right) \;=\; \frac{\mathrm{Var}\left(\mathcal{S}(\omega)\right)}{N}\,, \tag{3.84}$$

where the variance for each $\mathcal{S}^{(n)}$ and $S^{(n)}$ is the same, thus dropping the n superscript in the last expression of the equation above.

Note that the actual measurement is a discretised process of single measurements happening at time steps Δt. The total measurement time is then given by $T = N_t \Delta t$. In turn, this means that the measurement bandwidth is given by $1/\Delta t$ leading to a frequency resolution of $\Delta f = 1/(N_t \Delta t)$. For a fixed bandwidth, which is usually given by the measurement device, improving the frequency resolution is therefore only possible by increasing the total measurement time by a factor of B. This increase leads to a decrease of the variance with $1/B$, or an increase of the SNR with a factor of $\sqrt{B}$. The SNR of this averaged signal therefore improves by a factor of $\sqrt{NB}$ compared to the original SNR

$$\mathrm{SNR}(\overline{\mathcal{S}}) \;=\; \frac{\overline{\mathcal{S}}(\omega)}{\sqrt{\mathrm{Var}(\overline{\mathcal{S}})}} \;=\; \sqrt{NB}\,\frac{\overline{S}(\omega) + \sigma_{\mathrm{sn}}^2}{\sqrt{\mathrm{Var}(\mathcal{S})}}\,. \tag{3.85}$$

Calculating the variance of the PSD requires to calculate the 4-point correlator $\langle(\widetilde{\psi}^\dagger(t)\widetilde{\psi}(t))^2\rangle - \langle\widetilde{\psi}^\dagger(t)\widetilde{\psi}(t)\rangle^2$, which can be calculated explicitly using equations (3.79) and (3.81), assuming no correlation between the signal and shot noise. This correlator can be used to calculate the variance of $\mathcal{S}$

$$\mathrm{Var}(\mathcal{S}(\omega)) \;=\; \mathrm{Var}(S(\omega)) + 2\sigma_{\mathrm{sn}}^2 S(\omega) + \sigma_{\mathrm{sn}}^4\,. \tag{3.86}$$

If $\psi(t)$ is a stochastic signal with Gaussian fluctuating amplitudes, its variance is given by $\mathrm{Var}(S(\omega)) = 2S(\omega)^2$, such that

$$\mathrm{Var}(\mathcal{S}(\omega)) \;=\; 2S(\omega)^2 + 2\sigma_{\mathrm{sn}}^2 S(\omega) + \sigma_{\mathrm{sn}}^4\,. \tag{3.87}$$

Note that the shot noise itself is assumed to be Gaussian, so every higher order cumulant beyond second order vanishes.

[7] Using $\mathrm{Var}(\mathrm{const.}\cdot x + \mathrm{const.}) = \mathrm{Var}(\mathrm{const.}\cdot x) = \mathrm{const}^2 \cdot \mathrm{Var}(x)$.

If we assume a sufficiently small signal with $(S(\omega)+\sigma_{\mathrm{sn}}^2)/\sigma_{\mathrm{sn}}^2$ close to 1, we find

$$\mathrm{SNR} \;\approx\; \sqrt{NB}\,\frac{S(\omega)+\sigma_{\mathrm{sn}^2}}{\sigma_{\mathrm{sn}}^2}\,. \tag{3.88}$$

As mentioned in the previous section, we are interested in the signal arising due to the Unruh effect and being able to resolve it with respect to vacuum fluctuations. We therefore look at the SNR for the signal difference between the accelerated motion and a static laser beam, which we call ΔSNR. Essentially, ΔSNR is defined for the signal above the shot noise level

$$\Delta\mathrm{SNR} \;=\; \sqrt{\frac{NB}{2}}\frac{S(\omega)}{\sigma_{\mathrm{sn}}^2}\,. \tag{3.89}$$

Putting all the pieces together, namely equation (3.77), (3.81) and (3.89), we find

$$\Delta\mathrm{SNR} \;=\; \sqrt{\frac{NB}{2}}\frac{P}{\hbar\omega_L}\left(\frac{1}{2}\frac{\alpha\rho_0}{\epsilon_0}\frac{\omega_L}{c_0}\right)^2\frac{\pi m}{\hbar\rho_0}\widetilde{E}^2\mathrm{e}^{-\frac{1}{2}\left(\frac{r_0}{\xi}\right)^2\widetilde{E}^2}\frac{1}{\mathrm{e}^{\mu\beta\widetilde{E}}-1}\,. \tag{3.90}$$

In order to make a feasibility statement we need to consider experimentally accessible parameters. In the next section, we discuss experimental constraints and justify the values we choose in order to estimate the signal in equation (3.90).

3.2.4 Estimates for Experimental Parameters

Before we discuss any concrete estimates to optimise the SNR, we want to look at the relevant scaling of important physical parameters that directly enter the PSD. Note that in practice not all of those parameters are entirely independent. The SNR increases for increasing atom mass m and number density ρ_0, and for decreasing chemical potential μ and laser beam width r_0. One can now optimise the SNR with respect to those parameters, however, there are more considerations to be taken into account. First, the trajectory is chosen to have a radius of $R = 10\mu$m and a velocity of 95% of the speed of sound in the BEC, which is in reach of current experimental development. As mentioned in the chapter about the Unruh effect in analogue systems, there is nothing peculiar in exceeding the speed of sound, however, in the relativistic model this threshold imposes a hard limit which we must respect in the analogue as well. The parameters for a ^{133}Cs BEC are given in table 3.1 with which we can calculate the speed of sound in BECs to be $c_s = 1.7\times10^2\mu$m/s. This results in an Unruh temperature of

$$T_{\mathrm{U}} \;\sim\; 60\ \mathrm{pK}\,, \tag{3.91}$$

using the linear prediction as a simplification. Note that this chapter assumes an initial state at absolute zero such that Unruh temperatures of pico Kelvin are significant, however, any real experiment has a finite temperature. We will discuss this aspect later in the summary. As discussed, the circular motion temperature will include another factor of order unity. To calculate the SNR we first have to calculate the shot-noise variance

$$\sigma_{\mathrm{SN}}^2 \;=\; \frac{\hbar\omega_L}{P}\,. \tag{3.92}$$

Here, P is the power of the detected laser beam, which can be written in terms of the unmodulated laser power P_0, the modulation parameter M, as a result of the sideband modulation, and the off-resonance optical density $\widetilde{D}$

$$\widetilde{D} \;=\; \frac{2\pi\rho_0}{\lambda_L}\mathrm{Im}\,\alpha\;, \tag{3.93}$$

to obtain [93]

$$\sigma^2_{\mathrm{SN}} \;=\; \frac{2\hbar\omega_L}{M^2P_0\mathrm{e}^{-\widetilde{D}}}\;. \tag{3.94}$$

Parameter	Symbol	Value	Units
Experiment			
Experimental Realisations	N	10^6	
BEC			
Atom Mass ^{133}Cs	m	2.2085×10^{-25}	kg
Scattering Rate	Γ_{sc}	0.1	Hz
Chemical Potential	μ	$2\pi\hbar$ 9.5Hz	$\mathrm{kg\,m^2\,s^{-2}}$
Healing Length	ξ	2	μm
Density	ρ_0	10^3	$\mu\mathrm{m}^{-2}$
Scattering Length	a_s	25	pm
Transverse Confinement	$a_\perp$	1	μm
Peak Density	$\max[\rho_{3d}]$	5.6×10^{14}	cm^{-3}
Speed of Sound	c_s	170	$\mu\mathrm{m\,s}^{-1}$
Trajectory			
Trajectory Radius	R	10	μm
Velocity	v	$0.95c_s$	$\mathrm{m\,s}^{-1}$
Laser			
Beam Width	r_0	3	μm

Table 3.1 (BEC Parameters) Parameter estimates for potential implementation in experimental setups. These parameters were used to produce corresponding plots in this chapter.

By their nature, BECs are complex constructs which are difficult to create and maintain. In order to find the parameters given in table 3.1 one has to consider a few experimental constraints. The key principle behind this kind of measurement is a non-destructive measurement of the BEC which requires the photon scattering rate to be small

$$\Gamma_{\mathrm{sc}} \;=\; \frac{1}{\hbar c\pi r_0^2}\mathrm{Im}\,\alpha M^2P_0 \;\ll\; 1\;. \tag{3.95}$$

The condition therefore imposes a restriction on the beam width of the laser, its power and detuning. Furthermore, in order to resolve the phononic band with frequencies up to $\mu/\hbar$ we require

$$B \;=\; \frac{\mu}{2\pi\hbar B_m} \;>\; 1\;, \tag{3.96}$$

where the measurement resolution bandwidth B_m is determined by the lifetime of the BEC. There are several factors influencing the lifetime of a BEC, for example due to technical heating or back-action of the laser. In addition, one has to account for disturbances that the laser create in the BEC which are reflected from the edges due to the finite size of the BEC [102]. To resolve the phononic band with $B > 1$, we require a measurement bandwidth of $B_m < \mu/\hbar$.

Lastly, in order to actually obtain a measurable Unruh temperature we have to demand that $k_\mathrm{B} T_\mathrm{U} \sim \mu$ which leads to the condition $\hbar\Omega_R \sim \mu$, where all other constants, fixing v/c_s, result in a constant of order unity. This means that the radius of the trajectory has to be of the order of the healing length.

Considering all those limitations, figure (3.5) shows the SNR for the Unruh effect in a Caesium-133 BEC. The SNR indicates that the expected signal due to the Unruh effect is above the shot noise level.

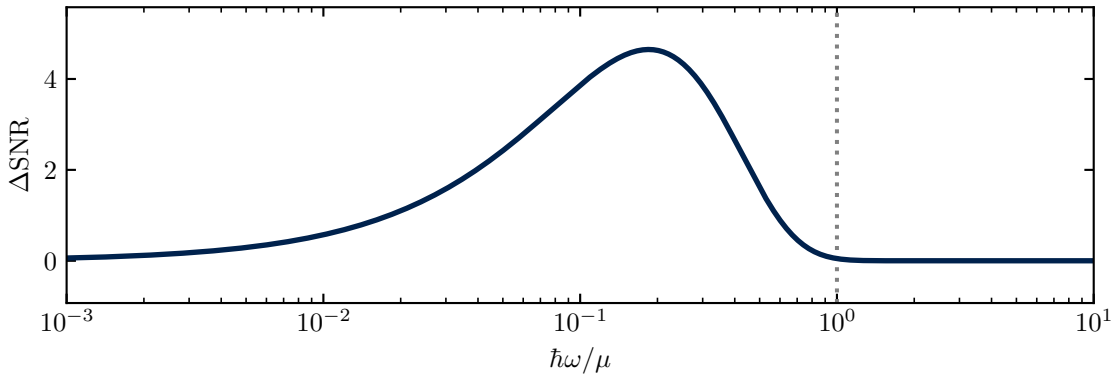

Figure 3.4 (SNR of density fluctuations) Signal-to-Noise ratio for ^{133}Cs with parameters given in table 3.1 and $B = 1$. Integrating over the phononic band to $\hbar\omega/\mu = 1$ yields $\overline{\Delta\mathrm{SN}} \approx 5.8$.

3.2.5 Summary

We saw in this section that a continuous laser beam interacting with a BEC on a circular trajectory can act as an Unruh detector. We used the continuous detector description of chapter 2.4 and applied it to a system of linearised phase fluctuations of a continuous laser beam. Light-matter interactions in the dipole approximation turned out to be the appropriate interaction between a laser beam and the BEC and together with the linearised density fluctuations in the BEC, we found an analogue system of the continuous detector model. Then, we used statistical properties of multiple measurements to define the signal-to-noise ratio of a shot-noise limited signal. In the final step, we used estimates for physical parameters to make a feasibility statement about the signal detection in the BEC using the SNR. Figure 3.5 shows that the SNR considering all mentioned simplifications and limitations suggests that a detection of the Unruh effect in BECs is in the realm of possibilities. Certainly, more careful considerations are necessary, especially regarding the simplifications of finite size systems and zero temperature initial states.

3.3 Analogue Unruh Effect in Superfluid Helium-4

In the 1930s, P. Kapitza experimentally discovered some peculiar effects of Helium-4 below a certain temperature, now commonly called the λ-point, which could only be explained by an abnormally low viscosity [103]. Those results were independently confirmed by J. Allen and A. Misener the very same year. In the years that followed, theorists tried to advance on the understanding of this phenomenon. One of the theorists was Landau who published a paper in 1941 describing this effect theoretically [104]. These early attempts have led to the model which is now known as the two-fluid model. The idea is that below the λ-point, Helium can be described as a mixture of a normal, viscous fluid and a superfluid with zero viscosity. Early attempts tried to derive a theory for superfluids starting from a microscopic theory without success. The difference in Landau's approach was to express macroscopic hydrodynamical variables in terms of quantum-mechanical operators while showing that the equations of motion reproduce equations like the continuity equation and Euler's equation.

Below this critical temperature the superfluid component of Helium rises and the normal component declines until only pure superfluid Helium remains as the temperature reaches 0K.

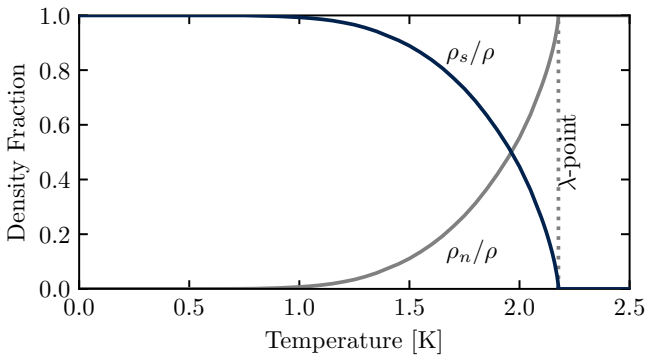

Figure 3.5 (He^4 Density Distribution) Below the λ-point with a temperature of 2.17K, the superfluid component of helium increases while the normal component decreases. Above 2.17K, Helium-4 only consists of a normal component, at $\sim$ 0K it is a pure superfluid. Data from Donnelly [105].

There are several known isotopes of Helium. The first papers on this matter discuss Helium-4 which is a bosonic system, so it should not come by surprise that cooling down bosonic Helium-4 below a critical point shows resemblance to Bose-Einstein Condensation. On the other hand, Helium-3 is a fermionic system [106]. In the following, we describe the fundamental dynamics of Helium-4 and show how this superfluid can be used as an analogue system to detect the Unruh effect.

3.3.1 Two-Fluid Model

The basic idea of the two-fluid model is to describe Helium-4 below the λ-point as a mix of two fluids – a normal, viscous fluid and a superfluid without viscosity. The total density is then given as $\rho = \rho_n + \rho_s$ consisting of the normal component ρ_n and superfluid component ρ_s. The normal component moves with a velocity profile $\boldsymbol{v}_n$, while the superfluid component moves with $\boldsymbol{v}_s$. This leads to the total mass current density $\boldsymbol{j} = \rho_n \boldsymbol{v}_n + \rho_s \boldsymbol{v}_s$.

The starting point of this model are the equations governing the dynamics of macroscopical, classical fluids and extend this description towards the quantum regime. One of those equations is the requirement of conservation of mass, leading to the continuity equation

$$\partial_t \rho + \nabla \cdot \boldsymbol{j} \;=\; 0\,, \tag{3.97}$$

where ρ is the total density and $\boldsymbol{j}$ the mass current. An assumption that has to be put into the model is that the superfluid component is inviscid and irrotational with $\nabla \times \boldsymbol{v}_s = 0$. Since both fluids have their own dynamics, we need a supplementary equation to describe the dynamics of the superfluid component [107]

$$\partial_t \boldsymbol{v}_s + \nabla \left(\frac{\boldsymbol{v}_s^2}{2} + \mu \right) \;=\; 0\,, \tag{3.98}$$

with μ being the chemical potential of superfluid Helium.

Furthermore, we want to restrict ourselves to non-dissipative processes such that entropy is conserved, in the sense that

$$\partial_t s + \nabla \cdot \boldsymbol{F} \;=\; 0\,, \tag{3.99}$$

with $s = \frac{\rho_n}{\rho} s_n + \frac{\rho_s}{\rho} s_s$ being the total entropy per mass, as weighted average of superfluid entropy s_s and normal entropy s_n, and $\boldsymbol{F}$ the entropy flux operator. Another assumption of this model is that the entropy is entirely carried by the normal component of the superfluid, i.e. $s_s = 0$, such that $\rho s = \rho_n s_n$ and consequently the entropy flux is $\boldsymbol{F} = s\boldsymbol{v}_n$. Entropy conservation therefore demands

$$\partial_t s + \nabla \cdot (s \boldsymbol{v}_n) \;=\; 0\,. \tag{3.100}$$

In addition, we have momentum conservation (for details see Khalatnikov [107]), which will simplify immensely if we assume that normal and superfluid velocities are small and, such that the the final expression can be linearised with respect to those velocities, leading to

$$\partial_t \boldsymbol{j} + \nabla p \;=\; 0\,. \tag{3.101}$$

In addition, using this linearisation assumption, equation (3.98) reads

$$\partial_t \boldsymbol{v}_s + \nabla \mu \;=\; 0\,. \tag{3.102}$$

Apart from the boundary conditions, equations (3.97),(3.100), (3.101), and (3.102) form the set of equations fully describing the dynamics of superfluid Helium-4 in the two-fluid model. This set of equations allows for distinct types of wave propagation in Helium. In the following, we will briefly discuss two types and go into more detail of a third type which proves to be relevant for the analogy.

3.3.2 Surface Fluctuations of Thin Films

The two-fluid model allows for various types of waves for the normal and superfluid component, each propagating with their own speed. Ordinary longitudinal pressure waves involving fluctuations in the total density at constant temperature are called first sound. It is characterised by a constant surface tension σ, vanishing temperature gradients $\nabla T = 0$ and non-constant total density $\rho \neq \text{const}$. In this case, normal and superfluid component move in phase with $\boldsymbol{v}_n = \boldsymbol{v}_s$.

For adiabatic processes with $p = \left(\frac{\partial p}{\partial \rho}\right)_s \rho$, the density dynamics is described by a wave equation and propagates through the bulk of the superfluid, called *first sound*, whose velocity is given by

$$u_1^2 = \left(\frac{\partial p}{\partial \rho}\right)_s . \tag{3.103}$$

Temperature waves are called second sound which are specified by a non-constant surface tension σ, a constant density ρ and vanishing pressure gradients $\nabla p = 0$, such that the mass current $\rho_s \boldsymbol{v}_s + \rho_n \boldsymbol{v}_n = 0$ vanishes. Both fluid components move with a phase shift of π. We know from thermodynamics that $\mathrm{d}\mu = -s\mathrm{d}T + \frac{\mathrm{d}p}{\rho}$ which, combined with the set of equations above, results in a wave equation for the temperature. It describes heat propagation in the superfluid and is called *second sound* with

$$u_2^2 = \frac{\rho_s}{\rho_n}\left(s^2 \frac{T}{c_P}\right) , \tag{3.104}$$

with c_P being the specific heat of Helium-4.

Third Sound. As third sound will play a fundamental role in our analogy, we will spend some time further specifying the underlying assumptions. If a viscous fluid with viscosity η_n and density ρ_n performs an oscillatory motion of frequency ω, the velocity of those oscillations cannot change significantly over a distance that is smaller than what is called the viscous penetration depth $d_{\mathrm{visc}} = \sqrt{2\eta_n/(\rho_n \omega)}$. If the depth of the fluid is smaller than this viscous penetration depth and since the normal velocity has to be zero at the walls, it is reasonable to assume that it is zero at the surface as well. The normal component can therefore be assumed to be at rest and it is possible for the superfluid component to form surface waves which propagate independently of the normal component. Figure 3.6 shows the process schematically. As the normal component carries all the entropy, waves of the superfluid component create troughs and peaks leading to an excess of the superfluid component in some parts and a deficit in other parts. This creates temperature gradients leading to evaporation and condensation effects in superfluid Helium, the temperature then being $T = T_0 + \delta T$. Of course, nonetheless the whole system is subject to boundary conditions, namely that there is no penetration of the solid bottom of the basin, i.e. $\boldsymbol{j}_\perp = 0$, and that the normal component does not move parallel to the bottom $\boldsymbol{v}_{n\parallel} = 0$. At the surface, we demand the standard condition for a free surface $\partial_t h + \boldsymbol{v} \cdot \nabla h = 0$ [108].

These evaporation and condensation processes adjust the mass conservation equation by adding a mass flux to it. The mass loss due to evaporation $J_m^{vap} = \frac{\mathrm{d}m}{\mathrm{d}t}$ is proportional to the difference of the local temperature and its surrounding temperature. Let's call this proportionality constant K such that $J_m^{vap} = K\delta T$. The vapour is assumed to be uniformly at temperature T_0 and pressure p_0. The temperature changes in the fluid would be in equilibrium with the vapour at pressure $p = p_0 + \beta \delta T$. Modifying the two-fluid model equations with those considerations, we can linearise those equations in terms of small height fluctuations δh around an equilibrium height h_0. The evolution of these surface waves, or third sound waves, is then described by [108, 109, 110]

$$\rho_s h_0 \nabla \cdot \boldsymbol{v}_s + \rho \partial_t \delta h + K\delta T = 0 , \tag{3.105a}$$

$$\rho h_0 c_P \partial_t \delta T - \rho_s h_0 s T \nabla \cdot \boldsymbol{v}_s + KL\delta T = 0 , \tag{3.105b}$$

$$\partial_t \boldsymbol{v}_s + g\nabla \delta h - \left(s - \frac{\beta}{\rho}\right)\nabla \delta T = 0 , \tag{3.105c}$$

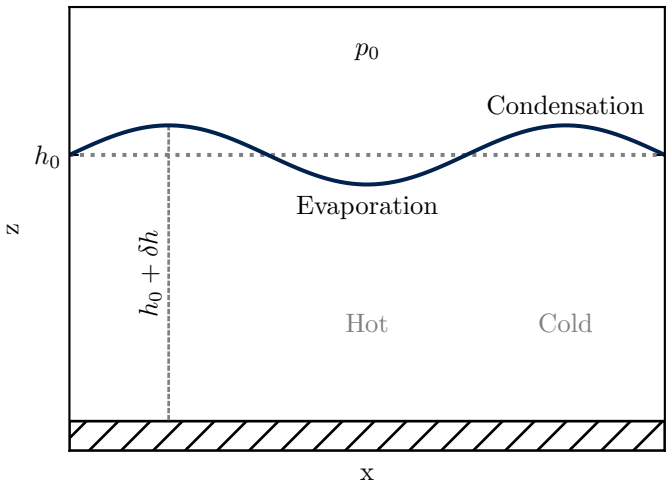

Figure 3.6 (Superfluid Helium-4 Setup) Waves propagating on the surface of Helium-4 perturbing the height $h(x)$ of the fluid by some offset $\delta h(x)$ around an equilibrium height h_0. Fluctuations in the superfluid component create entropy differences in Helium, leading to evaporation and condensation at the surface.

where L is the latent heat of vaporisation per gram of the fluid and g a parameter describing the restoring force. By assuming a planar wave ansatz for the height perturbations of the superfluid helium (and all other quantities in a similar way), viz.

$$\delta h(t, \boldsymbol{x}) \;=\; \delta h_0 \exp\left\{\mathrm{i}(\omega t - \boldsymbol{k}\cdot\boldsymbol{x})\right\} \;, \tag{3.106}$$

the equations above simplify to

$$\begin{pmatrix} \rho_s h_0 k & \omega\rho & -\mathrm{i}K \\ \rho_s h_0 k s T_0 & 0 & \rho h_0 c_P \omega - \mathrm{i}KL \\ \omega & -gk & \left(s - \frac{\beta}{\rho}\right) k \end{pmatrix} \begin{pmatrix} \boldsymbol{v}_0 \\ \delta h_0 \\ \delta T_0 \end{pmatrix} \;=\; 0 \;. \tag{3.107}$$

Non trivial solutions to these equations require the relation [111]

$$\frac{\omega^2}{k^2} \;=\; \frac{\rho_s}{\rho} h_0 g + \frac{\rho_s}{\rho} s T \frac{\left(s - \frac{\beta}{\rho}\right) - \mathrm{i}\frac{Kg}{\omega\rho}}{c_P - \mathrm{i}\frac{KL}{\rho\omega h_0}} \;. \tag{3.108}$$

This dispersion relation is rather complex but in essence describes how surface waves on superfluid Helium-4 propagate. This expression can be simplified with further assumptions, two of which are commonly mentioned in the literature – the no vapour limit and the isothermal limit. Below 0.5 Kelvin, the no vapour limit assumes that the vapour pressure and its interaction with the superfluid can be neglected. In this case, the pressure p can be set to zero in the equations and there is no entropy or mass flux at the surface. The isothermal limit on the other hand is more interesting for the purpose of establishing the analogy.

A note on thin films. The dispersion relation for thick films leads to the propagation speed of surface waves [109]

$$\omega^2 \;=\; \left(\rho g + \sigma k^2\right) \frac{k \tanh(k h_0)}{\rho} \;, \tag{3.109}$$

which we use in the approximation $k h_0 \ll 1$. All these equations show similarities to gravity waves in classical fluid dynamics and as such we could think of the constant g as the gravitational acceleration. However, it is shown in [112] that the restoring force in thin film superfluids results in an effective coupling g, which comprises a gravitational effect and a van-der-Waals effect due to the interaction with the surrounding basin. In this case, we find

$$g \;=\; g_0 + 3\frac{\alpha_{\mathrm{vdw}}}{h^4} \;\approx\; 3\frac{\alpha_{\mathrm{vdw}}}{h^4} \;, \tag{3.110}$$

with h being the height of the film and α_{vdw} a material-specific van-der-Waals coupling constant. The second part clearly dominates for thin films and is several orders of magnitude larger than g_0. We might as well drop the gravity contribution in this thin film limit.

Isothermal Limit. Surface waves of the superfluid component create troughs and peaks and since the superfluid component does not carry entropy, the entropy of the normal component creates temperature gradients ∇T at those points, which are accompanied by pressure gradients ∇p in the vapour. The evaporation rate on the surface J_m^{vap} is proportional to the temperature difference $T - T_m$, T_m being the mean temperature of the superfluid. There is an effective mechanism of evaporation and condensation of the superfluid that cools down the troughs and heats up the crests, such that it is reasonable to assume that temperature gradients ∇T, as well as any evaporation at the surface J_m^{vap} and pressure differences ∇p vanish

$$\nabla T \;=\; 0 \quad , \quad \nabla p \;=\; 0 \quad , \quad J_m^{vap} \;=\; 0 \,. \tag{3.111}$$

Until now, we have kept the subscripts to distinguish between the superfluid component and total density. In a certain temperature regime, at around 1K, we can see from figure (3.5) that almost the whole fluid can be treated as superfluid. We will therefore omit the distinction in the following and drop the subscripts, i.e. $\rho = \rho_s$. In this case, the governing equations arising from equations (3.105) are

$$h_0 \frac{\hbar}{m} \nabla^2 \phi + \partial_t \delta h \;=\; 0 \,, \tag{3.112a}$$

$$\frac{\hbar}{m} \partial_t \phi + g \delta h \;=\; 0 \,, \tag{3.112b}$$

where we have used that $\boldsymbol{v}_s = \frac{\hbar}{m} \nabla \phi$ can be represented as the gradient of a velocity potential. If we want to think of equations (3.112) as the equations of motion for a field ϕ and its conjugate momentum δh, the corresponding Hamiltonian is

$$\mathcal{H} \;=\; \frac{1}{2} \rho \left[\frac{\hbar}{m} h_0 \left(\nabla \phi\right)^2 + g \frac{m}{\hbar} \left(\delta h\right)^2 \right] \,, \tag{3.113}$$

where the constant ρ is introduced for dimensional convenience. The equations of motion (3.112) can be calculated from this Hamiltonian using

$$\rho\partial_t\delta h \;=\; \frac{\delta\mathcal{H}}{\delta\phi}\,, \tag{3.114a}$$

$$\partial_t\phi \;=\; -\frac{1}{\rho}\frac{\delta\mathcal{H}}{\delta(\delta h)}\,. \tag{3.114b}$$

These equations already show a striking, fundamental similarity with the BEC formalism. The dynamic fields here are the velocity potential ϕ and the field $\rho\delta h$ which is an effective, dynamic two-dimensional density, just as in the BEC case. In this limit, equations (3.112a) and (3.112b) can be combined into an equation for δh

$$\partial_t^2\delta h - h_0 g\nabla^2\delta h \;=\; 0\,. \tag{3.115}$$

These height fluctuations on thin-film superfluid Helium in the isothermal limit therefore behave like a massless Klein-Gordon field propagating with the velocity

$$c_3^2 \;=\; \left(\frac{\omega}{k}\right)^2 \;=\; gh_0\,. \tag{3.116}$$

In this limit, height fluctuations on superfluid helium can effectively be described as a scalar field in $(2+1)$d propagating with c_3. Note that this limit effectively applies the approximations $kh \ll 1$ and $\rho g \gg \sigma k^2$ to the thick film dispersion relation (3.109). We will refer to this branch of the dispersion relation as the phononic branch.

The equation of motion for δh is reproduced by the Lagrangian

$$\mathcal{L} \;=\; \frac{1}{c_3^2}\left(\partial_t\delta h(t,\boldsymbol{x})\right)^2 - \left(\nabla\delta h(t,\boldsymbol{x})\right)^2\,. \tag{3.117}$$

This is the Lagrangian of a massless field in $(2+1)$ dimensions and by comparison with the relativistic model in equation (2.92), we see that the height field takes the role of the field whose vacuum is probed by the continuous detector. As we are interested in the quantum behaviour of these height fluctuations in the ultra-cold environment of the setup, we can write the height fluctuation field as a mode expansion

$$\delta\hat{h}(t,\boldsymbol{x}) \;=\; \int\frac{\mathrm{d}^2k}{2\pi}A_k\left(\hat{d}_k\mathrm{e}^{-\mathrm{i}(\omega_k t-\boldsymbol{k}\cdot\boldsymbol{x})} + h.c.\right) \tag{3.118}$$

with annihilation operators $\hat{d}_k$, dispersion relation $\epsilon_k = \hbar c_3 k$ and

$$A_k \;=\; \left(\frac{\hbar c_3 k}{\rho g}\right)^{1/2}\,. \tag{3.119}$$

To complete the analogue model, we derive in the next section the interaction between external electromagnetic fields and height fluctuations on superfluid Helium.

A Note on Surface Waves. In this description, the equations certainly show similarities to classical fluids. However, surface waves on thin films of classical fluids are highly suppressed by

the viscosity, as we have seen for the normal component of the superfluid. As the superfluid component does not possess this restriction it is an excellent candidate for this analogue. In addition, in a thin film limit, third sound effects dominate first and second sound effects [113].

3.3.3 Superfluid Helium-4 - Laser Interactions

Superfluid Helium-4 interacts with an external electromagnetic field in the same way as a BEC – it develops dipoles according to the polarisability of Helium-4. In this case, however, there are a few subtle differences compared to the BEC. First, we assume a constant density but instead look at height fluctuations as suggested by the equations of motion for $\rho\delta h$. Hence, this height displacement field interacting with the laser has to arise from an effective description of this theory. Instead of a Gaussian profile in the z-direction, as it was the case in the BEC setup, the Helium-4 is confined in the z-direction, specifically it is located between $z = 0$ which forms the bottom of the basin and the free surface at $z = h(t, \boldsymbol{x})$. Note, that the free surface field $h(t, \boldsymbol{x}) = h_0 + \delta h(t, \boldsymbol{x})$ propagates in the (x, y)-plane and can be described as fluctuations δh around some equilibrium height h_0. Second, the resonance structure of Helium atoms leads to a conceptual difference. Compared to Alkali atoms, their resonant frequency is in a regime in which it is experimentally unfeasible to use a red and blue detuned laser beam. Realistically, it is not feasible to use a two sideband structure as before. We will later comment on the consequences of that.

The interaction Lagrangian is still given by equation (3.28), however, on the level of the action we find

$$S \;=\; -\int \mathrm{d}t \int \mathrm{d}\boldsymbol{x} \int_0^{h(t,\boldsymbol{x})} \mathrm{d}z \; \frac{\alpha\rho_N}{\sqrt{2}} A_0 \omega_L \partial_t \psi(t, z) \;, \tag{3.120}$$

whose integration limits in the z-direction reflect the spatial confinement of the Helium. In the following, we derive an effective Lagrangian for this interaction. First, we can calculate how this interaction contributes to the equation of motion for ψ by varying the action using Luke's variation principle [114]

$$\delta S \;=\; -\frac{\alpha\rho_N}{\sqrt{2}} A_0 \omega_L \iint \mathrm{d}t\mathrm{d}\boldsymbol{x} \int_0^{h(t,\boldsymbol{x})} \mathrm{d}z \; \partial_t \delta\psi(t, z) - \frac{\alpha\rho_N}{\sqrt{2}} A_0 \omega_L \iint \mathrm{d}t\mathrm{d}\boldsymbol{x} \; \partial_t \psi(t, h(t, \boldsymbol{x}))\delta h \;. \tag{3.121}$$

The Leibniz rule shows that

$$\frac{\mathrm{d}}{\mathrm{d}t} \int_0^{h(t,\boldsymbol{x})} \mathrm{d}z \; \delta\psi(t, z) \;=\; \partial_t h(t, \boldsymbol{x}) \, \delta\psi(t, h(t, \boldsymbol{x})) + \int_0^{h(t,\boldsymbol{x})} \mathrm{d}z \; \partial_t \delta\psi(t, z) \;, \tag{3.122}$$

which can be used to rewrite the first part in equation (3.121)

$$\delta S \;=\; \frac{\alpha\rho_N}{\sqrt{2}} A_0 \omega_L \iint \mathrm{d}t\mathrm{d}\boldsymbol{x} \; \partial_t h(t, \boldsymbol{x}) \, \delta\psi(t, h(t, \boldsymbol{x})) - \frac{\alpha\rho_N}{\sqrt{2}} A_0 \omega_L \iint \mathrm{d}t\mathrm{d}\boldsymbol{x} \; \partial_t \psi(t, h(t, \boldsymbol{x}))\delta h \;, \tag{3.123}$$

where we drop the total time derivative as it does not contribute to the equations of motion. After absorbing a factor of $A_0/\sqrt{2}$ into ψ, the equation of motion for ψ contains the standard free part and a contribution from the interaction above

$$\frac{1}{c_0^2}\partial_t^2 \psi(t, z) - \partial_z^2 \psi(t, z) \;=\; \alpha\rho_N \omega_L \mu_0^2 \partial_t \delta h(t, \boldsymbol{x}) \delta(z) \delta\left(\boldsymbol{x} - \boldsymbol{X}(t)\right) \;. \tag{3.124}$$

Note, that we linearised with respect to $\delta h(t, \boldsymbol{x})$ such that a Taylor expansion of $\delta\psi(t, h(t, \boldsymbol{x}))$ in the variation of the action leads to a simplified $\delta(z)$ in the equation of motion. Again, this equation of motion is of the exact form as in the relativistic model and shows once more that height fluctuations transduce into phase fluctuations of the laser. A circular motion will exhibit the same characteristic dependence on the acceleration as required for the Unruh effect. We can solve the equation above to obtain [8]

$$\psi(t,z) \;=\; \psi_0(t,z) + \frac{1}{2}\frac{\alpha\rho_N}{\epsilon_0}\frac{\omega_L}{c_0}\delta h\left(t - \left|\frac{z}{c}\right|, \boldsymbol{X}\left(t - \left|\frac{z}{c}\right|\right)\right) \;, \tag{3.125}$$

where $\psi_0(t,z)$ is the solution of equation (3.124) for $\alpha = 0$.

Conceptual Detection Scheme. The previous section showed that the signal of interest is in the phase of the laser, it is therefore essential to build an experiment that is sensitive to those laser phase fluctuations. One possible, rather simple setup is a homodyning detection scheme as in figure 3.7. A beam splitter is used to create a signal and reference arm from an incoming laser. The lower arm is the signal arm that probes height fluctuations on Helium-4 on a circular trajectory. After being reflected back from the bottom of the basin, the signal arm is being reunited again with the reference arm at a second beam splitter. Subsequently, the signal is being detected with two photo diodes. This should only be viewed as a guide to more sophisticated setups including intensity optimisation of the signal arm.

The Signal, Optimisation, and Signal-to-Noise Ratio. As in the case of density fluctuations in BECs, we want to look at the PSD of relative height fluctuations on superfluid helium $\delta h/h_0$, where the derivation of the PSD is analogous to the one in the previous chapter. Again, before calculating the PSD, averaging over the laser width is necessary

$$\overline{\delta h}(t) \;=\; \frac{1}{\sqrt{2V}}\sum_{k\neq 0} A_k \mathrm{e}^{-\frac{1}{2}r_0^2k^2}\left(\hat{d}_k \mathrm{e}^{-\mathrm{i}\omega_k t} + h.c.\right) \;, \tag{3.126}$$

and we obtain

$$S_{\overline{\delta h}}(\omega) \;=\; \frac{\pi(\hbar\omega)^2}{\hbar h_0^2 c_s^2 \rho g}\mathrm{e}^{-\frac{r_0^2}{c_s^2\hbar^2}(\hbar\omega)^2}\frac{1}{\mathrm{e}^{\beta\hbar\omega}-1} \;. \tag{3.127}$$

Here, the speed of sound is replaced by the third sound $c_s = c_3$. The PSD of phase fluctuations is given by the conversion factor (gain) in equation (3.125)

$$S_\psi(\omega) \;=\; \left(\frac{\alpha\rho_N h_0}{\epsilon_0}\frac{\omega_L}{c_0}\right)^2 \frac{\pi(\hbar\omega)^2}{\hbar h_0^2 c_s^2 \rho g}\mathrm{e}^{-\frac{r_0^2}{c_s^2\hbar^2}(\hbar\omega)^2}\frac{1}{\mathrm{e}^{\beta\hbar\omega}-1} \;. \tag{3.128}$$

Compared to the PSD in the BEC case, there is a factor of 2 in the brackets as the laser passes the fluid twice. The key quantity of interest is again the SNR for the averaged signal. The derivation of the difference signal SNR is analogous to the one in equation (3.90) of the previous chapter

$$\Delta\mathrm{SNR} \;=\; \sqrt{\frac{NB}{2}}\frac{P}{\hbar\omega_L}\left(\frac{\alpha\rho_N}{\epsilon_0}\frac{\omega_L}{c_0}\right)^2 \frac{\pi(\hbar\omega)^2}{\hbar c_s^2 \rho g}\mathrm{e}^{-\frac{r_0^2}{c_s^2\hbar^2}(\hbar\omega)^2}\frac{1}{\mathrm{e}^{\beta\hbar\omega}-1} \;. \tag{3.129}$$

[8] Using the relation between the vacuum permittivity ϵ_0, the speed of light in vacuum c_0 and the vacuum permeability μ_0, $\mu_0\epsilon_0 = c_0^2$.

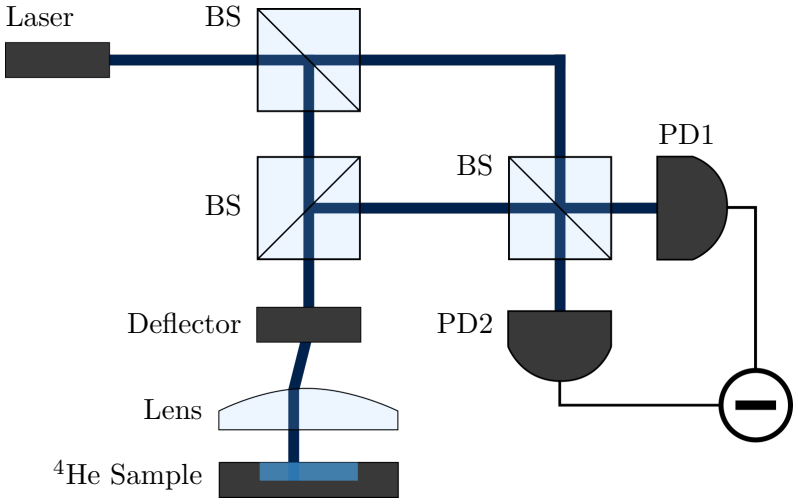

Figure 3.7 (Conceptual Setup) Possible homodyning setup with local oscillator. The incoming laser beam is split into a signal and a reference arm with a beam splitter (BS). The lower arm passes through a beam splitter (BS) and a subsequent deflector and lens. Then, moving on a circular trajectory, it passes through the sample of superfluid helium, is reflected back from the bottom of the container, and passes through the BS again. Both arms are combined again in another beam splitter and detected at two photo diodes (PD1) and (PD2).

3.3.4 Estimates for Experimental Parameters

Before reviewing the exact numbers, let us recap the assumptions that go into the model, further restricting possible parameters. An advantage of this system compared to BECs is that in the regime of interest the only tunable parameter of the superfluid is its height, so all approximations in this section impose a limit on the film height of the superfluid. First, we assumed a thin film limit, which means the effective coupling g is dominated by van-der-Waals interactions and we can neglect any gravitational effect. Most of the materials that are being used in superfluid Helium experiments have a van-der-Waals coupling of the same order as the one for a quartz substrate as given in table 3.2 [105]. This assumption is therefore valid up to a film height of around $1\,\mu$m. Second, we only consider waves with $kh_0 \ll 1$. Third, the equations are only valid in the phononic regime of the dispersion relation. From equation (3.109) we can see that this is the case for

$$\sigma k^2 \ll \rho g \,, \tag{3.130}$$

imposing a threshold of $k^2 = \rho g/\sigma$. This threshold leads to a characteristic mode energy

$$\mu = \hbar g \sqrt{\frac{\rho h_0}{\sigma}} \,, \tag{3.131}$$

up to which the phononic approximation is valid. The speed of sound for the parameters as given below is approximately $c_3 = 3.2 \times 10^{-2}\,\mathrm{m\,s^{-1}}$. The gain factor can be more conveniently

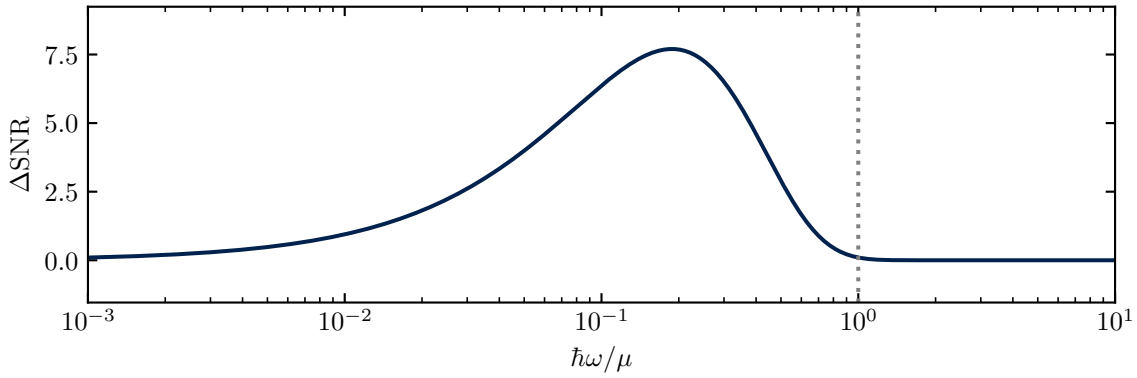

Figure 3.8 (SNR of Height Fluctuations) Signal-to-noise ratio for ^{4}He with parameters as given in table 3.2.

written in terms of the index of refraction n (using equation (3.27))

$$\left(\frac{\alpha\rho_N}{\epsilon_0}\frac{\omega_L}{c_0}\right)^2 = \left(\frac{(n^2-1)\omega_L}{c_0}\right)^2 . \tag{3.132}$$

The SNR of height fluctuations is shown in figure 3.8.

Parameter	Symbol	Value	Units
Experiment			
Experimental Realisations	N	10^6	
Helium-4			
Film Height	h_0	200	nm
Mass Density	ρ	145	kg/m^3
Surface Tension	σ	37.9×10^{-5}	Jm^{-2}
Van-der-Waals Coupling	α_{vdW}	2.6×10^{-24}	m^{5}s^{-2}
Atom. Pol.	α	2.3×10^{-41}	A^{2}s^4/kg
Index of Refraction	n	1.025	
Laser			
Frequency	ω_L	$(2\pi)2\times10^{14}$	rad/s
Beam Width	r_0	10	μm
Beam Power	P	50	mW
Trajectory			
Radius	R	60	μm
Ang. Speed	v	$0.95c_3$	m/s

Table 3.2 (Helium-4 Parameters) Parameter estimates for potential implementation in experimental setups. These parameters were used to produce corresponding plots in this chapter.

3.3.5 Summary

In this chapter we have developed the theory for an analogue model to detect the Unruh effect in thin film superfluid Helium-4. The light-matter interactions in section 3.1 could be equally applied to this system. We saw that phase fluctuations in the laser beam couple to height fluctuations on the superfluid Helium surface. The SNR suggests that, assuming a zero temperature initial state, a detection of the Unruh effect in this system is conceptually possible. The assumption of a zero temperature initial states seems a rather strong assumption in the context of superfluids, which we will comment on in the next section.

3.4 Finite Size and Finite Temperature

In this chapter, there have been resurfacing questions about what the effects of finite size systems and finite initial temperatures are on the expected Unruh effect signal. A finite size results in mode discretisation in the system depending on its exact geometry. This affects the calculation of response functions and power spectra. We could make a generalised estimate of those effects by looking at the wave with the lowest wavelength that fits into the geometry. Considering a basin of length L, the wave has a wavelength $\lambda = 2L$, or equivalent a wave vector $k = \frac{\pi}{L}$. This creates a low frequency cutoff in the power spectrum as waves with higher wavelengths are suppressed by the geometry, however, a more detailed analysis is necessary to make more qualified statements.
Throughout this chapter, the PSD is assumed to be evaluated at a state with a temperature given by the Unruh temperature. As such, all expectation values are evaluated for a zero temperature initial state (with static detector), i.e. all thermality comes from the Unruh effect. Realistically, every system possesses a finite, non-zero temperature and, thus, every calculation in this chapter imposes the rather strict assumption of a zero initial temperature. Finite temperature effects on the detection of the analogue Unruh effect have been investigated in [77]. However, we showed in [56] that if the expected, linear prediction Unruh temperature, that has been used as a proxy in this chapter, is above the ambient temperature of the system, the zero temperature assumption seems to be justified (see figure 3.9). In this case, the calculations presented in this chapter remain valid, which is in particular the case for Bose-Einstein condensates.

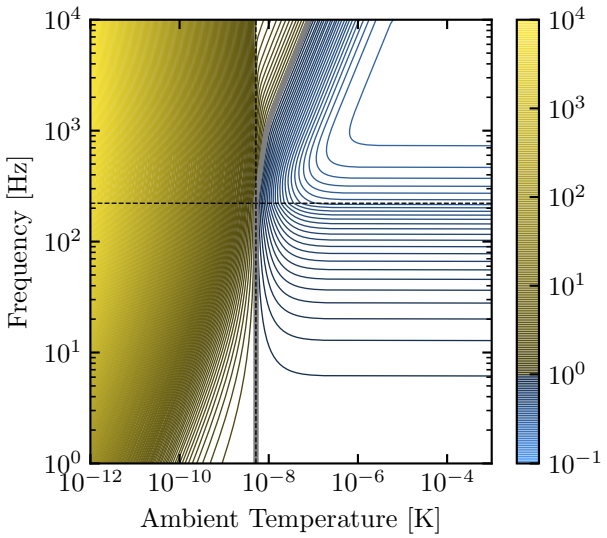

Figure 3.9 (Thermal Unruh Effect) Contour plot for ratio of temperature obtained from detailed balance condition to ambient temperature as a function of the ambient temperature and the detector frequency. Yellow contours represent a ratio of greater than 1, blue contours a ratio of less than 1, and grey line represents a ratio of 1. Dashed vertical line is at linear acceleration Unruh temperature prediction, dashed horizontal line is at the proposed frequency of the orbital rotation. Parameters given in table 3.2.

Figure 3.9 shows the ratio of the temperature obtained via the detailed balance condition T and the ambient temperature T_A of the system as a function of the ambient temperature and the detector frequency. The parameters for this plot are given in table 3.2. The contours

represent lines of constant temperature. The dashed horizontal line represents the frequency of the detector's trajectory, whereas the vertical dashed line represents the prediction of the linear Unruh temperature. The yellow contours are temperatures for which the detailed balance temperature is greater than the ambient temperature, as opposed to the blue region where it is less than the ambient temperature, while the grey border represents the ratio $T/T_A = 1$. For frequencies below the circular trajectory rotation frequency, we find that the linear prediction Unruh temperature forms the border between the regions with $T/T_A > 1$ and $T/T_A < 1$. For frequencies above the rotation frequency, the region with $T/T_A > 1$ is tilted towards the blue region.

Many interesting consequences arise from this plot, however, as mentioned above, the exact interpretation of the results that have been accumulated in this plot is still subject of further research [77, 56]. In particular, more careful considerations are necessary for a potential parameter search for any experimental implementation.

As ultra-cold atom systems, BECs are per construction extremely cold with temperatures in the pico Kelvin regime [98]. With expected Unruh temperatures in the same range, this plot suggests that the assumption of zero initial temperature seems reasonable. However on the other hand, state-of-the-art dilution fridges can cool down Helium only to a temperature of around 10 mK. The expected Unruh temperature in this case, based on the linear motion prediction, is in the nano Kelvin regime. This leads to the predicament that we used a zero temperature expectation value for a system with non-negligible finite temperature effects.

This suggests, that superfluid Helium requires for a more careful treatment. In particular, the Unruh effect needs to be calculated for a thermal initial state at the temperature of experimentally achievable ambient temperatures in the laboratory. This is a subject of ongoing research and we hope to implement the results of this study in this analogue model to better support our findings in realistic experimental environments.

3.5 Summary

In this chapter we established two analogues of the relativistic model (2.92), which consists of a $(1+1)$-dimensional scalar probing field and a second $(2+1)$-dimensional scalar field. We derived the theory behind the interaction of electromagnetic fields with polarisable matter and the effective interaction of phase fluctuations in the electromagnetic field with polarisable matter. In each of the analogues presented in this chapter, the phase fluctuations in the laser took the role of the probing field. We then introduced the Gross-Pitaevskii equation, which describes the evolution of the BEC field. This equation can be restated in terms of the BEC density and the phase of the BEC field. Linearising the resulting equations in terms of density fluctuations showed that the density fluctuation field effectively obeys a massless Klein-Gordon equation. Combined with the interaction with a laser beam, this system is mathematically analogous to the relativistic continuous detector model. We provided a schematic for a potential setup in an experiment and used the signal-to-noise ratio as key indicator for the feasibility of such an experiment. We found that the SNR of phase fluctuations in the laser beam has a peak of around 4 in the linear regime of the dispersion relation, indicating that the proposed implementation is in reach of current cold-atom experiments.

The second analogue was superfluid Helium-4 interacting with a laser beam. In superfluid Helium-4 at temperatures below 1K, the predominant fluctuations come from height fluctuations on the surface instead of density fluctuations in the bulk. We established the regime of thin-film, linearised height fluctuations starting from the macroscopic two-fluid model of superfluids and saw that, conceptually, the interaction of light with superfluid Helium is the same as the interaction of light with BECs, although there are some technical differences in calculating the effective interaction. As in the BEC case, we proceeded by calculating the signal-to-noise ratio which we found to be well above 1, indicating that, given all our assumptions, the Unruh effect is detectable.

We briefly mentioned the limitations of the approaches in the discussion of the results and more explicitly in the section on finite size and temperature effects. First, we used the linear acceleration expression for the Unruh temperature. Technically, there are energy dependent corrections of the circular Unruh temperature. However, we saw in chapter II that these corrections are bounded from above by a factor of approximately one, justifying the simplifications for a conceptual detection scheme in this chapter. More importantly, we assumed that the thermal state, as seen by an accelerated observer, has a temperature given by this linear acceleration Unruh temperature prediction. This assumes that the experiment is conducted in an environment of zero ambient temperature. For a finite ambient temperature, the calculations are more complicated as they include calculating thermal Green's functions for a circular motion. In addition, we always used continuous mode expansions, i.e. an infinitely sized systems. This assumption is a good approximation for a first estimate, however, finite size effects become important for tiny systems, such as superfluid Helium.

In summary, we found that given the simplifying assumptions the two analogue models presented in this chapter are well suited for a potential detection of the Unruh effect. However, one has to refine the analysis with more rigorous calculations of finite size and temperature effects, which is the focus of ongoing research.

IV

Signals and Detection

The idea that we can stand back and behold nature at a distance, as something discrete from our actions, is an illusion.

—Bruno Latour

In this section, we dive into the theoretical modelling of the signal detection process of the analogues outlined in the previous chapter. All detection schemes presented before rely on a photodetection process. We will therefore introduce the quantum mechanical photon counting process first and how it relates to the classical signal that will be detected with a physical photodiode. We then describe the transformations on the operators of the electromagnetic field, as it interacts with the components in the experiment. We will show what the detected signal will be, where in the measured signal the Unruh effect signal is to be expected and how to extract it. Finally, we will compare the power of the desired Unruh effect signal to the power of noise contributions in the signal.

4.1 Photodetector Model

Before we dive into the exact modelling of the detection schemes mentioned in earlier chapters, we need a mathematical model for the photodetection process. This detector model determines which signal can be detected with a photodiode and it will give us the framework to extract the desired Unruh signal. In generality, photons entering a photodiode are converted into electrons which are then subsequently multiplied to obtain a measurable signal. Photons are excitations of the electromagnetic field, so let us have a closer look at the quantum mechanical description of this field. An electric field propagating in z direction can be written as

$$\hat{\boldsymbol{E}}(t,\boldsymbol{x}) \;=\; \int_{-\infty}^{\infty} \mathrm{d}\omega\; \boldsymbol{E}_\omega \hat{a}_\omega \mathrm{e}^{-\mathrm{i}(\omega t - kz)} \;=\; \hat{\boldsymbol{E}}^{+}(t,z) + \hat{\boldsymbol{E}}^{-}(t,z)\;, \tag{4.1}$$

where in the last step we split it into a positive and negative frequency part [115]

$$\hat{\boldsymbol{E}}^{(+)}(t,\boldsymbol{x}) \;=\; \int_{0}^{\infty} \mathrm{d}\omega\; \boldsymbol{E}_\omega \hat{a}_\omega \mathrm{e}^{-\mathrm{i}(\omega t - kz)}\;, \tag{4.2}$$

with $\hat{\boldsymbol{E}}^{(+)}(t,\boldsymbol{x}) = \left(\hat{\boldsymbol{E}}^{(-)}(t,\boldsymbol{x})\right)^{\dagger}$ and annihilation operator $\hat{a}_\omega$. This split allows one to define the electromagnetic vacuum as the state for which

$$\hat{\boldsymbol{E}}^{(+)}(t,\boldsymbol{x})\,|0\rangle \;=\; 0\;. \tag{4.3}$$

In the following, we will work with one component of the electric field $\hat{E}(t,\boldsymbol{x})$ only.

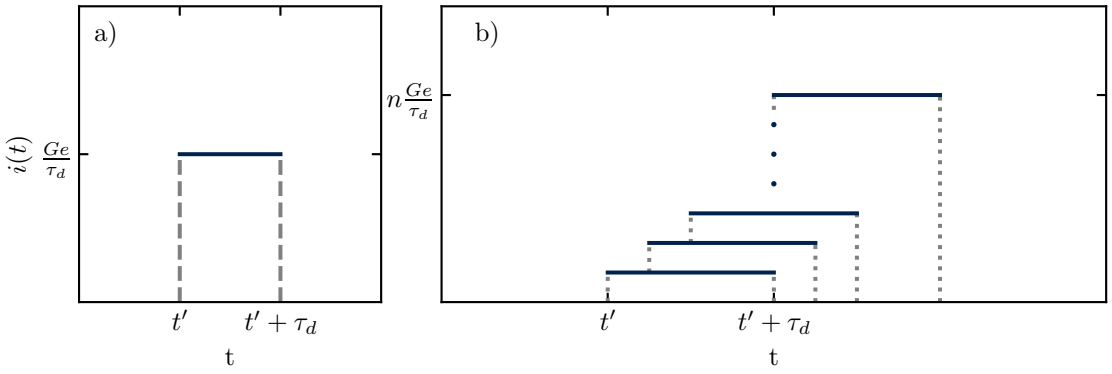

Figure 4.1 (Photodetection) a) Single photodetection with photo current $i(t \in [t', t'+\tau_d]) = \frac{Ge}{\tau_d}$ during pulse width τ_d. b) Multi-photon detection during interval $[t', t'+\tau_d]$ each triggering an additional current of $\frac{Ge}{\tau_d}$.

Classically, the photocurrent at the photo diode $i(t)$ recorded during the interval $[t-\tau_d, t]$

is simply (see figure 4.1)

$$i(t) \;=\; \int_{t-\tau_d}^{t} \mathrm{d}n(t')F(t') \;=\; n\frac{Ge}{\tau_d}\,, \tag{4.4}$$

where $F(t)$ is a function that determines the current generated by each photodetection event and n the total number of events occurring in that time interval. In the case of a time-independent response, it is given by $F(t) = eG/\tau_d$, where e is the electron charge and G is the gain of the detector.

In the following, we want to connect this classical photocurrent to the quantum mechanical flux using Carmichael's framework of photodetection [116]. The detection takes place at position $z = z_d$, which will be treated as constant. As such, we will omit any reference to the spatial coordinate, implicitly assuming all relevant quantities are evaluated at the detector position. Carmichael uses a probability approach in which the average of the classical photocurrent can be expressed as the sum of detected events weighted with their respective probabilities

$$\overline{i(t)} \;=\; \frac{Ge}{\tau_d}\sum_{n=0}^{\infty} np(n, t-\tau_d, t)\,, \tag{4.5}$$

where $p(n, t-\tau_d, t)$ is the probability for n photodetection events during the interval $[t-\tau_d, t]$. Using the photon counting formula we find [117]

$$p(n, t-\tau_d, t) \;=\; \left\langle : \frac{(\hat{\Omega}(t-\tau_d, t))^n}{n!} \exp\left\{-\hat{\Omega}(t-\tau_d, t)\right\} : \right\rangle\,, \tag{4.6}$$

where $\hat{\Omega}$ is given as the integrated intensity operator (4.8)

$$\hat{\Omega}(t-\tau_d, t) \;=\; \frac{4\pi\epsilon_0 c A_\perp}{\hbar\omega_c}\int_{t-\tau_d}^{t} \mathrm{d}t'\; \hat{I}(t')\,, \tag{4.7}$$

with carrier frequency of the electric field ω_c and photon flux cross section $A_\perp$. The colons indicate time and normal ordering with time ordering meaning that time arguments increase from right to left in any product of annihilation operators. Since Glauber, we know that the intensity of a radiation field is not the square of the electromagnetic field but rather the normal ordered product [118]

$$\hat{I}(t, z) \;=\; \hat{E}^{(-)}(t, z)\hat{E}^{(+)}(t, z)\,. \tag{4.8}$$

Using the photon counting formula, the average of the classical photocurrent can be written as

$$\overline{i(t)} \;=\; \frac{Ge}{\tau_d}\left\langle : \Omega(t-\tau_d, t) : \right\rangle\,. \tag{4.9}$$

This photo counting approach accounts for the fact that there might be several events during the measurement period τ_d (see figure 4.1 b)). Thus, with this formalism one can calculate more interesting quantities, such as correlators for the classical photocurrent

$$G_i(\tau) \;=\; \overline{i(t+\tau)i^*(t)} \;=\; \lim_{T\to\infty}\frac{1}{T}\int_{-T/2}^{T/2}\mathrm{d}t\; i(t+\tau)i^*(t)\,. \tag{4.10}$$

Here, one has to be more careful as there might be overlapping detection intervals contributing to each photo current. In a first step, we can safely assume that $\tau > \tau_d$, so that none of the

photon counts from $i(0)$ contribute to $i(\tau)$. Similar to the calculation above, we find [117]

$$\overline{i(\tau)i(0)} \;=\; \left(\frac{Ge}{\tau_d}\right)^2 \left\langle : \hat{\Omega}(\tau-\tau_d,\tau)\hat{\Omega}(-\tau_d,0) : \right\rangle \quad \text{for } \tau > \tau_d \,. \tag{4.11}$$

Now, consider overlapping intervals as shown in figure 4.1 leading to a photon self-correlation. The correlator can then be split in three segments, one only contributing to $i(0)$, one contributing to $i(\tau)$ and one contributing two both. A statistical analysis shows that [116]

$$\overline{i(\tau)i(0)} \;=\; \left(\frac{Ge}{\tau_d}\right)^2 \left\langle : \hat{\Omega}(\tau-\tau_d,\tau)\hat{\Omega}(-\tau_d,0) : \right\rangle + \left\langle : \hat{\Omega}(\tau-\tau_d,0) : \right\rangle \quad \text{for } \tau < \tau_d \,. \tag{4.12}$$

Combining the results for $\tau < \tau_d$ and $\tau > \tau_d$, we find

$$\overline{i(\tau)i(0)} \;=\; \left(\frac{Ge}{\tau_d}\right)^2 \left(\left\langle : \hat{\Omega}(\tau-\tau_d,\tau)\hat{\Omega}(-\tau_d,0) : \right\rangle + \Theta(\tau_d-\tau) \left\langle : \hat{\Omega}(\tau-\tau_d,0) : \right\rangle \right) \,. \tag{4.13}$$

The result above is a central element of the following analysis as it provides a formalism to connect the correlator of the classically measured current at the photo diode $i(t)$ with the quantum mechanical correlator of the photon flux $\hat{I}$. For τ_d much shorter than the field correlation times, i.e. we assume the integrand in Ω to not change significantly over the time τ_d, we may write

$$\overline{i(\tau)i(0)} \;=\; \left(Ge\frac{2\epsilon_0 c A_\perp}{\hbar\omega_c}\right)^2 \left\langle : \hat{I}(\tau)\hat{I}(0) : \right\rangle + (Ge)^2 \frac{2\epsilon_0 c A_\perp}{\hbar\omega_c}\Theta(\tau_d-\tau)\frac{\tau-\tau_d}{\tau_d^2} \left\langle : \hat{I}(0) : \right\rangle \,. \tag{4.14}$$

Explicitly, the time and normal ordering for $\tau > 0$, as indicated by the colons, is defined as

$$\langle : \hat{I}(t+\tau)\hat{I}(t) : \rangle \;\sim\; \langle \hat{a}^\dagger(t)\hat{a}^\dagger(t+\tau)\hat{a}(t+\tau)\hat{a}(t) \rangle \,. \tag{4.15}$$

In the linearised version with $\hat{a}(t) = \alpha_0 + \delta\hat{a}(t)$ that will be presented in this chapter, the first term in equation (4.14) dominates and we find [119]

$$\overline{i(\tau)i(0)} \;\approx\; \left(Ge\frac{2\epsilon_0 c A_\perp}{\hbar\omega_c}\right)^2 \left\langle : \hat{I}(\tau)\hat{I}(0) : \right\rangle \,. \tag{4.16}$$

As this linearisation procedure will be predominant in this section, we will work with the simplified approximation above.

A Note on Quantum Efficiency. In an idealised world, each photon produces exactly one electron in the photo detector which means the photo current is given by the numbers of photons times a constant conversion factor. Most of the real world detectors, however, most likely do not have this efficiency. In those detectors each photon produces one electron with probability $\eta \leq 1$, which is called quantum efficiency. If we wanted to model such a detector we would need to combine a beam splitter with an idealised photo detector, such as in figure 4.2. The detected photocurrent is then

$$\hat{I}(t) \;\sim\; \hat{a}_\eta^\dagger(t)\hat{a}_\eta(t) \,, \tag{4.17}$$

with $\hat{a}_\eta(t)$ given by [1]

$$\hat{a}_\eta(t) \;=\; \sqrt{\eta}\hat{a}(t) - \sqrt{1-\eta}\delta\hat{a}_0(t)\;. \tag{4.18}$$

Here, $\delta\hat{a}_0(t)$ are vacuum fluctuations entering through the second input port of the beam splitter. Throughout this thesis, however, we use a quantum efficiency of $\eta = 1$ unless specified otherwise.

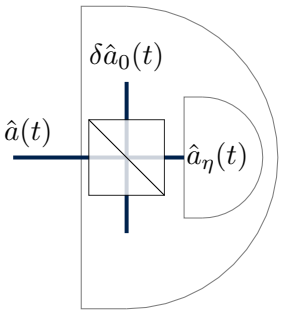

Figure 4.2 (Realistic Detector) A realistic detector consists of a beam splitter with transmission coefficient $\eta < 1$ and an ideal photodetector. The reflected part is the loss in the photodetection process, which is not being detected.

4.1.1 Power Spectral Densities

Now, we can apply the previous findings to power spectral densities of classical photo currents. The PSD is given by the ensemble average of windowed Fourier transforms of the photocurrent [119]

$$S_i(\omega) \;=\; \lim_{T\to\infty} \frac{1}{T}\,\overline{i_T^*(\omega) i_T(\omega)}\;, \tag{4.19}$$

where the windowed Fourier transform is given by

$$i_T(\omega) \;=\; \frac{1}{\sqrt{T}} \int_{-T/2}^{T/2} \mathrm{d}t\; i(t) \mathrm{e}^{-\mathrm{i}\omega t}\;. \tag{4.20}$$

The Wiener-Khinchin theorem allows us to connect the power spectral density (PSD) of the photocurrent to its autocorrelation function

$$S_i(\omega) \;=\; \int_{-\infty}^{\infty} \mathrm{d}\tau\; \mathrm{e}^{-\mathrm{i}\omega\tau} \overline{i^*(t+\tau) i(t)}_{t=0}\;, \tag{4.21}$$

which states that the PSD is essentially the Fourier transform of the autocorrelation function. This is the same definition as we used before for operators in equation (3.66). An important consequence arises for real signals, such as $i(t)$, where we have $i^*(\omega) = i(-\omega)$, such that $S_i(\omega)$ is real and

$$S_i(\omega) \;=\; S_i(-\omega)\;, \tag{4.22}$$

which can be seen directly from the definition of $S_i(\omega)$ using the fact that $i(\omega)i^*(\omega) = i^*(\omega)i(\omega)$. The PSD of any classical signal is therefore symmetric with respect to ω, however, this is in

[1] For details on beam splitters see section 4.3.

general not true for the PSD of operators $S_{\hat{I}}(\omega)$ with $\left[\hat{I}(t), \hat{I}(t')\right] \neq 0$.

Now we can use equation (4.14) for the correlator of the classical photocurrent and slightly rewrite the expectation value of the normal/time ordered product as a symmetric and an anti-symmetric part

$$\left\langle : \hat{I}(\tau)\hat{I}(0) : \right\rangle \;=\; \frac{1}{2}\left\langle : \left\{\hat{I}(\tau), \hat{I}(0)\right\} + \left[\hat{I}(\tau), \hat{I}(0)\right] : \right\rangle \,. \tag{4.23}$$

Using this expression the PSD becomes

$$S_i(\omega) \;=\; \overline{S}_{\hat{I}}(\omega) + \frac{1}{2}\int_{-\infty}^{\infty} \mathrm{d}\tau\; \mathrm{e}^{\mathrm{i}\omega\tau}\mathrm{sgn}(\tau)\left\langle : \left[\hat{I}(\tau), \hat{I}(0)\right] : \right\rangle \,, \tag{4.24}$$

where we defined the symmetrised PSD of $\hat{I}$ as

$$\overline{S}_{\hat{I}}(\omega) \;=\; \frac{1}{2}\int_{-\infty}^{\infty} \mathrm{d}\tau\; \mathrm{e}^{\mathrm{i}\omega\tau}\left\langle : \left\{\hat{I}(\tau), \hat{I}(0)\right\} : \right\rangle \,. \tag{4.25}$$

The sign function above appears due to the time-ordering within the expectation value. Within the linearisation approximation, the first term of equation (4.24) dominates and we see the important result that photodetection will always produce a symmetrised power spectral density [119]

$$S_i(\omega) \;=\; \overline{S}_{\hat{I}}(\omega) \,. \tag{4.26}$$

4.1.2 Perturbations and Noise

Most generally, we can define fluctuations of any quantity as deviations from its mean value. In particular, for the number operator, we can write

$$\delta\hat{n} \;=\; \hat{n} - \langle\hat{n}\rangle \,. \tag{4.27}$$

Here, we only consider noise that is inherently present in the laser, neglecting at first instance other noise sources such as induced noise during the photodetection process. The fluctuations in the measured photo current are therefore caused by fluctuations of the number operators. In the following, we want to calculate those fluctuations in the number operator, assuming a coherent state. We know that the Hamiltonian of the free electromagnetic field is

$$\mathcal{H} \;\sim\; \int \mathrm{d}\omega\hbar\omega\hat{a}^{\dagger}_{\omega}\hat{a}_{\omega} \,. \tag{4.28}$$

A coherent state $|\alpha\rangle$ with amplitude α and frequency ω_L can be achieved by acting with the displacement operator $D(\alpha)$ on the vacuum state $|0\rangle$ [60]

$$|\alpha\rangle \;=\; \hat{D}(\alpha)\,|0\rangle \,, \tag{4.29}$$

with

$$\hat{D}(\alpha) \;=\; \mathrm{e}^{\alpha\hat{a}^{\dagger}_{\omega_L} - \alpha^{*}\hat{a}_{\omega_L}} \,. \tag{4.30}$$

This state has the interesting property that $\langle\hat{n}\rangle = \mathrm{Var}(\hat{n}) = |\alpha|^2$. As the displacement operator does not explicitly depend on time, we find that annihilation operators of the electromagnetic

field transform as (using Hadamard's lemma with $s = 1$, see appendix A.5)

$$\hat{a}_\omega \;\to\; \hat{D}(\alpha)\hat{a}_\omega\hat{D}^\dagger(\alpha) \;=\; \alpha\delta(\omega-\omega_L)+\hat{a}_\omega\;. \tag{4.31}$$

Accordingly, the coherent electromagnetic field can be written as

$$\hat{E}(t,z) \;=\; E_0(\omega_L)\mathrm{e}^{-\mathrm{i}(\omega_L t-kz)}\left(\alpha+\delta a(t,z)\right)+\mathrm{h.c.}\;, \tag{4.32}$$

with

$$\delta a(t,z) \;=\; \int_{-\Lambda}^{\Lambda}\mathrm{d}\omega\;\delta a_\omega \mathrm{e}^{-\mathrm{i}(\omega t-kz)}\;, \tag{4.33}$$

being fluctuations in a bandwidth 2Λ about this coherent background. The approximation above assumes a slowly varying amplitude over the frequencies of the fluctuations, $E(\omega_L\pm\Lambda)\approx E(\omega_L)$. This expression is essentially the semi classical ansatz that we chose in our conceptual detection scheme of the previous chapter. The last equation tells us, that the electromagnetic field has a macroscopically occupied mode with frequency ω_L and fluctuations in a frequency band $\omega_L\pm\Lambda$. Consequently, the number operator as detected at the photo diode with $\hat{a}(t)=\alpha+\delta\hat{a}(t)$ is given by

$$\hat{n}(t) \;\sim\; \hat{a}^\dagger(t)\hat{a}(t) \;\approx\; |\alpha|^2+|\alpha|\left(\mathrm{e}^{-\mathrm{i}\varphi}\delta\hat{a}(t)+\mathrm{e}^{\mathrm{i}\varphi}\delta\hat{a}^\dagger(t)\right)\;, \tag{4.34}$$

where $\alpha=|\alpha|\mathrm{e}^{\mathrm{i}\varphi}$. Note that the expression above is a linearised approximation, neglecting terms with higher order in $\delta\hat{a}$. For future reference, we define the rotated operator with phase φ

$$\delta\hat{a}^\varphi(t) \;:=\; \mathrm{e}^{-\mathrm{i}\varphi}\delta\hat{a}(t)+\mathrm{e}^{\mathrm{i}\varphi}\delta\hat{a}^\dagger(t)\;, \tag{4.35}$$

such that we could write $\delta\hat{n}(t)=|\alpha|\delta\hat{a}^\varphi(t)$. For any fluctuation in this number operator $\hat{n}(t)=\langle\hat{n}\rangle+\delta\hat{n}(t)$ the PSD is given by

$$S_{\hat{n}}(\omega) \;=\; \int_{-\infty}^{\infty}\mathrm{d}\tau\;\mathrm{e}^{\mathrm{i}\omega\tau}\left\langle\hat{n}^\dagger(\tau)\hat{n}(0)\right\rangle \;=\; S_{\delta\hat{n}}(\omega)\;, \tag{4.36}$$

with $\langle\delta\hat{n}(t)\rangle=0$. In the previous section, we saw that the PSD of the classical current constructed by measurements can be linked to the symmetrised PSD of the intensity operator as given in equation (4.26). The symmetrised PSD of the noisy intensity operator is

$$\overline{S}_{\delta\hat{n}}(\omega) \;=\; \frac{1}{2}\left(S_{\delta\hat{n}}(\omega)+S_{\delta\hat{n}}(-\omega)\right)\;. \tag{4.37}$$

In an experiment, we measure the photocurrent at the photodiode and then calculate its power spectrum. The important results of this section showed that this power spectrum can be related to the symmetrised power spectrum of the photon flux. Knowing what the photon flux operator is, lets us calculate its symmetrised power spectrum, which will give us insights on the information that we can experimentally extract from the signal. In the following, we will briefly introduce some fundamental detection schemes and then go into the detailed modelling of the BEC and superfluid Helium setup.

4.1.3 Detection Schemes

Before going into the details of the explicit proposals on how to detect the Unruh effect in various systems, we quickly want to give an overview of reoccurring ideas throughout this chapter. That is, we want to discuss the different detection methods such as direct detection, homodyning and heterodyning 4.3. For a conceptual discussion, we use a single-mode analysis in this section.

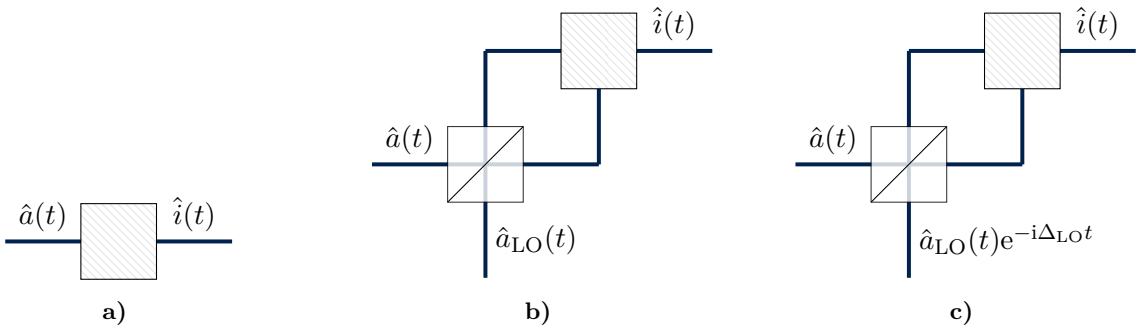

Figure 4.3 a) Direct detection of incoming annihilation operator $\hat{a}(t)$, b) homodyning method with local oscillator $\hat{a}_{\mathrm{LO}}(t)$ entering a beam splitter and being recombined in some kind of detection scheme (shaded area) to the outgoing number operator $\hat{i}(t)$. c) Heterodyning detection scheme.

The direct detection consists of a device directly measuring incoming photo counts (see figure 4.3a). The photo counts as expressed by creation and annihilation operators has been discussed previously and is simply given by the number operator $\hat{n}(t) = \hat{a}^\dagger(t)\hat{a}(t)$.

The other two methods make use of a beam splitter which transforms most generally ingoing annihilation operators $\hat{a}_1$ and $\hat{a}_2$ with a transformation matrix $(B)_{ij}$. The outgoing annihilation operators are $\hat{b}_1$ and $\hat{b}_2$ such that

$$\begin{pmatrix} \hat{b}_1 \\ \hat{b}_2 \end{pmatrix} = \begin{pmatrix} B_{11} & B_{12} \\ B_{21} & B_{22} \end{pmatrix} \begin{pmatrix} \hat{a}_1 \\ \hat{a}_2 \end{pmatrix} . \tag{4.38}$$

The outgoing operators $\hat{b}_i$, $i \in \{1, 2\}$ have to fulfil the same bosonic commutation relations as the ingoing operators

$$\left[\hat{b}_i, \hat{b}_j\right] = \left[\hat{b}_i^\dagger, \hat{b}_j^\dagger\right] = 0, \tag{4.39a}$$

$$\left[\hat{b}_i, \hat{b}_j^\dagger\right] = \delta_{ij}. \tag{4.39b}$$

These commutation relations impose conditions on the matrix elements of B and show that $B \in \mathrm{U}(2)$. Solving these equations for the matrix elements of B, we see that any B can be written in terms of three independent parameters, the transmission coefficient τ, reflection coefficient $\rho = 1 - \tau$ and respective phases Φ_τ and Φ_ρ [120]. In the following, we assume a lossless, symmetric beam splitter with $\tau = \rho = 1/2$. In the following, we will use beam splitters as given by $B^{(1)}$ and omit the superscript

$$B^{(1)} \;=\; \frac{1}{\sqrt{2}}\begin{pmatrix} 1 & -1 \\ 1 & 1 \end{pmatrix} \quad \text{for } \Phi_\tau = 2\pi\mathbb{Z}, \Phi_\rho = (2\mathbb{Z}+1)\pi \; . \tag{4.40}$$

In the homodyne detection method, the optical field $\hat{a}(t)$ to be detected is being interfered with a local oscillator $\hat{a}_{\mathrm{LO}}(t)$ (figure 4.3), using a beam splitter. The output operators of the beam splitter are

$$\hat{a}_\pm(t) \;=\; \frac{1}{\sqrt{2}}\left(\hat{a}_{\mathrm{LO}}(t) \pm \hat{a}(t)\right) \; . \tag{4.41}$$

These outputs are independently detected by two photodiodes. The corresponding number operators of the photon flux are given by

$$\hat{n}_\pm \;=\; \hat{a}_\pm^\dagger \hat{a}_\pm \; . \tag{4.42}$$

The difference photocurrent is given by

$$\hat{i}(t) \;=\; \hat{n}_+(t) - \hat{n}_-(t) \;=\; \hat{a}_{\mathrm{LO}}^\dagger \hat{a} + \hat{a}_{\mathrm{LO}} \hat{a}^\dagger \; . \tag{4.43}$$

If the local oscillator is much brighter then the detectable signal, i.e. $|\alpha_{\mathrm{LO}}| = |\langle \hat{a}_{\mathrm{LO}}(t) \rangle| \gg |\langle \hat{a}(t) \rangle|$, then we can treat the local oscillator classically. In that case the homodyne difference photocurrent becomes

$$\hat{i}(t) \;=\; \alpha_{\mathrm{LO}}^* \hat{a} + \alpha_{\mathrm{LO}} \hat{a}^\dagger \;=:\; |\alpha_{\mathrm{LO}}| \hat{a}^\theta(t) \; , \tag{4.44}$$

with $\alpha_{\mathrm{LO}} = |\alpha_{\mathrm{LO}}| \mathrm{e}^{\mathrm{i}\theta}$. Lastly, the heterodyne detection method is in essence the same as the homodyne detection method, however, the frequency of the local oscillator is offset from the field to be detected by some detuning $\Delta_{\mathrm{LO}} = \Omega_{\mathrm{LO}} - \Omega_L$. The detected difference photocurrent is

$$\hat{i}(t) \;=\; \alpha_{\mathrm{LO}}^* \hat{a} \mathrm{e}^{\mathrm{i}\Delta_{\mathrm{LO}} t} + \alpha_{\mathrm{LO}} \hat{a}^\dagger \mathrm{e}^{-\mathrm{i}\Delta_{\mathrm{LO}} t} \;=\; |\alpha_{\mathrm{LO}}| \hat{a}^{\theta - \Delta_{\mathrm{LO}} t}(t) \; . \tag{4.45}$$

The quadrature of the detected field thus oscillates with a phase given by the detuning of the local oscillator. In this section, we introduced three common concepts of detection schemes and in the next section, we will use the direction detection in the BEC setup and the homodyne detection method in superfluid Helium.

4.2 Detectability of the Unruh Effect in BECs

Now that we developed the framework of classical and quantum mechanical photodetection, we can turn our attention to the detection schemes of the Unruh effect in BECs and later in superfluid Helium. This chapter outlines the transformation on the operators of the electromagnetic field as it interacts with the components of the experiment as proposed in figure 3.3. Eventually, this allows us to write down a photon flux operator as it is detected at the photodiode. Using the photodetection framework, we can calculate what the detected signal in an experiment would be and how to extract the Unruh signal from it. The BEC setup in figure 3.3 can be represented in a more abstract way as spacetime diagram, given in figure 4.4.

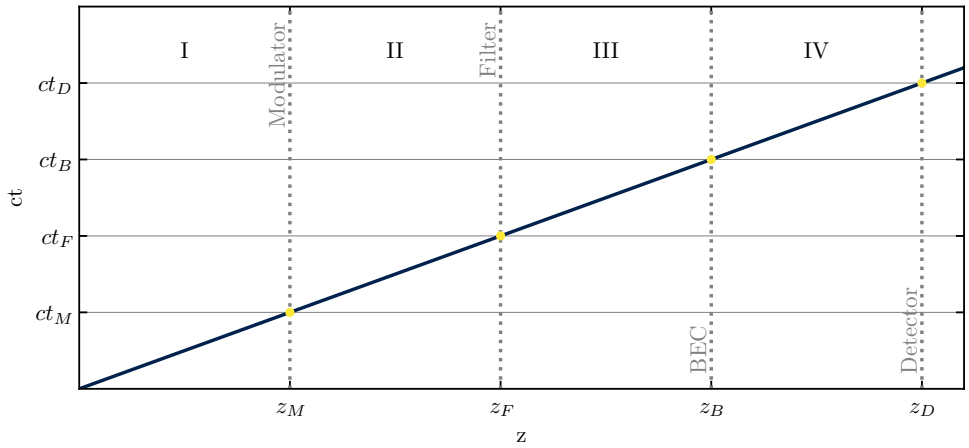

Figure 4.4 (Spacetime Diagram) Diagram for detection scheme in figure 3.3. Modulator located at (z_M, ct_M), filter at (z_F, ct_F), BEC at (z_B, ct_B) and detector at (z_D, ct_D). For future reference, each region with a specific mode content is labelled with Roman numbers I-IV.

The following paragraphs describe how the electromagnetic field operators transform in each step. We go through the field content in every region of the spacetime diagram 4.4. In particular, we see how the modulated sidebands helps us extract the signal of the Unruh effect.

I - Incoming Field. The incoming electric field is given by

$$\hat{E}(t,z) \;=\; \int_0^\infty \frac{\mathrm{d}\omega}{2\pi}\, E_0(\omega)\hat{a}_\omega \mathrm{e}^{-\mathrm{i}\omega(t-z)} + h.c.\,, \tag{4.46}$$

with $E_0(\omega) = \left(\frac{\hbar\omega}{A_\perp \epsilon_0 c}\right)^{1/2}$. This is the form of an electromagnetic field propagating in just one direction with only one polarisation as it has been shown in (3.6). In the same manner as the ansatz in section 3.1, the incoming field is now modelled as a macroscopically occupied mode with frequency ω_L and amplitude $\alpha \in \mathbb{C}$ [121]

$$\hat{a}_\omega \;=\; \alpha\, \delta(\omega - \omega_L) + \delta\hat{a}_{\omega-\omega_L}\,, \tag{4.47}$$

with $[\delta\hat{a}_{\omega}, \delta\hat{a}^{\dagger}_{\omega'}] = \delta(\omega - \omega')$. This expresses the annihilation operator as a central carrier frequency and perturbations about this frequency or, in other words, a macroscopical, classical background with (quantum) fluctuations. Thus, we can write (using $u = t - z$)

$$\hat{E}(u) = E_0(\omega_L)\alpha e^{-i\omega_L u} + \int_{\omega_L-\Lambda}^{\omega_L+\Lambda} \frac{d\omega}{2\pi} E_0(\omega)\delta\hat{a}_{\omega-\omega_L} e^{-i\omega u} + h.c. \tag{4.48a}$$

$$\equiv E_0(\omega_L)e^{-i\omega_L u}(\alpha + \delta\hat{a}(u)) + h.c. \tag{4.48b}$$

where in the last line, we used $E(\omega_L + \delta\omega) \approx E(\omega_L)$, and we identified the integral as the Fourier representation of $\delta\hat{a}(u)$. Note that the operators $\delta\hat{a}$ obey the usual bosonic commutation relations

$$[\delta\hat{a}(t), \delta\hat{a}(t')] = \left[\delta\hat{a}^{\dagger}(t), \delta\hat{a}^{\dagger}(t')\right] = 0\,, \tag{4.49a}$$

$$\left[\delta\hat{a}(t), \delta\hat{a}^{\dagger}(t')\right] = 2\pi\delta(t - t')\,. \tag{4.49b}$$

II - Modulation. The next step in figure 4.4 is to modulate the field with frequency ω_m. Mathematically, this modulation is simply a transformation $\hat{E}(u) \to \hat{E}(u)\exp\{iM\cos\omega_m(u - u_m)\}$, $u_m = t_m - z_m$ being the position of the modulator. For a small modulation index M, the exponential can be expanded up to linear order in M,

$$\hat{E}(u) \to \hat{E}(u)\left(1 + \frac{iM}{2}\left(e^{i\omega_m(u-u_m)} + e^{-i\omega_m(u-u_m)}\right)\right)\,, \tag{4.50}$$

where we have written the cosine as exponentials. Using the expression for $\hat{E}(u)$ from above, this transformation can be rewritten as a transformation on the coherent amplitude and fluctuation operators. We see that the coherent amplitude α transforms as

$$\alpha \to \alpha(u) = \alpha + \alpha_+ e^{-i\omega_m u} + \alpha_- e^{i\omega_m u}\,, \tag{4.51}$$

where we defined $\alpha_{\pm} = \frac{iM\alpha}{2}e^{\pm i\omega_m u_m} = \frac{M\alpha}{2}e^{i(\pi\pm\omega_m u_m)}$ with $|\alpha_+| = |\alpha_-|$. We find similar transformations for the operators $\delta\hat{a}$

$$\delta\hat{a}(u) \to \delta\hat{a}(u) + \delta\hat{a}_+(u)e^{-i\omega_m u} + \delta\hat{a}_-(u)e^{i\omega_m u}\,, \tag{4.52}$$

with $\delta\hat{a}_{\pm}(u) = \frac{iM\delta\hat{a}^{(\pm)}(u)}{2}e^{\pm i\omega_m u_m}$. This modulation creates the two desired sidebands with frequencies $\omega_L \pm \omega_m$.

A note on sideband operators $\delta\hat{a}^{(\pm)}$. Note, how we defined the operators before the modulation in equation (4.48)

$$\delta\hat{a}(u) = \int_{-\Lambda}^{\Lambda} \frac{d\nu}{2\pi}\,\delta\hat{a}_\nu e^{-i\nu u} \tag{4.53}$$

with $\nu = \omega - \omega_L$. The mode operators $\delta\hat{a}_\nu$ describe fluctuations around the central laser frequency. Equivalently, the operators $\delta\hat{a}_{\nu,\pm}$ in the Fourier representation of $\delta\hat{a}^{(\pm)}|(u)$ describe fluctuations around the side band frequencies. These are operators of the same electromagnetic field, however, at different frequencies $\omega_L \pm \omega_m + \nu$. The sideband operators obey the

commutation relations

$$\left[\delta\hat{a}_{\pm}(u), \delta\hat{a}_{\pm}(u')\right] = \left[\delta\hat{a}^{\dagger}_{\pm}(u), \delta\hat{a}^{\dagger}_{\pm}(u')\right] = 0 \,, \tag{4.54a}$$

$$\left[\delta\hat{a}_{\pm}(u), \delta\hat{a}^{\dagger}_{\pm}(u')\right] = \frac{\pi M^2}{2}\delta(u-u') \,. \tag{4.54b}$$

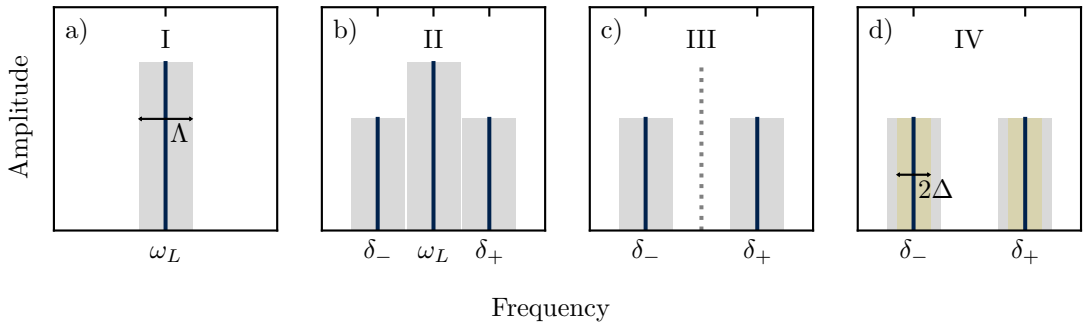

Figure 4.5 (Frequency Content) Modulation and filtering process with blue lines corresponding to macroscopically occupied frequencies and grey area indicating frequency range of noise. a) initial electromagnetic field with macroscopic single mode occupation with frequency ω_L corresponding to region I, b) Modulator, sideband modulation with modulation frequency ω_M and detuning $\delta_\pm = \omega_L \pm \omega_M$ corresponding to region II, c) Filter, filtering of carrier frequency corresponding to region III.

III - Central Frequency Filtering. All the transformations so far happen to a coherent input state with frequency ω_L. The modulation creates two sidebands with frequencies $\omega_L \pm \omega_M$ as can be seen from the transformations above. In consequence, the only term propagating with the original input frequency is the first term of equations (4.51) and (4.52). In the next step, this central frequency ω_L is being filtered out resulting in

$$\alpha(u) \;\rightarrow\; \alpha(u) = \mathrm{e}^{-\mathrm{i}\omega_m u}\alpha_+ + \mathrm{e}^{\mathrm{i}\omega_m u}\alpha_- \,, \tag{4.55a}$$

$$\delta\hat{a}(u) \;\rightarrow\; \delta\hat{a}(u) = \mathrm{e}^{-\mathrm{i}\omega_m u}\delta\hat{a}_+(u) + \mathrm{e}^{\mathrm{i}\omega_m u}\delta\hat{a}_-(u) \,. \tag{4.55b}$$

After this filtering process we may want to write the operators of the electromagnetic field as

$$\hat{a}_{\pm} = \mathrm{e}^{\pm\mathrm{i}\omega_m u}\left(\alpha_{\pm} + \delta\hat{a}_{\pm}\right) \,, \tag{4.56}$$

which show that the electromagnetic field consists of two macroscopically occupied modes at frequencies $\omega_L \pm \omega_M$ and fluctuations of a certain frequency range around it.

We can now introduce the common and difference modes using the phase shifted operators

$e^{\mp i\omega_m u_m}\delta\hat{a}_\pm$ and the sideband operators after the latest transformation (4.55b)

$$\hat{z}(u) = \frac{1}{\sqrt{2}}\left(e^{-i\omega_m u_m}\delta\hat{a}_+(u) + e^{i\omega_m u_m}\delta\hat{a}_-(u)\right) , \tag{4.57a}$$

$$\hat{Z}(u) = \frac{1}{\sqrt{2}}\left(e^{-i\omega_m u_m}\delta\hat{a}_+(u) - e^{i\omega_m u_m}\delta\hat{a}_-(u)\right) . \tag{4.57b}$$

Note again, that $\delta\hat{a}_\pm(u)$ contain operators at different frequencies.

This transformation can be inverted to find

$$\delta\hat{a}_\pm(u) = \frac{1}{\sqrt{2}}e^{\pm i\omega_m u_m}\left(z(u)\right) \pm Z(u)) , \tag{4.58}$$

which can be used to represent the operator after the transformation in equation (4.55b)

$$\delta\hat{a}(u) = \sqrt{2}\cos\left(\omega_m(u+u_m)\right)\hat{z}(u) + i\sqrt{2}\sin\left(\omega_m(u+u_m)\right)\hat{Z}(u) . \tag{4.59}$$

This definition is useful as these operators have a particularly convenient transformation under the interaction with the BEC.

IV - Interaction with BEC. In equation (3.62) of the previous chapter we saw how the BEC interacts with the laser. The density fluctuations are dumped into the laser phase fluctuations. Thus, we can write this interaction as a transformation on the operators before the BEC interaction

$$\hat{a}_\pm(u) \rightarrow \hat{a}_\pm(u) = e^{\mp i\frac{\epsilon}{2}\delta\rho(u)}\left(\alpha_\pm + \delta\hat{a}_\pm(u)\right) , \tag{4.60}$$

where $\delta\rho(u) \equiv \delta\rho\left(t-|z|, \boldsymbol{X}(t-|z|)\right)$ are the density perturbations coming from the position $\boldsymbol{X}(t)$ in the BEC plane. This is a transformation corresponding to the solution of the equation of motion for the laser phase fluctuations as shown in (3.62). This solution tells us that the BEC density fluctuations transduce into the phase of the electric field. Equivalently, this can be written as an additional phase of the annihilation operator as shown above. A quick remark on the sign of $\delta\hat{\rho}$. From the discussion of the polarisability we have seen that the sign for each side band is the opposite. The solution to the equation of motion tells us that the phase shift is positive for positive frequency modulation and negative for negative frequency modulation.

The transformation above can be expanded for small ϵ up to linear order where we omit the negligible product of $\epsilon\delta\rho\delta\hat{a}$. After some rearrangement we obtain

$$\hat{a}_\pm(u) \rightarrow \alpha_\pm + \delta\hat{a}_\pm(u) \mp i\frac{\epsilon}{2}\alpha_\pm\delta\rho(u) , \tag{4.61}$$

from which we can see that the interaction with the BEC is essentially a transformation on $\delta\hat{a}_\pm(u)$ with

$$\delta\hat{a}_\pm(u) \rightarrow \delta\hat{a}_\pm(u) \mp i\frac{\epsilon}{2}\alpha_\pm\delta\rho(u) . \tag{4.62}$$

This is a result as expected from the conceptual discussion of this setup. The solution to the semi classical ansatz of perturbations about a background showed that the BEC density fluctuations contribute to the fluctuation content, which is exactly what we use in the transformation on operator level above. The beauty of those phase shifted common and difference operators in

equation (4.57) is their transformation behaviour according to equation (4.62)

$$\hat{z}(u) \;\to\; \hat{z}(u)\,, \tag{4.63a}$$

$$\hat{Z}(u) \;\to\; \hat{Z}(u) + \frac{\epsilon}{\sqrt{2}}\frac{M\alpha}{2}\delta\rho(u)\,. \tag{4.63b}$$

This shows that

$$\delta\hat{a}(u) \;\to\; \sqrt{2}\cos\left(\omega_m(u+u_m)\right)\hat{z}(u) + \mathrm{i}\sqrt{2}\sin\left(\omega_m(u+u_m)\right)\hat{Z}(u) + \mathrm{i}\frac{\epsilon}{2}M\alpha\sin\left(\omega_m(u+u_m)\right)\delta\hat{\rho}(u)\,. \tag{4.64}$$

Remember, that the interaction with the BEC is just a transformation on $\delta\hat{a}$, such that the coherent amplitudes are still given by equation (4.47). As seen in (3.48), we can write the BEC field as a mode expansion

$$\delta\rho(u) \;=\; \int_0^\Delta \frac{\mathrm{d}\nu}{2\pi}\left(\mathrm{e}^{-\mathrm{i}\nu u}\hat{D}_\nu + \mathrm{e}^{\mathrm{i}\nu u}\hat{D}_\nu^\dagger\right) \tag{4.65a}$$

$$\;=\; \int_{-\Delta}^\Delta \frac{\mathrm{d}\nu}{2\pi}\,\mathrm{e}^{-\mathrm{i}\nu u}\left(\hat{D}_\nu\Theta(\nu) + \hat{D}_{-\nu}^\dagger\Theta(-\nu)\right)\,. \tag{4.65b}$$

as well as the sideband operators

$$\delta\hat{a}_\pm(u) \;=\; \int_{-\Lambda}^{\Lambda}\mathrm{d}\nu\;\mathrm{e}^{-\mathrm{i}\nu u}\delta\hat{a}_{\nu,\pm}\,. \tag{4.66}$$

Here, bear in mind that only the time dependence is shown as the BEC density field is evaluated at the point of interaction and then detected at the photodiode. Any normalisation factor appearing in (3.48) has been absorbed into the definition of $\hat{D}_\nu$. Similarly to the definitions above, we define the operators $\hat{Z}_\nu$ in momentum space, however, note that this operator contains annihilation operators from each sideband. Using the spectral decomposition for each respective operator we see that for $\nu > 0$

$$\hat{Z}_\nu \;\to\; \hat{Z}_\nu + \mathrm{i}\mu\mathrm{e}^{\mathrm{i}\varphi}\hat{D}_\nu\,, \tag{4.67a}$$

$$\hat{Z}_{-\nu} \;\to\; \hat{Z}_{-\nu} + \mathrm{i}\mu\mathrm{e}^{\mathrm{i}\varphi}\hat{D}_{-\nu}^\dagger\,, \tag{4.67b}$$

where for brevity we have defined $\mu = -\frac{\epsilon}{\sqrt{2}}\frac{M|\alpha|}{2} \in \mathbb{R}$ with φ being the phase of $\mathrm{i}\alpha$.

Bogoliubov Transformation. The operators after the interaction have to obey well defined bosonic commutation relations. This may not be satisfied if one considers the transformation only up to order μ, as we did above. In the following, we want to derive a transformation operation for the interaction with the BEC that fully retrieves the bosonic commutation relations. More general, we can express the transformation above as Bogoliubov transformation such that for any operator $\hat{X}_i \in \left\{\hat{Z}_\nu, \hat{Z}_{-\nu}, \hat{D}_\nu\right\}$ we find

$$\widetilde{X}_i \;=\; \alpha_{ij}\hat{X}_j + \beta_{ij}\hat{X}_j^\dagger\,, \tag{4.68}$$

where the tilde indicates operators after the interaction with the BEC and summation over repeated indices is implied. After all, the transformed operators still have to obey the usual commutation relations, i.e. $\left[\tilde{X}_i, \tilde{X}_j\right] = 0$ and $\left[\tilde{X}_i, \tilde{X}_j^\dagger\right] = \delta_{ij}$. These commutation relations impose the conditions

$$\alpha_{ik}\beta_{jk} - \beta_{ik}\alpha_{jk} = 0 \,, \tag{4.69a}$$
$$\alpha_{ik}\alpha_{jk}^* - \beta_{ik}\beta_{jk}^* = \delta_{ij} \,. \tag{4.69b}$$

Equations (4.67) suggest that to lowest order we can write $\alpha_{ij} = \delta_{ij} + \delta\alpha_{ij}$ and $\beta_{ij} = \delta\beta_{ij}$ for which the conditions in equations (4.69) yield

$$\delta\beta_{ji} = \delta\beta_{ij} \,, \tag{4.70a}$$
$$\delta\alpha_{ij} = -\delta\alpha_{ji}^* \,. \tag{4.70b}$$

For the sake of this discussion, let us absorb the phase φ appearing in (4.67) into the operators $\hat{Z}$. Comparing (4.67) with the expression above we find $\delta\alpha_{13} = -\delta\alpha_{31}^* = \mathrm{i}\mu$ and $\delta\beta_{23} = \delta\beta_{32} = \mathrm{i}\mu$. Consequently, the BEC operators transform like [122]

$$\hat{D}_\nu \;\to\; \hat{D}_\nu + \mathrm{i}\mu\left(\hat{Z}_\nu + \hat{Z}_{-\nu}^\dagger\right) \,. \tag{4.71}$$

Furthermore, we can write this Bogoliubov transformation in matrix form

$$\begin{pmatrix} \tilde{X}_i \\ \tilde{X}_k^\dagger \end{pmatrix} = \begin{pmatrix} \alpha_{ij} & \beta_{il} \\ \beta_{ki}^* & \alpha_{kl}^* \end{pmatrix} \begin{pmatrix} \hat{X}_i \\ \hat{X}_l^\dagger \end{pmatrix} \,, \tag{4.72}$$

which to lowest order in μ can be written as

$$\begin{pmatrix} \tilde{X}_i \\ \tilde{X}_k^\dagger \end{pmatrix} = \left[\begin{pmatrix} \delta_{ij} & 0 \\ 0 & \delta_{kl} \end{pmatrix} + \begin{pmatrix} \delta\alpha_{ij} & \delta\beta_{il} \\ \delta\beta_{ki}^* & \delta\alpha_{kl}^* \end{pmatrix}\right] \begin{pmatrix} \hat{X}_i \\ \hat{X}_l^\dagger \end{pmatrix} \,, \tag{4.73}$$

using the delta expressions as before. As can be seen from the explicit transformation, the matrix containing all the deltas is proportional to μ such that

$$\frac{\mathrm{d}}{\mathrm{d}\mu}\begin{pmatrix} \tilde{X}_i \\ \tilde{X}_k^\dagger \end{pmatrix} = \mathcal{M}\begin{pmatrix} \tilde{X}_i \\ \tilde{X}_k^\dagger \end{pmatrix}\Bigg|_{\mu=0} \,, \tag{4.74}$$

with $\mathcal{M}$ being the derivative with respect to μ of the delta matrix above. The equation can be extended to a differential equation $\frac{\mathrm{d}}{\mathrm{d}\mu}\tilde{U} = \mathcal{M}\tilde{U}$ and easily solved with an exponential function. More explicitly, we find

$$\begin{pmatrix} \tilde{X}_i \\ \tilde{X}_k^\dagger \end{pmatrix} = \left[\mathbb{I} + \mu\mathcal{M} + \frac{1}{2}\mu^2\mathcal{M}^2\right] \begin{pmatrix} \hat{X}_i \\ \hat{X}_l^\dagger \end{pmatrix} \,, \tag{4.75}$$

where the the key of this approach is that $\mathcal{M}^3 = 0$, which means the Taylor expansion of the exponential has a finite amount of elements. More specifically, any order in μ higher than 2 vanishes. We show the explicit form of $\mathcal{M}$ in appendix B.3. We obtain the following transformation

valid to all orders in μ

$$\hat{Z}_\nu \;\to\; \left(1-\frac{\mu^2}{2}\right)\hat{Z}_\nu + \mathrm{i}\mu \mathrm{e}^{\mathrm{i}\varphi}\hat{D}_\nu - \frac{\mu^2}{2}\mathrm{e}^{2\mathrm{i}\varphi}\hat{Z}^\dagger_{-\nu}\,, \tag{4.76a}$$

$$\hat{Z}_{-\nu} \;\to\; \left(1+\frac{\mu^2}{2}\right)\hat{Z}_{-\nu} + \mathrm{i}\mu \mathrm{e}^{\mathrm{i}\varphi}\hat{D}^\dagger_\nu + \frac{\mu^2}{2}\mathrm{e}^{2\mathrm{i}\varphi}\hat{Z}^\dagger_{\nu}\,, \tag{4.76b}$$

$$\hat{D}_\nu \;\to\; \hat{D}_\nu + \mathrm{i}\mu\left(\mathrm{e}^{-\mathrm{i}\varphi}\hat{Z}_\nu + \mathrm{e}^{\mathrm{i}\varphi}\hat{Z}^\dagger_{-\nu}\right)\,. \tag{4.76c}$$

These transformations show an important result of the two sideband setup and why this setup acts as an interferometer in frequency space – the interaction de-amplifies the modes $\hat{Z}_\nu$ and amplifies the modes $\hat{Z}_{-\nu}$! In contrast, the BEC modes are neither amplified nor de-amplified. In addition, we see that there is additional noise injected into each of those operators.

In a last step, let us define a set of new operators

$$\hat{Z}^\varphi_\nu \;=\; \frac{1}{\sqrt{2}}\left(\mathrm{e}^{-\mathrm{i}\varphi}\hat{Z}_\nu + \mathrm{e}^{\mathrm{i}\varphi}\hat{Z}^\dagger_{-\nu}\right)\,. \tag{4.77}$$

Rewriting the Bogoliubov transformations in terms of this new operator, we find

$$\hat{Z}_\nu \;\to\; \hat{Z}_\nu + \mathrm{i}\mu\mathrm{e}^{\mathrm{i}\varphi}\hat{D}_\nu - \frac{\mu^2}{\sqrt{2}}\mathrm{e}^{\mathrm{i}\varphi}\hat{Z}^\varphi_\nu\,, \tag{4.78a}$$

$$\hat{Z}_{-\nu} \;\to\; \hat{Z}_{-\nu} + \mathrm{i}\mu\mathrm{e}^{\mathrm{i}\varphi}\hat{D}^\dagger_\nu + \frac{\mu^2}{\sqrt{2}}\mathrm{e}^{\mathrm{i}\varphi}\hat{Z}^\varphi_{-\nu}\,, \tag{4.78b}$$

$$\hat{D}_\nu \;\to\; \hat{D}_\nu + \sqrt{2}\mathrm{i}\mu\hat{Z}^\varphi_\nu\,. \tag{4.78c}$$

This transformation can be expressed in real space as

$$\hat{Z}(u) \;\to\; \hat{Z}(u) + \mathrm{i}\mu\mathrm{e}^{\mathrm{i}\varphi}\delta\hat{\rho}(u) - \frac{\mu^2}{\sqrt{2}}\mathrm{e}^{\mathrm{i}\varphi}\int_{-\Delta}^{\Delta}\frac{\mathrm{d}\nu}{2\pi}\,\mathrm{e}^{-\mathrm{i}\nu u}\hat{Z}^\varphi_\nu(u)\,\mathrm{sgn}(u)\,, \tag{4.79}$$

and shows how the difference mode transforms under the interaction with the BEC. In equation (4.59), we expressed the annihilation operator in terms of $\hat{z}$ and $\hat{Z}$. Since we now know how these operators transform, we know how the original annihilation operators transform. According to the transformation above, the fluctuations in the electromagnetic field have a shot noise contribution (sn), a BEC contribution (bec) and a back-action contribution (ba), such that (using (4.59) and (4.78))

$$\delta\hat{a}(u) \;\to\; \delta\hat{a}_{\mathrm{sn}}(u) + \delta\hat{a}_{\mathrm{bec}}(u) + \delta\hat{a}_{\mathrm{ba}}(u)\,, \tag{4.80}$$

with

$$\delta\hat{a}_{\mathrm{sn}}(u) \;=\; \sqrt{2}\cos\left(\omega_m(u+u_m)\right)\hat{z}(u) + \mathrm{i}\sqrt{2}\sin\left(\omega_m(u+u_m)\right)\hat{Z}(u)\,, \tag{4.81a}$$

$$\delta\hat{a}_{\mathrm{bec}}(u) \;=\; -\sqrt{2}\mu\sin\left(\omega_m(u+u_m)\right)\mathrm{e}^{\mathrm{i}\varphi}\delta\hat{\rho}(u)\,, \tag{4.81b}$$

$$\delta\hat{a}_{\mathrm{ba}}(u) \;=\; -\mathrm{i}\mu^2\sin\left(\omega_m(u+u_m)\right)\mathrm{e}^{\mathrm{i}\varphi}\int_{-\Delta}^{\Delta}\frac{\mathrm{d}\nu}{2\pi}\,\mathrm{e}^{-\mathrm{i}\nu u}\hat{Z}^\varphi_\nu(u)\,\mathrm{sgn}(u)\,. \tag{4.81c}$$

Summary - Input/Output. In this section, we saw how the initial electromagnetic field transformed in our proposed BEC detection scheme. We have outlined how the field operators transform in each step and found that we can express the electromagnetic field after its interaction with the BEC as a coherent amplitude given by (see equation (4.55a))

$$\alpha(u) \;=\; \mathrm{i}M\alpha\cos\left(\omega_m(u+u_M)\right)\;, \tag{4.82}$$

and fluctuations about the carrier frequencies of the two sidebands (4.81).

This final expression for the operators of the electromagnetic field allows us to calculate the photon flux at the photodiode. As mentioned in the beginning of this chapter, the power spectral density of the photon flux can then be related to the power spectrum of the measured photocurrent of the photodiode. In the next section, we combine the results of the explicit photodetector model and this detection scheme to derive an expression for the PSD and how the BEC correlations can be extracted to measure the Unruh effect.

Detection. The laser is directly detected with a single photodiode (see direct detection in section 4.1.3). In this section, we will first look at the explicit form of the number operator based on the transformations in the previous section and then construct the PSD of the photon flux. Finally, we show how to extract the Unruh effect signal from the photocurrent PSD. The frequency structure of the modes in the electromagnetic field after the interaction with the BEC is represented in figure 4.5 (d), i.e. two carrier frequencies at $\omega_L \pm \omega_m$, shot noise at $\omega_L \pm \omega_m \pm \Lambda$ and BEC density fluctuations at $\omega_L \pm \omega_m \pm \Delta$. In addition, those frequencies obey the scale $\omega_L \gg \omega_m \gg \Delta$.

As shown in equation (4.34), the number operator for a coherent electromagnetic field can be expressed as a contribution from the coherent carrier frequencies (using equation (4.82))

$$\langle\hat{n}\rangle \;=\; |\alpha(u)|^2 \;=\; M^2|\alpha|^2\cos^2\left(\omega_m(u+u_M)\right)\;, \tag{4.83}$$

and fluctuations about this coherent background

$$\delta\hat{n}(u) \;=\; M|\alpha|\cos\left(\omega_m(u+u_M)\right)\delta\hat{a}^{\varphi}(u)\;, \tag{4.84}$$

where $\delta\hat{a}^{\varphi}(u)$ as defined in equation (4.35) is the rotated operator of all fluctuations (4.81). We saw that the fluctuations operator contains several contributions from different operators, whose rotated operators are given by

$$\begin{aligned}
\delta\hat{a}^{\varphi}_{\mathrm{sn}}(u) \;&=\; \sqrt{2}\cos\left(\omega_m(u+u_m)\right)\hat{z}^{\varphi}(u) \\
&\quad + \mathrm{i}\sqrt{2}\sin\left(\omega_m(u+u_m)\right)\left(\mathrm{e}^{-\mathrm{i}\varphi}\hat{Z}(u) - \mathrm{e}^{\mathrm{i}\varphi}\hat{Z}^{\dagger}(u)\right)\;, && \text{(4.85a)}\\
\delta\hat{a}^{\varphi}_{\mathrm{bec}}(u) \;&=\; -2\sqrt{2}\mu\sin\left(\omega_m(u+u_m)\right)\delta\hat{\rho}(u)\;, && \text{(4.85b)}\\
\delta\hat{a}^{\varphi}_{\mathrm{ba}}(u) \;&=\; -2\mathrm{i}\mu^2\sin\left(\omega_m(u+u_m)\right)\int_{-\Delta}^{\Delta}\frac{\mathrm{d}\nu}{2\pi}\,\mathrm{e}^{-\mathrm{i}\nu u}\left(\mathrm{e}^{-\mathrm{i}\varphi}\hat{Z}_{\nu}(u) - \mathrm{e}^{\mathrm{i}\varphi}\hat{Z}^{\dagger}_{\nu}\right)\mathrm{sgn}(\nu)\;. && \text{(4.85c)}
\end{aligned}$$

The first expression are the non-interacting shot noise fluctuations, leading to fluctuations in

the photon flux[2]

$$\delta\hat{n}_{\mathrm{sn}}(u) \;=\; M|\alpha|\sqrt{2}\cos^2\left(\omega_m(u+u_m)\right)\hat{z}^{\varphi}(u)+ \\ \frac{M|\alpha|}{\sqrt{2}}\mathrm{i}\sin\left(2\omega_m(u+u_m)\right)\left(\mathrm{e}^{-\mathrm{i}\varphi}\hat{Z}(u)-\mathrm{e}^{\mathrm{i}\varphi}\hat{Z}^{\dagger}(u)\right)\;. \quad (4.86)$$

Accordingly, we find for the BEC contribution in the photon flux

$$\delta\hat{n}_{\mathrm{bec}}(u) \;=\; -\sqrt{2}M|\alpha|\mu\sin\left(2\omega_m(u+u_m)\right)\delta\hat{\rho}(u)\;, \quad (4.87)$$

and for the back-action contribution

$$\delta\hat{n}_{\mathrm{ba}}(u) \;=\; -\mathrm{i}\mu^2 M|\alpha|\sin\left(2\omega_m(u+u_m)\right)\int_{-\Delta}^{\Delta}\frac{\mathrm{d}\nu}{2\pi}\,\mathrm{e}^{-\mathrm{i}\nu u}\left(\mathrm{e}^{-\mathrm{i}\varphi}\hat{Z}_{\nu}(u)-\mathrm{e}^{\mathrm{i}\varphi}\hat{Z}_{\nu}^{\dagger}\right)\mathrm{sgn}(\nu)\;. \quad (4.88)$$

The classical photocurrent detected at the photodiode therefore also contains contributions of each of those fluctuations. By measuring correlations in the classical photocurrent the question naturally arises what we can extract about correlations in the BEC density field, which is the interesting part for the Unruh effect. In the beginning of this chapter, we already saw that the power spectral density of a noisy operator is simply the PSD of collective fluctuations. As the fluctuations are composed of different constituents, the PSD of photon flux fluctuations will be the sum of PSDs of all possible combinations of those constituents.

First, let us focus on the most interesting part, the BEC density correlations in the power spectrum. From equation (4.87) we can tell that the BEC signal appears at frequencies $\omega \in [2\omega_m-\Delta, 2\omega_m+\Delta]$ at order μ^2 in the PSD. The PSD of density fluctuations in the photon flux is given by

$$S_{\mathrm{bec}}(\omega) \;=\; \int_{-\infty}^{\infty}\mathrm{d}t\;\mathrm{e}^{\mathrm{i}\omega u}\left\langle\delta\hat{n}_{\delta\rho}^{\dagger}(u)\delta\hat{n}_{\delta\rho}(0)\right\rangle\;. \quad (4.89)$$

Using equation (4.87), we find for the PSD at frequencies $2\omega_m+\nu$

$$S_{\mathrm{bec}}(2\omega_m+\nu) \;=\; -2\mathrm{i}M^2|\alpha|^2\mu^2\sin(2\omega_m u_m)\mathrm{e}^{\mathrm{i}2\omega_m u_m}S_{\delta\rho}(\nu)\;, \quad (4.90)$$

where $S_{\delta\rho}(\nu)$ is the PSD of the operator $\delta\hat{\rho}$. Subsequently, the symmetrised PSD is

$$\overline{S}_{\mathrm{bec}}(2\omega_m+\nu) \;=\; -\mathrm{i}M^2|\alpha|^2\mu^2\sin(2\omega_m u_m)\left(\mathrm{e}^{\mathrm{i}2\omega_m u_m}S_{\delta\rho}(\nu)-\mathrm{e}^{-\mathrm{i}2\omega_m u_m}S_{\delta\rho}(-\nu)\right)\;, \quad (4.91)$$

which is the part that we can experimentally access in the power spectrum of the photocurrent (see (4.26)). Using this expression, we see that the following linear combination yields the PSD of the BEC density fluctuations at frequencies ν

$$S_{\delta\rho}(\nu) \;=\; \frac{\mathrm{e}^{\mathrm{i}2\omega_m u_m}\overline{S}_{\mathrm{bec}}(2\omega_m+\nu)+\mathrm{e}^{-\mathrm{i}2\omega_m u_m}\overline{S}_{\mathrm{bec}}(2\omega_m-\nu)}{2M^2|\alpha|^2\mu^2\sin(2\omega_m u_m)\sin(4\omega_m u_m)}\;. \quad (4.92)$$

Now that we know where in the spectrum the Unruh signal is to be expected, we have to estimate the noise content at these frequencies in order to be able to detect it. The power spectrum in general contains parts to several orders in μ. As μ is considered a small coupling, higher orders of μ are negligible small and we only consider contributions up to order μ^2. The back-action

[2] Using $2\sin(x)\cos(x)=\sin(2x)$.

correlator is such a contribution at order μ^4. Most crucially, we see that those contributions all appear at different orders in μ.

The shot noise contribution to the PSD is unaffected by the interaction with the BEC and can be calculated using (4.86). As we are interested in the signal around $2\omega_m$, we can calculate the shot noise power at those frequencies. The shot noise number operator at frequencies $2\omega_m+\nu$ can be calculated to

$$\delta\hat{n}_{\mathrm{sn},2\omega_m+\nu} = \frac{M|\alpha|}{2}\mathrm{e}^{-\mathrm{i}\omega_m u_m}\left(\mathrm{e}^{-\mathrm{i}\varphi}\delta\hat{a}_{+,\nu}+\mathrm{e}^{\mathrm{i}\varphi}\delta\hat{a}^{\dagger}_{-,-\nu}\right), \tag{4.93}$$

using the spectral decomposition of (4.86). The shot noise spectrum at frequencies $2\omega_m$ is then given by

$$S_{\mathrm{sn}}(2\omega_m) = \int_{-\Delta}^{\Delta}\mathrm{d}\nu\ \langle\delta\hat{n}^{\dagger}_{2\omega_m}\delta\hat{n}_{2\omega_m+\nu}\rangle = \left(\frac{M|\alpha|}{2}\right)^2. \tag{4.94}$$

Besides the BEC contributions, there are cross-correlations of the back-action with the shot noise at order μ^2 in the PSD. The corresponding calculations can be done using the material that has been presented in this section, however, for the moment we want to focus on the BEC signal and the shot noise.

The shot noise power in equation (4.94) scales with $|\alpha|^2$, which is the coherent amplitude and therefore proportional to the intensity of the electromagnetic field (equation 3.13). In contrast, the BEC power in equation (4.91) scales with $|\alpha|^2\mu^2$. Since $\mu\sim|\alpha|$, the BEC power is proportional to the squared intensity of the electromagnetic field. An increase in the intensity of the electromagnetic field will therefore increase the BEC power more than the shot noise power. Consequently, we could increase the intensity to optimise the signal-to-noise ratio, defined as the BEC power over shot noise power, however, note that the maximum power, that can be used in the actual experiment, is constraint by the scattering rate (3.14).

This conclusion supports the results in the section about the conceptual outline of this experiment (see equation (3.90)). Furthermore, we have provided a supplementary derivation of the power spectrum based on the operator description of the electromagnetic field and photon counting processes at the photodiode. In the next section, we briefly outline how these findings can be used in the superfluid Helium analogue.

4.3 Detectability of the Unruh Effect in Superfluid Helium-4

In the previous section, we derived in detail what the measured power spectrum in the BEC analogue experiment would be. As mentioned earlier, there are some differences in the superfluid Helium analogue. Foremost, the resonance frequencies in Helium do not allow for a sideband structure. This entails that the photon pressure could have a non-negligible effect on superfluid Helium (see section 3.3) and consequently, the Bogoliubov transformation looks slightly different. In order to extract the phase information of the laser, we will have to use interferometric setups, such as a homodyning detection scheme. The setup as proposed in the previous chapter (see figure 3.7) consists of two beam splitters and the superfluid Helium sample inducing a phase shift in one of the interferometer arms. Figure 4.6 shows the last step of this setup, namely the combination of signal and reference arm at the last beam splitter and subsequent detection.

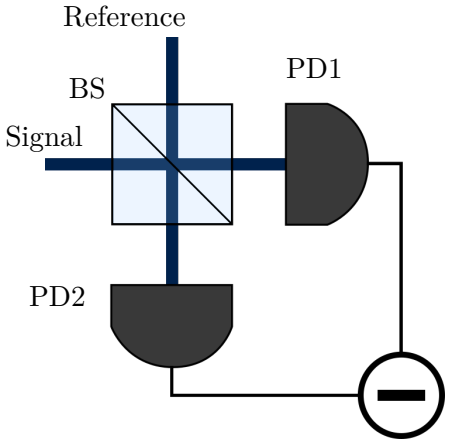

Figure 4.6 (Interferometric Setup) Homodyning setup for superfluid Helium-4 (for full schematics see 3.7). The signal and reference arm are combined at a beam splitter (BS) and subsequently detected in two photodiodes (PD1,PD2).

Detailed calculations on how to obtain the power spectrum of the measured signal is subject of ongoing research, however, we briefly outline conceptually how the results of the previous section can be used in this setup. Formally, the interaction is given by equation (3.125), which shows that the height fluctuation transduce into the laser phase. This interaction is the very same as in the BEC proposal, however, this setup is slightly easier to treat than the BEC setup as it only has one carrier frequency, instead of two sidebands. As such, the Bogoliubov transformation look similar evaluated for one sideband only, although there is some care necessary as the BEC Bogoliubov transformation assumed that the zero order contribution of the laser on the BEC is cancelled out by the two sideband structure. This needs to be accounted for in superfluid Helium and could modify the result of the Bogoliubov transformation.

Furthermore, we can use the homodyning description of section 4.1.3 to find the detected signal at the photodiodes. Using the homodyning photocurrent, the signal extraction procedure looks similar to the one presented in the previous section. In particular, one has to look at which frequencies the correlations of height fluctuations in Helium appear and what the noise content is. This allows us to calculate the corresponding power spectra and define a signal-to-noise ratio, similarly to the one in the conceptual discussion.

4.4 Summary

In this chapter, we have derived the transformations on the operators of the electromagnetic field, as it interacts with the components of the experiment. For this purpose, we presented first the modelling of the photodetection process and showed that by calculating the power spectrum of the measured photocurrent at a photodiode, we retrieve the symmetrised power spectrum of the photon flux.

In order to apply this result to the analogues presented in the previous chapter, we calculated the photon flux explicitly for the BEC analogue. We showed that each element of the experiment imposes a transformation on the operators of the electromagnetic field. The key element of these transformations was the interaction with the BEC, which can be conveniently written as a Bogoliubov transformation on the operators of the electromagnetic field and the BEC. This made clear that the BEC interaction amplifies certain modes in the electromagnetic field and de-amplifies others. On the other hand, the electromagnetic field induces noise in the BEC, causing back-action contributions. We showed that the symmetrised power spectrum of the photon flux consequently contains contributions from the shot noise, the BEC and back-action. We derived a formalism how to extract the BEC correlations in a certain frequency regime of the symmetrised PSD and calculated the shot noise power at those frequencies. We identified the relevant scaling of the corresponding SNR, defined as the BEC power over the shot noise power, with the intensity of the electromagnetic field and compared it to the discussion of the conceptual setup in the previous chapter.

We then gave a brief outlook on how this modelling can be applied to superfluid Helium. The crucial difference in this analogue is that, compared to the BEC, a sideband structure with opposite detuning from resonance frequencies of Helium is not feasible experimentally. This has multiple consequences. First, in order to resolve the phase of the laser in which the Unruh signal is expected, we need, for example, a homodyning setup instead of a direct photo detection. Second, this changes the Bogoliubov transformation for the interaction with Helium, which requires a more careful treatment. The details of this transformation and the signal extraction are subject of further research.

The calculations in this chapter complement the experimental considerations in the previous chapter and provides an exact formalism how the signal of the Unruh effect can be extracted in an experiment.

V

Experiment

The goal in this chapter is to establish a series of experiments that can be used to measure the Unruh effect in superfluid Helium-4 with a continuous, localised laser beam. The experimental proposal is based on the setup in [57, 58]. The first step is to build an experiment to measure thermal surface fluctuations on classical fluids. The main focus of this chapter is to establish a low noise detection scheme. One way to achieve this is a confocal microscope setup. Once we have introduced a setup for classical fluids we give an outlook on how this experiment can be extended to superfluids in order to measure the analogue Unruh effect.

5.1 Thermal Fluctuations on Classical Fluids

In this section, we present a detection scheme for thermal interface fluctuations on classical fluids as suggested in [57]. The detection method is a variation of confocal microscopy with the key elements being a pinhole aperture in combination with a focusing lens. Before we go into the explicit experimental setup, we will provide a brief theory introduction to power spectra of height fluctuations on classical fluids.

5.1.1 Power Spectrum of Height Fluctuations

The dynamics of an incompressible fluid with surface tension σ, viscosity η, density ρ, velocity $\boldsymbol{u}$, and pressure p is described by the Navier-Stokes equation and the incompressibility condition [123]. Linearising the pressure $p \to p_0 + p$ and velocity $\boldsymbol{u} \to \boldsymbol{u}_0 + \boldsymbol{u}$ around a background yields the linearised Navier-Stokes equation

$$\partial_t \boldsymbol{u} \;=\; -\frac{\nabla p}{\rho} + \frac{\eta}{\rho}\nabla^2 \boldsymbol{u}\,, \tag{5.1a}$$

$$\nabla \cdot \boldsymbol{u} \;=\; 0\,. \tag{5.1b}$$

Eventually, we are interested in the power spectrum of the height fluctuations on the surface, namely

$$S_{\delta h}(\omega, \boldsymbol{k}) \;=\; \int_{-\infty}^{\infty} \mathrm{d}t\; \mathrm{e}^{\mathrm{i}\omega t}\, \langle \delta h(t, \boldsymbol{k}) \delta h^*(0, \boldsymbol{k}) \rangle \;. \tag{5.2}$$

Note that most generally in the literature, the fluid is assumed to be semi-infinite with a surface at $z = 0$ and a no-slip boundary condition $\boldsymbol{u} \to 0$ for $z \to -\infty$. This gives us an expression for the Laplace and Fourier transform of the velocity perturbation at the surface of the liquid. Then we identify the time derivative of the height field on the surface with the velocity perturbations, i.e. $\partial_t \delta h = u_z$ to obtain an expression for the Laplace and Fourier transform of the height fluctuations. This expression can in turn be used to calculate the power spectrum in equation (5.2). The final result for the power spectrum of height fluctuations on a classical fluid at temperature T is

$$S_{\delta h}(\omega, \boldsymbol{k}) \;=\; \frac{k}{\rho}\left(\frac{\rho}{2\eta k^2}\right)^2 \frac{\mathrm{Im}\left\{\mathrm{i}\frac{\omega\rho}{\eta k^2} - \sqrt{1 - \mathrm{i}\frac{\omega\rho}{2\eta k^2}}\right\}}{\left|\frac{\sigma\rho}{4\eta^2 k} + \left(1 - \mathrm{i}\frac{\omega\rho}{2\eta k^2}\right)^2 - \sqrt{1 - \mathrm{i}\frac{\omega\rho}{2\eta k^2}}\right|^2} \frac{k_\mathrm{B} T}{\omega\pi}\,. \tag{5.3}$$

The expression above can be generalised for a system of two fluids that do not mix, such as air/water interfaces or oil/water interfaces. In such a case, we simply replace $\eta = \eta_1 + \eta_2$ and $\rho = \rho_1 + \rho_2$.

The crucial assumption behind the derivation of the spectrum (5.3) is the one of a semi-infinite fluid. Aoki and Mitsui [57, 58] claim that their experimental data of their proposed setup fits this theoretical prediction quite well. In the detection scheme that we will introduce in this chapter, the boundary conditions are different as the fluid sample is contained in a finite size basin. The difference in the boundary condition will therefore have an effect on the explicit form of the power spectrum. For a conceptual discussion, let us look at the expression for the height field in our setup. The basin is a cylindrical shaped container of height h_0, so it is natural

to decompose the height field into a radial, angular and time-dependent part

$$\delta h(t, r, \theta) \;=\; R(r)\Theta(\theta)T(t)\;. \tag{5.4}$$

This ansatz can be used in the dynamic equations (5.1) and proceeding with this separation ansatz, we see that the t- and θ-dependent parts obey wave equations. Solving the equations for R, Θ and T shows that the height fluctuations can be written as

$$\delta h(t, r, \theta) \;=\; \sum_m \cos(m\theta) J_m(kr) T(t)\;, \tag{5.5}$$

where J_m are Bessel functions of the first kind. What are the exact boundary conditions for this system? In principle, there are two main options. First, we could demand that the height at the boundary is equal to its equilibrium height h_0 and therefore $\delta h(t, R, \theta) = 0$, yielding

$$J_m(kR) \;=\; 0 \quad , m \in \mathbb{N}\;. \tag{5.6}$$

Alternatively, we could demand that the velocity in radial direction is zero at the boundary, i.e. $\partial_r \delta h(t, R, \theta) = 0$, resulting in

$$J'_m(kR) \;=\; 0 \quad , m \in \mathbb{N}\;. \tag{5.7}$$

One part of the preparation for this experiment is therefore to understand how the system behaves and what the appropriate boundary conditions are. In both cases, these boundary conditions restrict the modes that are present in the system by imposing a condition on possible k values, as kR has to be a zero of either the Bessel functions, or their derivatives. Since Bessel functions are periodic, there are infinitely many zeroes for a given m value. We label the k value of the nth zero of the mth Bessel function with another subscript n, i.e. k_{mn}. The corresponding frequencies are given by the standard dispersion relation

$$\omega_{mn}^2 \;=\; \left(\rho g + \sigma k_{mn}^2\right) \frac{k_{mn} \tanh\left(k_{mn} h_0\right)}{\rho}\;, \tag{5.8}$$

where g is the gravitational acceleration.

We discussed the spectrum of height fluctuations, however as we will see later, the setup we are proposing is only sensitive to the inclination spectrum of the reflected probing laser on the surface. The spectrum will therefore indicate which modes are present in this particular system.

5.1.2 Confocal Microscopy

As we have mentioned in the introduction of this chapter, we want to use a confocal microscopy setup to measure the inclination spectrum of thermal height fluctuations on classical fluids. We will explain the setup step-by-step and give a justification why this leads to the desired outcome. A schematic of the setup with a 633 nm wavelength Helium-Neon laser is shown in figure 5.1. In principle, this setup is designed to detect the offset in the laser beam position due to a reflection on the surface of the fluid. Before going into the details of this setup, let us have a look what happens at the surface of the fluid sample.

Optical Lever Approximation. In a first approximation, the surface of the fluid can be treated as an optical lever. Effectively, this means that a laser beam is reflected from the surface

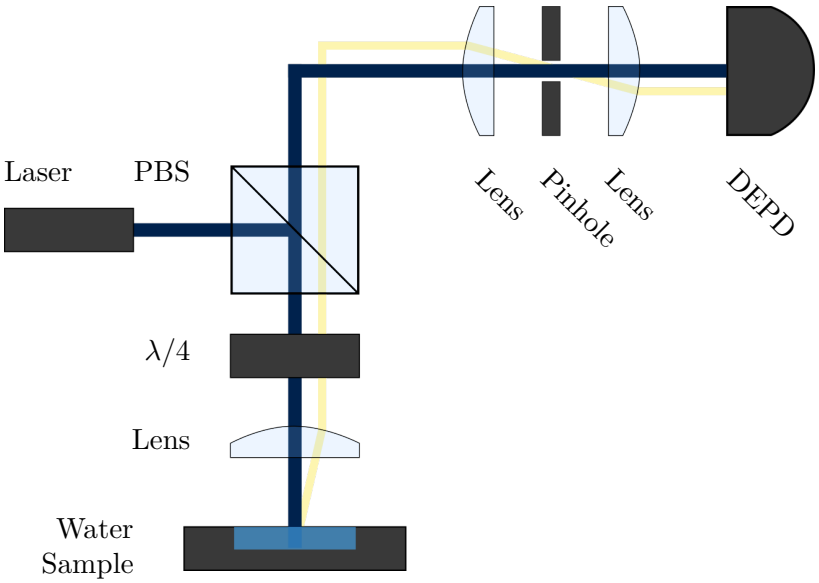

Figure 5.1 (Confocal Microscopy Setup) Experimental setup to measure inclination spectrum on water. The laser beam is reflected by a polarising beam splitter (PBS) and focused with a lens on the water sample in a basin with a 2 inch diameter and depth of 12 mm. The spatial filter combination of lens, aperture and lens filters out unwanted noise before the laser is being detected at a dual-element photodiode (DEPD). The blue path represents the beam path without reflection at the surface, whereas the yellow path is an example of a reflected beam at the sample surface.

as if there was a mirror tangential to the fluid surface at this point [124]. As the fluid surface is approximately located in the focal point of the lens, all reflected beams after the lens are parallel to incoming beams. The surface of the fluid is constantly moving, so the direction of the reflected beam changes according to the gradient of the height field at the point of reflection.

$\lambda/4$-Waveplate and Focussing Lens. After the reflection at the polarising beam splitter, the beam passes through a $\lambda/4$-waveplate. This waveplate changes the polarisation of the beam in such a way that, after the beam went through it twice, it will be transmitted at the polarising beam splitter, instead of being reflected. The focussing lens with focal length $f = 25$ mm focusses the laser beam on the surface of the sample.

Pinhole. After the beam splitter, the transmitted laser beam is focused on a pinhole with a focusing lens with focal length $f = 13.86$ mm. The pinhole aperture has a diameter of 15 μm. After the pinhole, a second focusing lens with focal length $f = 50$ mm aligns the direction of the outgoing beam. The pinhole acts as a spatial filter and filters out any ambient noise source.

Photodiodes. The signal is detected with a Hamamatsu Si Photodiodes S3096-02. This is a dual-element photo diode (DEPD), which is a combination of two adjacent photo sensitive elements. Aligning the detected laser in such a way that it hits the DEPD centrally, i.e. at the intersection of both elements, one can measure the position of the laser by independently measuring the intensities $i_i(t)$ at both photo elements, where $i \in \{1, 2\}$ labels the two elements

of the DEPD, and calculate their difference

$$i(t) \;:=\; i_1(t) - i_2(t)\;. \tag{5.9}$$

As long as the laser is entirely captured by the DEPD the sum of intensities will be approximately constant. Since the laser position due to the reflection at the surface fluctuates, the detected photo current difference $i(t)$ will fluctuate with time. It can be shown that this difference is connected to the reflection angle θ on the surface of the liquid [57, 58]

$$\frac{i_1(t) - i_2(t)}{i_1(t) + i_2(t)} \;=\; \frac{2\theta}{\mathrm{NA}}\;, \tag{5.10}$$

where NA is the numerical aperture of the microscope objective.

Data Acquisition. The Tektronix DPO4032 oscilloscope provides a convenient way to measure the photo currents of the DEPD. Each element of the DEPD is connected via a transimpedance amplifier (Thorlabs AMP 140, impedance 10 kV/A) to an input channel of the oscilloscope. The data from the oscilloscope is directly taken with a computer, which calculates the difference of both input channels. For the purpose of data acquisition, we have developed a data acquisition tool with which it is possible to take data from the oscilloscope in a structured and automated way. The tool is entirely built in Python and SQLite3.

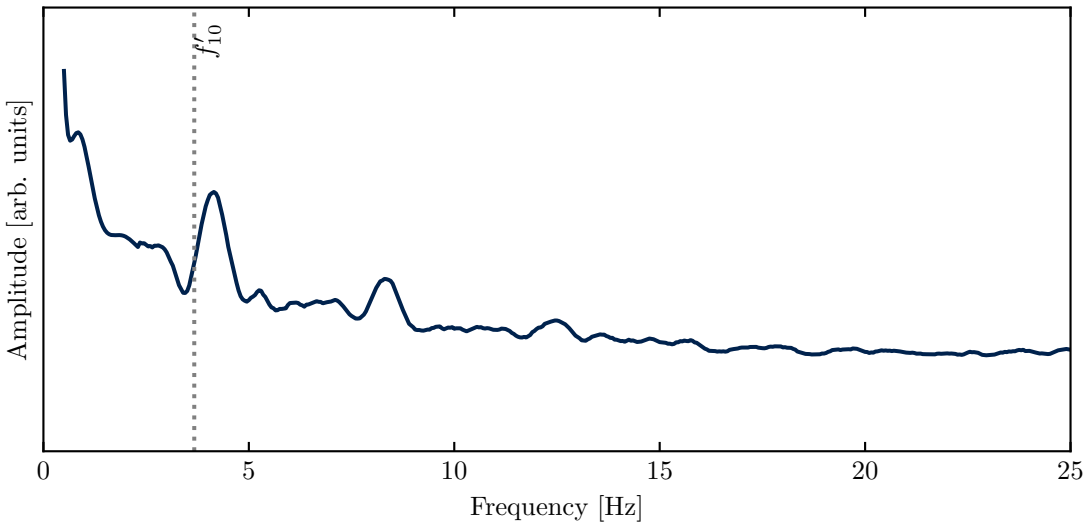

Figure 5.2 (Difference Current Spectrum) Spectrum of difference current for a sampling rate of 500 S/s. Note that the vertical axis is given in arbitrary units. The dataset is an average over ten realisations. Vertical line shows an example of a Bessel mode at f'_{10} =3.7 Hz that corresponds to the first zero of the derivative of the Bessel function J_1.

Signal and Results. Equation (5.10) shows that measuring the difference current of the DEPD can be converted into the reflection angle of the beam on the surface, thus, the spectra of both are related

$$S_i(\omega, \boldsymbol{k}) \;=\; \frac{2I}{\mathrm{NA}} S_\theta(\omega, \boldsymbol{k}) \;. \tag{5.11}$$

This expression represents the original claim that this setup is only sensitive to the inclination spectrum of height fluctuations. As explained in the beginning of this chapter, we expect to see modes in this spectrum that are characteristic to the geometry of the basin and the fluid. The basin has a cylindrical with a radius of 2 inch and a depth of 12 mm. Therefore, we would expect to see characteristic frequencies of Bessel modes in the spectrum. The first data indicates that we might indeed see the eigenmodes of the system (see figure 5.2). As the data acquisition is still in its infancy, we use this data set as a motivation for continuing the experiment with larger data sets, experimental improvements and tests in different fluids to make a justified statement about the quality of this method. As such this plot does not contain any experimental errors and is meant as a guidance only. Furthermore, we need to compare the results to different methods, such as off-axis holography readily available in our research group. Once we have a solid understanding of this detection method, we can further develop it to detect thermal excitations on the surface instead of just eigenmodes of the basin.

The data in figure 5.2 shows the spectrum of the difference current. This data set is an average over ten runs and shows the frequency content up to 25 Hz. The sampling rate was 500 S/s with a total measurement time of 20 s. The spectrum shows prominent peaks at 4Hz and 8Hz. As mentioned in section 5.1.1, we expect to see the eigenmodes of the system as given by the zeroes of the Bessel function, or their derivatives respectively. The dashed, vertical line in this plot represents the frequency of the first zero of the derivative of the Bessel function $J_1(x)$. We see that the theoretical prediction for this peak slightly deviates from the measured one. Due to the curved surface, or meniscus, of water in a basin, the depth of water slightly varies over the whole area of the sample, effectively changing the dispersion relation locally. As the laser beam was slightly offset from the centre of the water sample this shift could be due to this meniscus effect.

Limitations and Noise. This setup is only sensitive to the inclination spectrum of the height fluctuations and there is a priori no way to extract the absolute height of the fluid. However, we think that this method can be combined in detection schemes to build experiments that are sensitive to the absolute value of height fluctuations. In addition, this setup suffers from a few experimental issues, in particular the evaporation of the fluid and induced noise, in particular from electronics. The most obvious solution to evaporation is to constantly realign the focus on the surface, but we think there are more intelligent solutions such as automated translation stage adjustments. Sources of electronics noise need to be identified and isolated with various shielding boxes or electronic filters. Due to the small size of the water sample, there are meniscus effects on the boundaries that slightly change the dispersion relation and effectively shift the peaks in the spectrum. More measurements are necessary to quantify the effect of the meniscus such that final datasets can be adjusted accordingly. Lastly, there is still the open question which boundary condition is correct. For a definitive answer, more tests are necessary.

In order to reduce the noise, two DEPDS can be used to detect the signal after another beam splitter following the spatial filter. Then calculating the correlator using the difference current

from both photo diode will reduce uncorrelated noise induced in the measurement process. This detection method is used in the original proposal [57] and might be implemented in a further stage of this experiment.

Despite some open questions and necessary refinement of this system, the measured data shows motivating first results that justify a promising outlook for further experiments.

5.2 Outlook for Superfluid Helium

In the previous section, we showed how a confocal microscopy setup can be used to detect thermal interface fluctuations on classical fluids, such as water. The setup was inspired by a proposal from Mitsui and Aoki [57, 58], who used this method to measure fluctuations on various media, such as water, oil and ethanol. The first data sets look promising in the sense that we seem to detect the eigenmodes of the system, however, this is the very first stepping stone to a larger series of experiments confirming these findings. The difference to the original proposal is the specific geometry of our setup. While Mitsui and Aoki assume an infinitely sized fluid, our system is confined to a cylindrical basin. We will therefore expect to see geometry specific eigenmodes of the system in the spectrum.

In principle this method is not limited to classic fluids only but can be extended to superfluids, as well. In essence, the conceptual setup will be the same as before, with a superfluid Helium-4 sample instead of a water sample. However, this leads to experimental challenges as the whole setup needs to be cooled down and placed in a dilution fridge, or equivalent cooling device.

In summary, our findings mark a first promising step of many experimental successes needed to detect the Unruh effect in superfluid Helium-4. The first chapters of this thesis showed that the acceleration of the laser on a circular trajectory leads to an imprint of height fluctuations in the laser phase. Consequently, it is necessary to build an experiment that can resolve phase differences. The confocal microscopy setup showed that the pinhole is an excellent device to isolate the relevant signal and filter out ambient noise. It seems promising that this setup can be refined in an interferometric setup as a detection scheme for the Unruh effect [58]. In this chapter, the first step was to set up a static detector for thermal interface fluctuations, however, for the Unruh effect one has to think about an explicit implementation of the circular acceleration.

VI

Conclusion

In this thesis, we investigated the Unruh effect and presented the development from an abstract two-level detector in relativistic quantum field theory, to measurement schemes with continuous detectors in analogue systems and associated intricate technical challenges every physical detection scheme faces.

After a brief introduction of the linear acceleration Unruh effect in QFT in chapter II [17], we extended the original description to a circular accelerated trajectory. A circular trajectory was the first step towards an actual implementation in a laboratory, as the space that is required for such a setup is confined. The detailed balance condition defines the Unruh temperature in terms of the response function of a detector. The main part of this chapter was therefore dedicated to the calculation of response functions. In particular, we calculated the response function in $(3+1)$ and $(2+1)$ dimensions, since, as we saw in later chapters, the presented analogue systems are effectively described by a $(2+1)$ dimensional field theory. We found that in the ultra-relativistic limit in $(2+1)$ dimensions the linear prediction Unruh temperature for a circular motion is similar to the actual circular Unruh temperature, justifying the simplified use of the linear prediction in later chapters. Then, we introduced the concept of a continuous detector, for which the aforementioned results can be equally applied. This continuous detector model, consisting of two interacting scalar fields, is the blueprint for the analogue models in this thesis. We concluded the chapter with a derivation of the response functions in analogue systems. The results were published in [54].

Chapter III was about establishing two explicit analogue systems. Based on the concept of a continuous detector, we showed that a laser beam interacting with polarisable matter provides an interaction that can be mapped to the interaction in the detector model of chater II. In particular, the phase fluctuations in the laser beam take the role of the probing field of the continuous detector model. We presented two systems that can be used as an analogue model:

a two dimensional, oblate Bose-Einstein condensates and thin film superfluid Helium-4. In a BEC, linearised density perturbations couple to the phase fluctuations in the laser beam and both fields, density and laser fluctuations, behave effectively as massless Klein-Gordon fields. In superfluid Helium-4, on the other hand, the height fluctuations behave as a massless scalar field and couple to the laser phase fluctuations. In both cases, we provided a schematic setup for a potential experimental implementation and calculated the signal-to-noise ratio to make a feasibility statement about the signal detection. Using a zero-temperature initial state, we found that for multiple repetitions of the experiment the signal is well above the shot noise induced phase noise. In the superfluid analogue, however, some assumptions are too restrictive, which requires further research. In particular, we briefly discussed the non-zero ambient temperature for Helium experiments. The analysis of the BEC analogue was published in [55], whereas the superfluid Helium analysis is currently still work in progress [56].

In chapter IV, we introduced the concept of the quantum mechanical photonflux and how this quantity relates to the classically measured photocurrent. We then proceeded by calculating the photo current at the photo diode in the BEC proposal and showed how to extract the signal of the Unruh effect. The focus was on the operator transformation for the interaction with the BEC. We derived that this interaction can be conveniently expressed in terms of a Bogoliubov transformation. Then, we showed how this Bogoliubov transformation can be applied to the superfluid Helium proposal. We derived the exact composition of the photocurrent and at which frequencies the signal due to the Unruh effect is expected. This chapter contains unpublished work.

In the last chapter V, we outlined an detection method that can facilitate an Unruh detector in superfluid Helium with a confocal microscopy setup. We presented first experimental results to locally extract the inclination spectrum of height fluctuations on water as seen by a static observer, using a microscope lens and a spatial filter. Preliminary results show that this detection scheme is a promising candidate for more complex experiments, such as implementations in superfluid Helium and finally, in combination with interferometers and detectors in accelerated motion, to detect the Unruh effect.

Outlook

We saw that the Unruh effect in its relativistic QFT description is extremely difficult to measure and there has been no experimental evidence of it to date. The novel approach to formulate the Unruh effect in the context of continuous detectors is a complete game changer as it opens up a whole new range of experiments to probe this fascinating effect and the quantum vacuum more generally. We have shown that the detection of the Unruh effect is not only theoretically possible in analogue systems, such as Bose-Einstein condensates and superfluids, but that it is already in the realm of current experimental possibilities.

Having established the analogy in cold-atom systems, the next stage is to work towards actual experiments. In this thesis, we have outlined a series of experiments that will be realised in the near future. Along with the preparation of those experiments, more detailed analysis will be conducted to further fine-tune the experimental parameter sets and to get a deeper understanding of finite size effects, non-zero temperature effects and back-action.

A

Theorems, Identities, and Integrals

A.1 Laplace's Method

Laplace's method attempts to approximate the large x limit of the integral [128]

$$I(x) \;=\; \int_a^b \mathrm{d}t\; g(t)\mathrm{e}^{xf(t)}\;, \tag{1.1}$$

with $a, b, f(t) \in \mathbb{R}$. Now suppose $f(t)$ has a global maximum at t_0, such that $f'(t_0) = 0$ and $f''(t_0) < 0$. Expanding f in a Taylor series around that maximum results in $f(t) \approx f(t_0) - \frac{1}{2}|f''(t_0)|(t-t_0)^2$, where we used that at this point the first derivative of f vanishes. For t close to t_0 we can therefore write

$$I(x) \;\approx\; \mathrm{e}^{xf(t_0)} \int_a^b \mathrm{d}t\; g(t)\mathrm{e}^{-x\frac{1}{2}|f''(t_0)|(t-t_0)^2}\;. \tag{1.2}$$

For $a \to \infty$ and $b \to -\infty$ the integral on the right is a Gaussian integral, which can be calculated resulting in

$$I(x) \;\approx\; \sqrt{\frac{2\pi}{x|f''(t_0)|}}\, g(t_0)\mathrm{e}^{xf(t_0)}\;. \tag{1.3}$$

A.2 Clausius-Mossotti Relation

The Clausius-Mossotti relation tells us that

$$\epsilon - \epsilon_0 \;=\; \frac{4\pi\rho\alpha}{1 - \frac{4\pi}{3}\frac{\rho\alpha}{\epsilon_0}}\;, \tag{1.4}$$

which connects the electric permittivity ϵ to the polarisability α of the fluid. For $\frac{4\pi}{3}\frac{\rho\alpha}{\epsilon_0} \ll 1$ we find that

$$\epsilon \;\approx\; \epsilon_0 + 4\pi\rho\alpha \;, \tag{1.5}$$

A.3 Residue Theorem

Let $f(z)$ be holomorphic function defined on $\Omega \in \mathbb{C}$ except for some points $z_n \in \mathbb{C}$. The integral of $f(z)$ along any closed path γ in $\Omega/\{z_n\}$ can be evaluated using the enclosed residues at z_n

$$\oint_\gamma \mathrm{d}z\; f(z) \;=\; 2\pi\mathrm{i} \sum_n \mathrm{Res}(f, z_n) \;. \tag{1.6}$$

A.4 Dominated Convergence

Let (f_n) be a sequence of complex-valued functions defined on Ω that converges pointwise to a function f. In addition, let this sequence dominated by another function g such that

$$|f_n(x)| \;\leq\; g(x) \;, \tag{1.7}$$

for all n and $x \in \Omega$. Then f is integrable and

$$\lim_{n\to\infty} \int_\Omega \mathrm{d}x\; |f_n(x) - f(x)| \;=\; 0 \;. \tag{1.8}$$

Equivalently, dominated convergence says that

$$\lim_{n\to\infty} \int_\Omega \mathrm{d}x\; f_n(x) \;=\; \int_\Omega \mathrm{d}x\; f(x) \tag{1.9}$$

A.5 Hadamard's Lemma

Consider the operator

$$\mathrm{e}^{s\hat{X}} \hat{Y} \mathrm{e}^{-s\hat{X}} \tag{1.10}$$

for $s \in \mathbb{C}$. A Taylor expansion around $s = 0$ shows that

$$\mathrm{e}^{sX} Y \mathrm{e}^{-sX} \;=\; Y + [X, Y]s + \frac{1}{2}[X, [X, Y]]s^2 + \dots \;. \tag{1.11}$$

If the commutator is central, then

$$\mathrm{e}^{sX} Y \mathrm{e}^{-sX} \;=\; Y + [X, Y]s \;. \tag{1.12}$$

B

Detailed Calculations

B.1 Useful Integrals

2.1.1 sin Es/s

$$\int_0^\infty \mathrm{d}s \frac{\sin(Es)}{s} \;=\; \frac{1}{2}\int_{-\infty}^\infty \mathrm{d}s \frac{\sin(Es)}{s} \;=\; \frac{1}{2}\mathrm{Im}\int_{-\infty}^\infty \mathrm{d}z \frac{\mathrm{e}^{\mathrm{i}Ez}}{z}\,. \tag{2.1}$$

This integral has a pole at $z = 0$. For this integration, we proceed by choosing the integration contour $\mathcal{C}_1$ as in figure 2.2 for $E > 0$. For $E < 0$ we close the integration contour in the lower half of the complex plane, passing the origin from below. The integration along the outer semi circle does not contribute in the limit $R \to \infty$. The integration along the inner semi circle with radius ϵ is parametrised with $z = \epsilon \mathrm{e}^{\mathrm{i}\theta}$, $\theta \in [0, \pi]$ for the upper semi circle and $z = \epsilon \mathrm{e}^{\mathrm{i}(2\pi-\theta)}$, $\theta \in [0, \pi]$ for the lower one.

$$\lim_{\epsilon\to 0}\int_{\gamma_\epsilon^+} \mathrm{d}z \frac{\mathrm{e}^{\mathrm{i}Ez}}{z} \;=\; \lim_{\epsilon\to 0}\mathrm{i}\int_0^\pi \mathrm{d}\theta \exp\{\mathrm{i}E\epsilon\mathrm{e}^{\mathrm{i}\theta}\} \;=\; \mathrm{i}\pi\,. \tag{2.2}$$

For the integration with $E < 0$ in the lower semi circle we find

$$\lim_{\epsilon\to 0}\int_{\gamma_\epsilon^-} \mathrm{d}z \frac{\mathrm{e}^{\mathrm{i}Ez}}{z} \;=\; \lim_{\epsilon\to 0} -\mathrm{i}\int_0^\pi \mathrm{d}\theta \exp\{\mathrm{i}E\epsilon\mathrm{e}^{\mathrm{i}(2\pi-\theta)}\} \;=\; -\mathrm{i}\pi\,. \tag{2.3}$$

As we know by Cauchy's integral theorem, the sum of all those integrals has to be zero and we find that the integral along the real axis is given by

$$\int_0^\infty \mathrm{d}s \frac{\sin(Es)}{s} \;=\; -\frac{\pi}{2}\operatorname{sgn} E \tag{2.4}$$

2.1.2 $(1-\cos \mathbf{Es})/\mathbf{s^2}$

$$\int_0^\infty \mathrm{d}s \frac{1-\cos(Es)}{s^2} \;=\; \frac{1}{2}\int_{-\infty}^{\infty} \mathrm{d}s \frac{(1-\cos(Es))}{s^2} \;=\; \frac{1}{2}\mathrm{Re}\int_{-\infty}^{\infty} \mathrm{d}z \frac{(1-\mathrm{e}^{\mathrm{i}Ez})}{z^2}\,. \tag{2.5}$$

This integral has a single pole at $z=0$. First, notice that the integrand can be rewritten using the Taylor expansion of the exponential

$$\frac{(1-\mathrm{e}^{\mathrm{i}Ez})}{z^2} \;=\; -\frac{\mathrm{i}E}{z} + \mathcal{E}(z)\,, \tag{2.6}$$

for some function $\mathcal{E}(z) \to \frac{1}{2}E$ for $z \to 0$. Choosing the integration contour as in section 2.1.1 of the appendix, the contribution of the outer auxiliary semi circle vanishes such that

$$\int_{|z|>\epsilon} \mathrm{d}z E\left(-\frac{\mathrm{i}}{z}+\mathcal{E}(z)\right) \;=\; \int_{\gamma_\epsilon} \mathrm{d}z E\left(-\frac{\mathrm{i}}{z}+\mathcal{E}(z)\right)\,. \tag{2.7}$$

Parametrising the contour γ_ϵ with $z=\epsilon \mathrm{e}^{\mathrm{i}\theta}$ for the upper semi circle and $z=\epsilon \mathrm{e}^{\mathrm{i}(2\pi-\theta)}$ with $\theta \in [0,\pi]$ for the lower semi circle, we see that in the limit $\epsilon \to 0$ we find

$$\int_{-\infty}^{\infty} \mathrm{d}s \frac{1-\cos(Es)}{s^2} \;=\; |E| \int_{\pi}^{0} \mathrm{d}\theta\,(1+O(\epsilon)) \;=\; |E|\pi\,, \tag{2.8}$$

and finally

$$\int_0^\infty \mathrm{d}s \frac{1-\cos(Es)}{s^2} \;=\; |E|\frac{\pi}{2}\,. \tag{2.9}$$

B.2 Response Functions

2.2.1 Response Function of Unruh-DeWitt Detector on Inertial Trajectory

The response function of an Unruh-DeWitt detector on an inertial trajectory $x(\tau)=(\gamma\tau,\gamma\boldsymbol{v}\tau)$ is given by

$$\mathcal{F}(E) \;=\; \frac{1}{4\pi^{\frac{d}{2}}}\int_{-\infty}^{\infty} \mathrm{d}\tau \mathrm{e}^{-\mathrm{i}E\tau} \frac{\Gamma\left(\frac{d}{2}-1\right)}{(-(\tau-\mathrm{i}\epsilon)^2)^{\frac{d-2}{2}}}\,, \tag{2.10}$$

which is regularised with $\tau \to \tau - \mathrm{i}\epsilon$ is understood in the limit $\epsilon \to 0+$.

In (3+1)d For $d=4$ the response function is given by

$$\mathcal{F}(E) \;=\; -\frac{1}{4\pi^2}\int_{-\infty}^{\infty} \mathrm{d}\tau \frac{\mathrm{e}^{-\mathrm{i}E\tau}}{(\tau-\mathrm{i}\epsilon)^2}\,. \tag{2.11}$$

The integrand has a pole of order 2 at $\tau=\mathrm{i}\epsilon$. The whole integral can be analytically continued to the whole complex plane and be expressed in terms of the residue at this pole after closing the integration contour in the upper complex plane (assuming $E<0$)

$$\mathcal{F}(E) \;=\; -\frac{\mathrm{i}}{2\pi}\mathrm{Res}_{\tau=\mathrm{i}\epsilon}\frac{\mathrm{e}^{-\mathrm{i}E\tau}}{(\tau-\mathrm{i}\epsilon)^2}\,. \tag{2.12}$$

The residue can be calculated to be

$$\mathrm{Res}_{\tau=\mathrm{i}\epsilon}\frac{\mathrm{e}^{-\mathrm{i}E\tau}}{(\tau-\mathrm{i}\epsilon)^2} \;=\; \frac{\mathrm{d}}{\mathrm{d}\tau}(\tau-\mathrm{i}\epsilon)^2\frac{\mathrm{e}^{-\mathrm{i}E\tau}}{(\tau-\mathrm{i}\epsilon)^2} \;=\; -\,\mathrm{i}E\mathrm{e}^{E\epsilon}\,. \tag{2.13}$$

In the limit $\epsilon \to 0+$ we finally find

$$\mathcal{F}(E) \;=\; -\,\frac{E}{2\pi}\,. \tag{2.14}$$

Note the derivation above assumes $E < 0$, however, closing the integration contour in the lower complex plane works equivalently for $E > 0$.

2.2.2 Ultrarelativistic (2 + 1) Reponse Function – Circular Motion Corrections

Consider the integral

$$\mathrm{sgn}(E)\int_0^\infty \mathrm{d}x\frac{\sin(Ex)}{x\sqrt{1+x^2}} \;=\; \frac{1}{2}\int_{-\infty}^\infty \mathrm{d}x\frac{\sin(|E|x)}{x\sqrt{1+x^2}}\,, \tag{2.15}$$

where on the right hand side we have absorbed the $\mathrm{sgn}(E)$ in the sine using that it is an odd function. Adding and subtracting a $1/x$ in the integrand and using the integral in section 2.1.1 we find

$$\frac{1}{2}\int_{-\infty}^\infty \mathrm{d}x\frac{\sin(|E|x)}{x\sqrt{1+x^2}} \;=\; \frac{\pi}{2}+\frac{1}{2}\int_{-\infty}^\infty \mathrm{d}x\sin(|E|x)\left(\frac{1}{x\sqrt{1+x^2}}-\frac{1}{x}\right)\,. \tag{2.16}$$

The part of the integrand in brackets is odd in x which means that we get result by using the integral

$$\frac{\pi}{2}-\frac{\mathrm{i}}{2}\int_{-\infty}^\infty \mathrm{d}x\mathrm{e}^{\mathrm{i}|E|x}\left(\frac{1}{x\sqrt{1+x^2}}-\frac{1}{x}\right) \tag{2.17}$$

where the contribution of the cosine vanishes due to its symmetry properties. Continuation in the whole complex plane allows us to choose the integration contour $\mathcal{C}_2$ as in figure 2.2 to arrive at

$$\frac{\pi}{2}-\frac{\mathrm{i}}{2}\int_{\mathcal{C}_2}\mathrm{d}z\frac{\mathrm{e}^{\mathrm{i}|E|z}}{z\sqrt{1+z^2}}\,, \tag{2.18}$$

where the pole at $z = 0$ is excluded. The denominator possesses poles at $z = 0$ and $z = \pm\mathrm{i}$. Since the integration contour is deformed in the upper plane the only interesting pole is at $z = \mathrm{i}$, however, the integration contour explicitely excludes this pole. We therefore know that by Cauchy this integral has to vanish. In the limit of infinitely small or large auxiliary circles this contour integral converges to the integral along the real axis plus a contribution from integrating around the pole at $z = \mathrm{i}$

$$\int_{\mathcal{C}_2}\mathrm{d}z\frac{\mathrm{e}^{\mathrm{i}|E|z}}{z\sqrt{1+z^2}} \;\to\; \int_{-\infty}^\infty \mathrm{d}x\frac{\mathrm{e}^{\mathrm{i}|E|x}}{x\sqrt{1+x^2}}+\oint_{z=\mathrm{i}}\mathrm{d}z\frac{\mathrm{e}^{\mathrm{i}|E|z}}{z\sqrt{1+z^2}}\,, \tag{2.19}$$

where the integral on both sides of the branch cut can be calculated to be

$$\oint_{z=\mathrm{i}}\mathrm{d}z\frac{\mathrm{e}^{\mathrm{i}|E|z}}{z\sqrt{1+z^2}} \;=\; 2\int_1^R \mathrm{d}y\frac{\mathrm{e}^{-|E|y}}{y\sqrt{1-y^2}}\,. \tag{2.20}$$

We finally obtain

$$\operatorname{sgn}(E)\int_0^\infty \mathrm{d}x \frac{\sin(Ex)}{x\sqrt{1+x^2}} \;=\; \frac{\pi}{2} - \int_1^\infty \mathrm{d}y \frac{\mathrm{e}^{-|E|y}}{y\sqrt{y^2-1}}\,. \tag{2.21}$$

2.2.3 Residues of Response Function of Circular Motion in 3+1 Dimensions

The response function in 3+1 dimensions is given by (see equation (2.61))

$$\mathcal{F}(E) \;=\; -\frac{E}{2\pi}\Theta(-E) - \frac{1}{8\pi^2\gamma v R}\oint_{\mathcal{C}} \mathrm{d}z\, \frac{\exp\left\{\mathrm{i}\frac{2ER}{\gamma v}z\right\}}{\frac{z^2}{v^2}-\sin^2 z}\,. \tag{2.22}$$

Calculating the residues at $z = z_n$ shows that

$$\mathcal{F}_n(E) \;=\; -\frac{v}{8\pi\gamma R}\sum_n \frac{\exp\left\{-\frac{2|E|R}{\gamma v}(\alpha_n+\mathrm{i}\beta_n)\right\}}{(\alpha_n+\mathrm{i}\beta_n)\,(1+\mathrm{i}\alpha_n\tan\beta_n+\beta_n\cot\beta_n)}\,, \tag{2.23}$$

where the denominator needs some rearranging, trigonometric identities and the equations (2.49a) and (2.49b). The residue at $z_0 = \mathrm{i}\alpha_0$ with $\beta_0 = 0$ is of further relevance, and can be calculated using the most general solution above

$$\mathcal{F}_0(E) \;=\; \frac{v}{8\pi\gamma R}\frac{\mathrm{e}^{-E\frac{2R}{\gamma v}\alpha_0}}{(\alpha_0 - v^2\sinh\alpha_0\cosh\alpha_0)}\,. \tag{2.24}$$

B.3 Bogoliubov Transformation

The Bogoliubov transformation in (4.75) is given by the differential equation

$$\frac{\mathrm{d}}{\mathrm{d}\mu}\begin{pmatrix}\widetilde{X}_i\\ \widetilde{X}_k^\dagger\end{pmatrix} \;=\; \mathcal{M}\begin{pmatrix}\hat{X}_i\\ \hat{X}_l^\dagger\end{pmatrix}\,, \tag{2.25}$$

with

$$\mathcal{M} \;=\; \begin{pmatrix}\delta\alpha' & \delta\beta'\\ (\delta\beta')^* & (\delta\alpha')^*\end{pmatrix}\,. \tag{2.26}$$

The prime indicates a differentiation with respect to μ. We find

$$\delta\alpha \;=\; \begin{pmatrix}0 & 0 & \mathrm{i}\\ 0 & 0 & 0\\ \mathrm{i} & 0 & 0\end{pmatrix} \tag{2.27}$$

and

$$\delta\beta \;=\; \begin{pmatrix}0 & 0 & 0\\ 0 & 0 & \mathrm{i}\\ 0 & \mathrm{i} & 0\end{pmatrix}\,. \tag{2.28}$$

With those results we find

$$\mathcal{M} = \mathrm{i}\begin{pmatrix} 0 & 0 & 1 & 0 & 0 & 0 \\ 0 & 0 & 0 & 0 & 0 & 1 \\ 1 & 0 & 0 & 0 & 1 & 0 \\ 0 & 0 & 0 & 0 & 0 & -1 \\ 0 & 0 & -1 & 0 & 0 & 0 \\ 0 & -1 & 0 & -1 & 0 & 0 \end{pmatrix} \quad , \quad \mathcal{M}^2 = \begin{pmatrix} -1 & 0 & 0 & 0 & -1 & 0 \\ 0 & 1 & 0 & 1 & 0 & 0 \\ 0 & 0 & 0 & 0 & 0 & 0 \\ 0 & -1 & 0 & -1 & 0 & 0 \\ 1 & 0 & 0 & 1 & 0 & 0 \\ 0 & 0 & 0 & 0 & 0 & 0 \end{pmatrix} \tag{2.29}$$

and every higher order vanishing.

References

[1] C. Kiefer, *Why quantum gravity?*, Quantum Gravity, Oxford University Press, 04 2012.

[2] S. Carlip, *Is quantum gravity necessary?*, Classical and Quantum Gravity **25** (2008), no. 15, 154010.

[3] S. Hollands and R. M. Wald, *Quantum fields in curved spacetime*, Physics Reports **574** (2015), 1–35, Quantum fields in curved spacetime.

[4] N. Birrell and P. Davies, *Quantum fields in curved space*, Cambridge University Press, 1982.

[5] P. W. Higgs, *Broken symmetries and the masses of gauge bosons*, Phys. Rev. Lett. **13** (1964), 508–509.

[6] G. e. Aad, *Observation of a new particle in the search for the Standard Model Higgs boson with the ATLAS detector at the LHC*, Physics Letters B **716** (2012), no. 1, 1–29.

[7] LIGO Scientific Collaboration and Virgo Collaboration, *Observation of gravitational waves from a binary black hole merger*, Phys. Rev. Lett. **116** (2016), 061102.

[8] The Event Horizon Telescope Collaboration, *First M87 Event Horizon Telescope Results. i. the shadow of the supermassive black hole*, The Astrophysical Journal Letters **875** (2019), no. 1, L1.

[9] A. Einstein, *Erklärung der Perihelbewegung des Merkur aus der allgemeinen Relativitätstheorie*, Sitzungsberichte der Königlich Preussischen Akademie der Wissenschaften (1915), 831–839.

[10] K. Schwarzschild, *Über das Gravitationsfeld eines Massenpunktes nach der Einsteinschen Theorie*, Sitzungsberichte der Königlich Preussischen Akademie der Wissenschaften (1916), 189–196.

[11] S. Hawking, *Black hole explosions?*, Nature **248** (1974), 30–31.

[12] L. Parker, *Particle creation in expanding universes*, Phys. Rev. Lett. **21** (1968), 562–564.

[13] L. Parker, *Quantized fields and particle creation in expanding universes. I*, Phys. Rev. **183** (1969), 1057–1068.

[14] L. Parker, *Quantized fields and particle creation in expanding universes. II*, Phys. Rev. D **3** (1971), 346–356.

[15] L. Parker and J. Navarro-Salas, *Fifty years of cosmological particle creation*, 2017.

[16] S. A. Fulling, *Nonuniqueness of canonical field quantization in Riemannian space-time*, Phys. Rev. D **7** (1973), 2850–2862.

[17] W. G. Unruh, *Notes on black-hole evaporation*, Phys. Rev. D **14** (1976), 870–892.

[18] W. G. Unruh and R. M. Wald, *What happens when an accelerating observer detects a Rindler particle*, Phys. Rev. D **29** (1984), 1047–1056.

[19] J. S. Ben-Benjamin, M. O. Scully, S. A. Fulling, D. M. Lee, D. N. Page, A. A. Svidzinsky, M. S. Zubairy, M. J. Duff, R. Glauber, W. P. Schleich, and W. G. Unruh, *Unruh acceleration radiation revisited*, International Journal of Modern Physics A **34** (2019), no. 28, 1941005, https://doi.org/10.1142/S0217751X19410057.

[20] P. C. W. Davies, *Scalar particle production in Schwarzschild and Rindler metrics*, J. Phys. A **8** (1975), 609–616.

[21] J. Bell and J. Leinaas, *Electrons as accelerated thermometers*, Nucl. Phys. B **212** (1983), no. 1, 131–150.

[22] J. Bell and J. Leinaas, *The Unruh effect and quantum fluctuations of electrons in storage rings*, Nucl. Phys. B **284** (1987), 488–508.

[23] W. G. Unruh, Map and Territory in Physics: The Role of an Analogy in Black Hole Physics, 233–243, Springer International Publishing, Cham, 2018, p. 233–243.

[24] W. G. Unruh, *Experimental black-hole evaporation?*, Phys. Rev. Lett. **46** (1981), 1351–1353.

[25] W. G. Unruh, *Sonic analogue of black holes and the effects of high frequencies on black hole evaporation*, Phys. Rev. D **51** (1995), 2827–2838.

[26] W. Unruh, *Has Hawking radiation been measured?*, Foundations of Physics **44** (2014), 532–545.

[27] M. Visser, *Acoustic propagation in fluids: an unexpected example of Lorentzian geometry*, 1993.

[28] M. Visser, *Acoustic black holes: horizons, ergospheres and hawking radiation*, Classical and Quantum Gravity **15** (1998), no. 6, 1767.

[29] M. Visser, *Acoustic black holes*, 1999.

[30] C. Barceló, S. Liberati, and M. Visser, *Analogue gravity*, Living Rev. Relativ. **14** (2011), 3.

[31] M. J. Jacquet, S. Weinfurtner, and F. König, *The next generation of analogue gravity experiments*, Philosophical Transactions of the Royal Society A: Mathematical, Physical and Engineering Sciences **378** (2020), no. 2177, 20190239, https://royalsocietypublishing.org/doi/pdf/10.1098/rsta.2019.0239.

[32] W. G. Unruh, Irrotational, Two-Dimensional Surface Waves in Fluids, 63–80, Springer International Publishing, Cham, 2013, p. 63–80.

[33] T. G. Philbin, C. Kuklewicz, S. Robertson, S. Hill, F. König, and U. Leonhard, *Fiber-optical analog of the event horizon*, Science **319** (2008), 1367–1370.

[34] F. Belgiorno, S. L. Cacciatori, G. Ortenzi, L. Rizzi, V. Gorini, and D. Faccio, *Dielectric black holes induced by a refractive index perturbation and the Hawking effect*, Phys. Rev. D **83** (2011), 024015.

[35] R. Schützhold and W. G. Unruh, *Gravity wave analogues of black holes*, Phys. Rev. D **66** (2002), 044019.

[36] C. Barceló, S. Liberati, and M. Visser, *Analogue gravity from Bose-Einstein condensates*, Classical and Quantum Gravity **18** (2001), no. 6, 1137.

[37] C. Barceló, S. Liberati, and M. Visser, *Analogue models for FRW cosmologies*, International Journal of Modern Physics D **12** (2003), no. 09, 1641–1649, https://doi.org/10.1142/S0218271803004092.

[38] L. J. Garay, J. R. Anglin, J. I. Cirac, and P. Zoller, *Sonic analog of gravitational black holes in Bose-Einstein condensates*, Phys. Rev. Lett. **85** (2000), 4643–4647.

[39] L. J. Garay, J. R. Anglin, J. I. Cirac, and P. Zoller, *Sonic black holes in dilute Bose-Einstein condensates*, Phys. Rev. A **63** (2001), 023611.

[40] G. Volovik, *Black-hole horizon and metric singularity at the brane separating two sliding superfluids*, Jetp Lett. **76** (2002), 240–244.

[41] G. Volovik, Effective gravity and quantum vacuum in superfluids, 127–177, p. 127–177.

[42] S. Weinfurtner, E. W. Tedford, M. C. J. Penrice, W. G. Unruh, and G. A. Lawrence, *Measurement of stimulated Hawking emission in an analogue system*, Phys. Rev. Lett. **106** (2011), 021302.

[43] T. Torres, S. Patrick, A. Coutant, M. Richartz, E. W. Tedford, and S. Weinfurtner, *Rotational superradiant scattering in a vortex flow*, Nat. Phys. **13** (2017), no. 9, 833.

[44] S. Patrick, A. Coutant, M. Richartz, and S. Weinfurtner, *Black hole quasibound states from a draining bathtub vortex flow*, Phys. Rev. Lett. **121** (2018), 061101.

[45] S. Patrick, H. Goodhew, C. Gooding, and S. Weinfurtner, *Backreaction in an analogue black hole experiment*, Phys. Rev. Lett. **126** (2021), 041105.

[46] A. Retzker, J. I. Cirac, M. B. Plenio, and B. Reznik, *Methods for detecting acceleration radiation in a Bose-Einstein condensate*, Phys. Rev. Lett. **101** (2008), 110402.

[47] U. Leonhardt, I. Griniasty, S. Wildeman, E. Fort, and M. Fink, *Classical analog of the Unruh effect*, Phys. Rev. A **98** (2018), 022118.

[48] P. O. Fedichev and U. R. Fischer, *"Cosmological" quasiparticle production in harmonically trapped superfluid gases*, Phys. Rev. A **69** (2004), 033602.

[49] C. Barceló, S. Liberati, and M. Visser, *Towards the observation of Hawking radiation in Bose-Einstein condensates*, International Journal of Modern Physics A **18** (2003), no. 21, 3735–3745, https://doi.org/10.1142/S0217751X0301615X.

[50] S. Weinfurtner, P. Jain, M. Visser, and C. W. Gardiner, *Cosmological particle production in emergent rainbow spacetimes*, Classical and Quantum Gravity **26** (2009), no. 6, 065012.

[51] P. Jain, S. Weinfurtner, M. Visser, and C. W. Gardiner, *Analog model of a Friedmann-Robertson-Walker universe in Bose-Einstein condensates: Application of the classical field method*, Phys. Rev. A **76** (2007), 033616.

[52] S. Chä and U. R. Fischer, *Probing the scale invariance of the inflationary power spectrum in expanding quasi-two-dimensional dipolar condensates*, Phys. Rev. Lett. **118** (2017), 130404.

[53] U. R. Fischer and R. Schützhold, *Quantum simulation of cosmic inflation in two-component Bose-Einstein condensates*, Phys. Rev. A **70** (2004), 063615.

[54] S. Biermann, S. Erne, C. Gooding, J. Louko, J. Schmiedmayer, W. G. Unruh, and S. Weinfurtner, *Unruh and analogue Unruh temperatures for circular motion in 3+1 and 2+1 dimensions*, Phys. Rev. D **102** (2020), no. 8, 085006.

[55] C. Gooding, S. Biermann, S. Erne, J. Louko, W. G. Unruh, J. Schmiedmayer, and S. Weinfurtner, *Interferometric Unruh detectors for Bose-Einstein condensates*, Phys. Rev. Lett. **125** (2020), no. 21, 213603.

[56] C. R. D. Bunney, S. Biermann, V. S. Barroso, A. Geelmuyden, S. Gooding, G. Itier, X. Rojas, J. Louko, and S. Weinfurtner, *Third sound detectors in accelerated motion*, 2023.

[57] K. Aoki and T. Mitsui, *Thermal interface fluctuations of liquids and viscoelastic materials*, Progress of Theoretical and Experimental Physics **2018** (2018), no. 4, https://academic.oup.com/ptep/article-pdf/2018/4/043J01/24589360/pty026.pdf, 043J01.

[58] T. Mitsui and K. Aoki, *Michelson interferometry with quantum noise reduction*, arXiv:1206.3828 [physics.optics].

[59] W. Rindler, *Kruskal space and the uniformly accelerated frame*, American Journal of Physics **34** (1966), no. 12, 1174–1178.

[60] M. E. Peskin and D. V. Schroeder, *An Introduction to quantum field theory*, Addison-Wesley, Reading, USA, 1995.

[61] S. Takagi, *Vacuum Noise and Stress Induced by Uniform Acceleration: Hawking-Unruh Effect in Rindler Manifold of Arbitrary Dimension*, Prog. Theor. Phys. Suppl. **88** (1986), 1–142.

[62] S. Fulling, *Aspects of quantum field theory in curved spacetime*, EBL-Schweitzer, Cambridge University Press, 1989.

[63] S. W. Hawking and W. Israel, *General Relativity: An Einstein Centenary Survey*, Univ. Pr., Cambridge, UK, 1979.

[64] J. Louko and A. Satz, *Transition rate of the Unruh–DeWitt detector in curved spacetime*, Classical and Quantum Gravity **25** (2008), no. 5, 055012.

[65] A. Einstein, *Zur Quantentheorie der Strahlung*, Phys. Z. **18** (1917), 121–128.

[66] L. Hodgkinson, *Particle detectors in curved spacetime quantum field theory*, 2013.

[67] W. G. Unruh, *Acceleration radiation for orbiting electrons*, Phys. Rept. **307** (1998), 163–171, `hep-th/9804158`.

[68] S. Schlicht, *Considerations on the Unruh effect: causality and regularization*, Classical and Quantum Gravity **21** (2004), no. 19, 4647–4660.

[69] J. Louko and A. Satz, *How often does the Unruh–DeWitt detector click? regularization by a spatial profile*, Classical and Quantum Gravity **23** (2006), no. 22, 6321–6343.

[70] A. Satz, *Then again, how often does the Unruh–DeWitt detector click if we switch it carefully?*, Classical and Quantum Gravity **24** (2007), no. 7, 1719–1731.

[71] J. Audretsch, R. Müller, and M. Holzmann, *Generalized Unruh effect and Lamb shift for atoms on arbitrary stationary trajectories*, Classical and Quantum Gravity **12** (1995), no. 12, 2927.

[72] L. Hodgkinson and J. Louko, *How often does the Unruh-DeWitt detector click beyond four dimensions?*, Journal of Mathematical Physics **53** (2012), no. 8, 082301, `https://doi.org/10.1063/1.4739453`.

[73] G. E. Volovik, *The universe in a helium droplet*, vol. 117, Oxford University Press on Demand, 2003.

[74] O. Levin, Y. Peleg, and A. Peres, *Unruh effect for circular motion in a cavity*, Journal of Physics A: Mathematical and General **26** (1993), no. 12, 3001–3011.

[75] P. C. W. Davies, T. Dray, and C. A. Manogue, *Detecting the rotating quantum vacuum*, Phys. Rev. D **53** (1996), 4382–4387.

[76] S. Gutti, S. Kulkarni, and L. Sriramkumar, *Modified dispersion relations and the response of the rotating Unruh-DeWitt detector*, Phys. Rev. D **83** (2011), 064011.

[77] C. R. D. Bunney and J. Louko, *Circular motion analogue unruh effect in a* $2+1$ *thermal bath: Robbing from the rich and giving to the poor*, 2023.

[78] L. Hodgkinson, J. Louko, and A. C. Ottewill, *Static detectors and circular-geodesic detectors on the Schwarzschild black hole*, Phys. Rev. D **89** (2014), 104002.

[79] S.-Y. Lin and B. L. Hu, *Backreaction and the Unruh effect: New insights from exact solutions of uniformly accelerated detectors*, Physical Review D **76** (2007), no. 6.

[80] D. Moustos and C. Anastopoulos, *Non-Markovian time evolution of an accelerated qubit*, Physical Review D **95** (2017), no. 2.

[81] B. Sokolov, J. Louko, S. Maniscalco, and I. Vilja, *Unruh effect and information flow*, Physical Review D **101** (2020), no. 2.

[82] C. J. Fewster, B. A. Juárez-Aubry, and J. Louko, *Waiting for Unruh*, Classical and Quantum Gravity **33** (2016), no. 16, 165003.

[83] W. G. Unruh and R. Schützhold, The Analogue Between Rimfall and Black Holes, 1–4, Springer Berlin Heidelberg, Berlin, Heidelberg, 2007, p. 1–4.

[84] W. G. Unruh and R. Schützhold, *On slow light as a black hole analogue*, Phys. Rev. D **68** (2003), 024008.

[85] W. G. Unruh and R. Schützhold, *Universality of the Hawking effect*, Phys. Rev. D **71** (2005), 024028.

[86] S. Weinfurtner, E. Tedford, M. Penrice, W. Unruh, and G. Lawrence, *Measurement of stimulated Hawking emission in an analogue system*, Phys. Rev. Lett. **106** (2011), 021302.

[87] L.-P. Euvé, F. Michel, R. Parentani, T. Philbin, and G. Rousseaux, *Observation of noise correlated by the Hawking effect in a water tank*, Phys. Rev. Lett. **117** (2016), 121301.

[88] T. G. Philbin, C. Kuklewicz, S. Robertson, S. Hill, F. König, and U. Leonhardt, *Fiber-optical analog of the event horizon*, Science **319** (2008), no. 5868, 1367–1370.

[89] F. Belgiorno, S. L. Cacciatori, M. Clerici, V. Gorini, G. Ortenzi, L. Rizzi, E. Rubino, V. G. Sala, and D. Faccio, *Hawking radiation from ultrashort laser pulse filaments*, Phys. Rev. Lett. **105** (2010), 203901.

[90] J. Muñoz de Nova, K. Golubkov, V. Kolobov, and J. Steinhauer, *Observation of thermal Hawking radiation and its temperature in an analogue black hole*, Nature **569** (2019), 688–691.

[91] J. D. Jackson, *Classical electrodynamics*, American Cancer Society, 2003.

[92] R. Grimm, M. Weidemüller, and Y. B. Ovchinnikov, *Optical dipole traps for neutral atoms.*

[93] W. Ketterle, D. S. Durfee, and D. M. Stamper-Kurn, *Making, probing and understanding Bose-Einstein condensates*, 1999.

[94] L. Allen and J. Eberly, *Optical resonance and two-level atoms*, New York ; London : Wiley, 1975.

[95] J. A. Stratton, *Electromagnetic theory*, John Wiley & Sons, Ltd, 2015.

[96] D. E. Aspnes, *Local-field effects and effective-medium theory: A microscopic perspective*, American Journal of Physics **50** (1982), no. 8, 704–709.

[97] A. Einstein, *Quantentheorie des einatomigen idealen Gases*, John Wiley and Sons, Ltd, 2005.

[98] A. Leanhardt, T. Pasquini, M. Saba, A. SchirotzeK, Y. Shin, D. Kielpinski, D. Pritchard, and W. Ketterle, *Cooling Bose-Einstein condensates below 500 picokelvin*, Science **301** (2003), no. 5639, 1513–1515.

[99] N. N. Bogolyubov, *On the theory of superfluidity*, J. Phys. (USSR) **11** (1947), 23–32.

[100] L. P. Pitaevskj and S. Stringari, *Bose-Einstein condensation and superfluidity*, 2016.

[101] L. Salasnich, A. Parola, and L. Reatto, *Effective wave equations for the dynamics of cigar-shaped and disk-shaped Bose condensates*, Phys. Rev. A **65** (2002), 043614.

[102] R. Meppelink, S. B. Koller, and P. van der Straten, *Sound propagation in a Bose-Einstein condensate at finite temperatures*, Phys. Rev. A **80** (2009), 043605.

[103] P. Kapitza, *Viscosity of liquid Helium below the lambda-point*, Nature **142** (1938), 74.

[104] L. Landau, *Theory of the superfluidity of Helium II*, Phys. Rev. **60** (1941), 356–358.

[105] R. J. Donnelly and C. F. Barenghi, *The observed properties of liquid Helium at the saturated vapor pressure*, Journal of Physical and Chemical Reference Data **27** (1998), no. 6, 1217–1274.

[106] A. J. Leggett, *Interpretation of recent results on He^3 below 3 mK: A new liquid phase?*, Phys. Rev. Lett. **29** (1972), 1227–1230.

[107] I. Khalatnikov, *An introduction to the theory of superfluidity*, CRC Press, 1965.

[108] D. L. Goodstein and P. G. Saffman, *The two fluid model of the Helium film*, Proceedings of the Royal Society of London. Series A, Mathematical and Physical Sciences **325** (1971), no. 1563, 447–468.

[109] K. R. Atkins, *Third and fourth sound in liquid Helium ii*, Phys. Rev. **113** (1959), 962–965.

[110] K. R. Atkins and I. Rudnick, *Chapter 2 third sound*, Progress in low temperature physics **6** (1970), 37–76.

[111] P. Brouwer, W. Draisma, H. van Beelen, and R. Jochemsen, *On the propagation of third sound in 4He films*, Physica B: Condensed Matter **215** (1995), no. 2, 135–152.

[112] P. Roche, G. Deville, K. O. Keshishev, N. J. Appleyard, and F. I. B. Williams, *Low damping of micron capillary waves on superfluid ^4He*, Phys. Rev. Lett. **75** (1995), 3316–3319.

[113] D. Tilley and J. Tilley, *Superfluidity and superconductivity*, Routledge, 1990.

[114] J. C. Luke, *A variational principle for a fluid with a free surface*, Journal of Fluid Mechanics **27** (1967), no. 2, 395.

[115] R. J. Glauber, *Coherent and incoherent states of the radiation field*, Phys. Rev. **131** (1963), 2766.

[116] H. J. Carmichael, *Spectrum of squeezing and photocurrent shot noise: a normally ordered treatment*, J. Opt. Soc. Am. B **4** (1987), no. 10, 1588.

[117] P. L. Kelley and W. H. Kleiner, *Theory of electromagnetic field measurement and photoelectron counting*, Phys. Rev. **136** (1964), A316–A334.

[118] R. J. Glauber, *The quantum theory of optical coherence*, Phys. Rev. **130** (1963), 2529–2539.

[119] W. Bowen and G. Milburn, *Quantum optomechanics*, Taylor & Francis, 2015.

[120] G. J. M. D.F. Walls, *Quantum optics*, Springer, Berlin, Heidelberg, 2008.

[121] V. Sudhir, *Quantum limits on measurement and control of a mechanical oscillator*, Springer International Publishing AG, 2017.

[122] W. Unruh, *Black holes, acceleration temperature and low temperature analog experiments*, J Low Temp Phys **208** (2022), 196–209.

[123] L. Landau and E. Lifshitz, *Fluid mechanics*, Oxford: Pergamon Press, 1959.

[124] A. Tay, C. Thibierge, D. Fournier, C. Fretigny, F. Lequeux, C. Monteux, J. P. Roger, and L. Talini, *Probing thermal waves on the free surface of various media: Surface fluctuation specular reflection spectroscopy*, Review of Scientific Instruments **79** (2008), no. 10, 103107.

[125] R. Loudon, *Theory of thermally induced surface fluctuations on simple fluids*, Proceedings of the Royal Society of London. Series A, Mathematical and Physical Sciences **372** (1980), no. 1749, 275–295.

[126] D. Langevin and J. Meunier, *Light scattering and reflectivity of liquid interfaces*, Journal de Physique Colloques **44** (1983), no. C10, C10–155–C10–161.

[127] M. Bouchiat and J. Meunier, *Spectre des fluctuations thermiques de la surface libre d'un liquide simple*, Journal de Physique **32** (1971), no. 7, 561–571.

[128] R. Wong, *Asymptotic approximations of integrals*, Academic Press, 1989.